

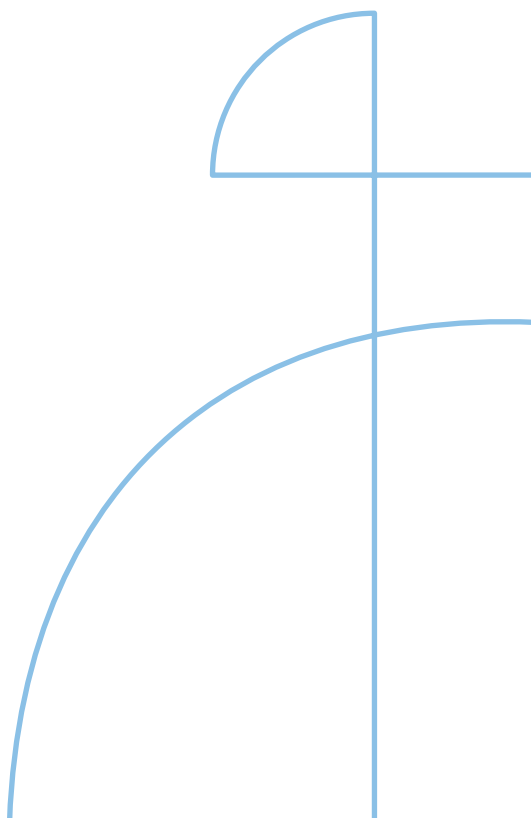


Doctoral Thesis in Chemical Engineering

# Carbonate-based solvents for carbon capture

NIMA MIRZAEI

KTH ROYAL INSTITUTE OF TECHNOLOGY



# Carbonate-based solvents for carbon capture

NIMA MIRZAEI

Academic Dissertation which, with due permission of the KTH Royal Institute of Technology, is submitted for public defence for the Degree of Doctor of Philosophy on Thursday the 23rd of April 2026, at 10:00 a.m. in F3, Lindstedtsvägen 26, Stockholm.

Doctoral Thesis in Chemical Engineering  
KTH Royal Institute of Technology  
Stockholm, Sweden 2026

© Nima Mirzaei

ISBN 978-91-8106-574-9  
TRITA-CBH-FOU-2026:19

Printed by: Universitetservice US-AB, Sweden 2026

*I'm in the light and flood  
I'm in the four winds  
I'm the waves, shaping pebbles, flawless gems  
I am the snow on your palm*

*I am the secret stream  
Moss beneath your feet  
I am you who climbed off my back not long ago  
A sheltered song in a world now gone, petrichor  
The timeless*

Lanternlight, Nightwish

*Blackened is the end, winter it will send  
Throwing all you see into obscurity  
Death of Mother Earth, never a rebirth  
Evolutions's end, never will it mend  
Never*

*Fire to begin whipping dance of the dead  
Blackened is the end  
To begin whipping dance of the dead  
Color our world blackened*

Blackened, Metallica



# Carbonate-based solvents for carbon capture

Nima Mirzaei

Department of Chemical Engineering, KTH Royal Institute of Technology  
SE-100 44 Stockholm, Sweden

## Abstract

Carbon dioxide ( $\text{CO}_2$ ) emissions from the combustion of fossil fuels and biomass used for energy production drive global warming and climate change. Carbon capture and storage (CCS), involving the removal of  $\text{CO}_2$  from combustion flue gas and its sequestration in geological formations, is therefore a key strategy for reducing the  $\text{CO}_2$  emissions. Absorption processes based on aqueous potassium carbonate ( $\text{K}_2\text{CO}_3$ ) are among the first-generation carbon capture technologies due to process maturity, benign chemistry, and operational robustness. Owing to its high potential for waste heat recovery, aqueous  $\text{K}_2\text{CO}_3$  is considered particularly suitable for applications where low-grade heat is a valuable product. The main limitation of aqueous  $\text{K}_2\text{CO}_3$ , however, is the slow absorption rate of  $\text{CO}_2$ , which results in a large material footprint and an electricity demand for flue gas compression. To alleviate this limitation, rate promoters are added to enhance the  $\text{CO}_2$  absorption rate.

This thesis investigates boric acid ( $\text{B}(\text{OH})_3$ ) and vanadium pentoxide ( $\text{V}_2\text{O}_5$ ), which are employed as rate promoters in industrial solvent blends. Absorption experiments were conducted using a stirred batch reactor over a broad range of promoter concentrations and solvent loadings. Boric acid exhibited negligible rate enhancement but was found to increase the absorption capacity for  $\text{CO}_2$  through an additional buffering effect. In contrast, vanadium pentoxide increased the  $\text{CO}_2$  absorption rate by up to 2–3 times that of unpromoted  $\text{K}_2\text{CO}_3$ , a performance comparable to that of monoethanolamine (MEA) as promoter. This rate enhancement occurs because the active species, hydrogen monovanadate, catalyzes the hydrolysis of  $\text{CO}_2$ . These results provide a mechanistic understanding of the roles of  $\text{B}(\text{OH})_3$  and  $\text{V}_2\text{O}_5$  in improving  $\text{CO}_2$  absorption in aqueous  $\text{K}_2\text{CO}_3$ . The kinetic rate models developed to describe the experimental observations can serve as a sound basis for accurate design of large-scale absorption processes.

**Keywords:** Carbon capture, Absorption, Aqueous potassium carbonate, Rate promoters, Vanadium pentoxide, Boric acid



# Karbonatbaserade lösningar för koldioxidinfångning

Nima Mirzaei

Institutionen för Kemiteknik, Kungliga Tekniska högskolan,  
SE-100 44 Stockholm, Sverige

## Sammanfattning

Antropogena utsläpp av koldioxid ( $\text{CO}_2$ ) till atmosfären från förbränning av fossila bränslen och biomassa leder till global uppvärmning och klimatförändringar. För att begränsa  $\text{CO}_2$ -utsläppen används *carbon capture and storage* (CCS). CCS innebär infångning av  $\text{CO}_2$  från förbränningsrökgaser samt lagring av denna  $\text{CO}_2$  i geologiska formationer. Absorptionsprocesser baserade på kaliumkarbonat ( $\text{K}_2\text{CO}_3$ ) tillhör den första generationens tekniker för  $\text{CO}_2$ -avskiljning, tack vare deras etablerade teknik, giftfria kemi och driftsäkerhet. Dessutom är den höga potentialen för spillvärmeåtervinning i  $\text{K}_2\text{CO}_3$ -baserade processer särskilt fördelaktig i tillämpningar där lågtemperaturvärme är en värdefull produkt. En begränsning med  $\text{K}_2\text{CO}_3$ -lösningen är den långsamma absorptionshastigheten för  $\text{CO}_2$ , vilket medför stort materialbehov och ett ökat elbehov för kompression av rökgaser. Därför tillsätts promotorer till  $\text{K}_2\text{CO}_3$ -lösningen för att öka absorptionshastigheten för  $\text{CO}_2$ .

Denna avhandling karaktäriserar borsyra och vanadinpentoxid, vilka används som promotorer i industriella  $\text{K}_2\text{CO}_3$ -blandningar. Absorptionsexperiment genomfördes i en satsreaktor med omrörning med varierande promotor- och  $\text{CO}_2$ -koncentrationer. Borsyra visade endast en försumbar påverkan på reaktionshastigheten, men en ökad absorptionskapacitet för  $\text{CO}_2$  genom en buffrande effekt. Vanadinpentoxid ökade absorptionshastigheten för  $\text{CO}_2$  upp till 2–3 gånger jämfört med icke-promoterat  $\text{K}_2\text{CO}_3$ , vilket är jämförbart med monoetanolamin (MEA) som promotor. Denna ökning beror på att den aktiva formen av vanadin katalyserar hydrolysen av  $\text{CO}_2$ . Dessa resultat ger en mekanistisk förståelse av hur borsyra och vanadinpentoxid förbättrar  $\text{CO}_2$ -absorption i  $\text{K}_2\text{CO}_3$ -solventer. De kinetiska modeller som utvecklats för att beskriva de experimentella observationerna möjliggör noggrann dimensionering av storskaliga absorptionsprocesser.

**Nyckelord:** Koldioxidinfångning, Absorption, Kaliumkarbonatlösning, Promotorer, Vanadinpentoxid, Borsyra



## Preface

This thesis presents rate data on CO<sub>2</sub> absorption in promoted blends of aqueous K<sub>2</sub>CO<sub>3</sub> for carbon capture processes. This summary consists of introduction, aim statement, literature overview, experiments and methodology, and a presentation of the results. Appended to this thesis are four articles listed below, which are summarized in the first part.

### List of publications

**Paper I.** NIMA MIRZAEI, AISHWARYA BABU, EFTHYMOS KANTARELIS, AND MATTHÄUS U. BÄBLER, 2023. Screening study of potassium carbonate solvents for bio-energy carbon capture and storage (BECCS). *Chemical Engineering Transactions* **105**, 157–162.

**Paper II.** NIMA MIRZAEI, FLORIAN WALTHERT, EFTHYMOS KANTARELIS, AND MATTHÄUS U. BÄBLER, 2025. Experiments and kinetic modeling of absorption rates of CO<sub>2</sub> into unpromoted K<sub>2</sub>CO<sub>3</sub> solutions at low to high solvent loading. *Separation and Purification Technology* **378** (3), 134622.

**Paper III.** NIMA MIRZAEI AND MATTHÄUS U. BÄBLER, 2025. Kinetic and mechanistic study of CO<sub>2</sub> absorption into vanadium-promoted aqueous K<sub>2</sub>CO<sub>3</sub>. *ACS Sustainable Chemistry & Engineering* **13** (42), 18163–18175.

**Paper IV.** NIMA MIRZAEI AND MATTHÄUS U. BÄBLER. Absorption of CO<sub>2</sub> into aqueous K<sub>2</sub>CO<sub>3</sub> co-buffered with borates. Manuscript under preparation.

### Author contributions

**Paper I.** N. Mirzaei: *conceptualization, methodology, data analysis, original draft, review and editing.* A. Babu: *methodology.* E. Kantarelis: *methodology, supervision, review.* M. U. Babler: *conceptualization, data analysis, review and editing, supervision, funding acquisition.*

**Paper II.** N. Mirzaei: *conceptualization, methodology, data analysis, original draft, review and editing.* F. Walthert: *methodology, review and editing.* E. Kantarelis: *methodology, supervision, review.* M. U. Babler: *conceptualization, data analysis, review and editing, supervision, funding acquisition.*

**Paper III.** N. Mirzaei: *conceptualization, methodology, data analysis, original draft, review and editing.* M. U. Babler: *conceptualization, data analysis, review and editing, supervision, funding acquisition.*

**Paper IV.** N. Mirzaei: *conceptualization, methodology, data analysis, original draft.* M. U. Babler: *conceptualization, review and editing, supervision, funding acquisition.*

## Conference presentations

N. MIRZAEI, M. TAGLIAVINI, M. U. BABLER. Characterization of CO<sub>2</sub> loading of potassium carbonate absorption solvents. 2<sup>nd</sup> International Conference on Negative CO<sub>2</sub> Emissions. Gothenburg, Sweden, 2022.

N. MIRZAEI, F. WALTHERT, E. KANTARELIS, M. U. BABLER. Enhanced bio-energy carbon capture and storage (BECCS) using V<sub>2</sub>O<sub>5</sub> promoted aqueous K<sub>2</sub>CO<sub>3</sub>. 14<sup>th</sup> European Congress of Chemical Engineering (ECCE14). Berlin, Germany, 2023.

N. MIRZAEI, A. BABU, E. KANTARELIS, M. U. BABLER. Screening study of potassium carbonate solvents for bio-energy carbon capture and storage (BECCS). 2<sup>nd</sup> International Conference on Energy, Environment & Digital Transition (E2DT). Palermo, Italy, 2023.

N. MIRZAEI, M. U. BABLER. Absorption of CO<sub>2</sub> by aqueous K<sub>2</sub>CO<sub>3</sub> promoted with V<sub>2</sub>O<sub>5</sub>. 13<sup>th</sup> Trondheim CCS Conference (TCCS13). Trondheim, Norway, 2025.

April 2026, Stockholm

*Nima Mirzaei*

# Contents

<b>Abstract</b>	iii
<b>Sammanfattning</b>	v
<b>Preface</b>	vii
<b>Abbreviations</b>	xi
<b>Notations</b>	xii
<b>Chapter 1. Introduction</b>	1
1.1. Global warming and climate change	1
1.2. Becoming net zero	2
1.3. Swedish context	4
1.4. Aim statement	4
<b>Chapter 2. Background</b>	6
2.1. Carbon dioxide supply chain	6
2.1.1. Carbon capture	6
2.1.2. Conditioning and transport	7
2.1.3. Geological storage	8
2.1.4. Utilization	9
2.2. Carbon capture by absorption	10
2.2.1. Amine-based solvents	11
2.2.2. Ammonia	13
2.2.3. Amino acids	14
2.2.4. Carbonates	15
2.3. Chemistry of aqueous $K_2CO_3$	16
2.4. Rate promoters for aqueous $K_2CO_3$	18
2.4.1. Amines and amino acids	20
2.4.2. Enzymes	21
2.4.3. Vanadium pentoxide	22
2.4.4. Boric acid	22
<b>Chapter 3. Methods</b>	24

3.1. Gas-liquid contactor configurations	24
3.2. Experimental setup	27
3.3. Data processing	28
<b>Chapter 4. Results and discussion</b>	<b>31</b>
4.1. Raw pressure-time data	31
4.2. Setup characterization	32
4.2.1. Mass balance over setup	32
4.2.2. Vapor-liquid equilibrium	33
4.2.3. Liquid-side mass transfer coefficient	33
4.3. Absorption into unpromoted $K_2CO_3$	35
4.4. Rate promoter screening	41
4.5. Absorption in $V_2O_5$ -promoted solvent	42
4.6. Absorption in presence of $B(OH)_3$	47
<b>Chapter 5. Conclusions</b>	<b>53</b>
5.1. Summary and conclusions	53
5.2. Sustainability contribution	55
5.3. Future work	55
<b>Appendix A. Mass transfer across gas-liquid interface</b>	<b>58</b>
A.1. Two-film model	58
A.2. Film theory	59
A.2.1. Physical absorption	61
A.2.2. Pseudo-first order reaction regime	61
A.2.3. Instantaneous regime	62
<b>Appendix B. Sample preparation and characterization</b>	<b>64</b>
B.1. Blending of solvents	64
B.2. Acid-base titration	65
<b>Acknowledgements</b>	<b>68</b>
<b>Bibliography</b>	<b>70</b>

# Abbreviations

AMP	Aminomethyl propanol
CA	Carbonic anhydrase
CAP	Chilled ammonia process
CCS	Carbon capture and storage
CHP	Combined heat and power
DACCS	Direct air carbon capture and storage
DEA	Diethanolamine
EOR	Enhanced oil recovery
GHG	Greenhouse gas
HPC	Hot potassium carbonate
MDEA	Methyldiethanolamine
MEA	Monoethanolamine
NET	Negative emission technology
Pz	Piperazine
SDG	Sustainable development goal

# Notations

## Latin letters

$[\text{CO}_2]$	Concentration of $\text{CO}_2$ in bulk solvent [ $\text{mol}/\text{m}^3$ ]
$[\text{CO}_2]_i$	Concentration of $\text{CO}_2$ at the gas-liquid interface [ $\text{mol}/\text{m}^3$ ]
$A$	Arrhenius prefactor [ $\text{m}^3/\text{mol}\cdot\text{s}$ ]
$c_A$	Concentration of species A in the film [ $\text{mol}/\text{m}^3$ ]
$C_B$	Atom concentration of boron [ $\text{mol}/\text{m}^3$ ]
$C_{\text{carbon}}$	Atom concentration of carbon [ $\text{mol}/\text{m}^3$ ]
$C_K$	Atom concentration of potassium [ $\text{mol}/\text{m}^3$ ]
$D_A$	Diffusivity of species A [ $\text{m}^2/\text{s}$ ]
$E$	Enhancement factor [-]
$E_{\text{app}}$	Apparent enhancement factor [-]
$E_a$	Activation energy [ $\text{J}/\text{mol}$ ]
$H$	Henry constant of $\text{CO}_2$ [ $\text{mol}/\text{m}^3\cdot\text{Pa}$ ]
$I$	Ionic strength $I = \frac{1}{2} \sum_A z_A^2 [A]$ [ $\text{mol}/\text{m}^3$ ]
$k_1$	Pseudo-first order reaction rate constant [ $1/\text{s}$ ]
$k_2$	Rate constant for reaction between $\text{CO}_2$ and $\text{OH}^-$ [ $\text{m}^3/\text{mol}\cdot\text{s}$ ]
$k_g$	Gas-side mass transfer coefficient [ $\text{mol}/\text{Pa}\cdot\text{m}^2\cdot\text{s}$ ]
$k_L$	Liquid-side mass transfer coefficient [ $\text{m}/\text{s}$ ]
$k_v$	Rate constant for reaction between $\text{CO}_2$ and $\text{HVO}_4^{2-}$ [ $\text{m}^3/\text{mol}\cdot\text{s}$ ]
$K_1$	Equilibrium constant for reaction (2.VII) [ $\text{mol}/\text{m}^3$ ]
$K_2$	Equilibrium constant for reaction (2.VIII) [ $\text{mol}/\text{m}^3$ ]
$K_g$	Overall mass transfer coefficient [ $\text{mol}/\text{Pa}\cdot\text{m}^2\cdot\text{s}$ ]
$K_w$	Equilibrium constant for reaction (2.IX) [ $(\text{mol}/\text{m}^3)^2$ ]
$l_b$	Length of the magnetic bar [ $\text{m}$ ]
$N_{\text{CO}_2}$	Absorption flux of $\text{CO}_2$ from gas to liquid [ $\text{mol}/\text{m}^2\cdot\text{s}$ ]
$p$	Pressure (total) at time $t$ [ $\text{Pa}$ ]
$p_\infty$	Asymptotic (total) pressure [ $\text{Pa}$ ]

$p_0$	Pressure (total) at time 0 [Pa]
$p_{\text{CO}_2}$	Partial pressure of $\text{CO}_2$ [Pa]
$p_{\text{CO}_2}^*$	Partial pressure of $\text{CO}_2$ at equilibrium [Pa]
$P_{\text{app}}$	Apparent promotion factor [-]
$r_f$	Forward rate of reaction [ $\text{mol}/\text{m}^3 \cdot \text{s}$ ]
$r_A$	Reaction rate of species $A$ in the film [ $\text{mol}/\text{m}^3 \cdot \text{s}$ ]
$R$	Gas constant [ $\text{Pa} \cdot \text{m}^3 / \text{mol} \cdot \text{K}$ ]
$S$	Area of the gas-liquid interface [ $\text{m}^2$ ]
$t$	Time [s]
$T$	Temperature [K]
$V_g$	Volume of gas in the reactor [ $\text{m}^3$ ]
$V_L$	Volume of liquid in the reactor [ $\text{m}^3$ ]

### Dimensionless numbers

$M$	Square of Hatta number
$Re$	Reynolds number $Re = \rho_w \omega l_b^2 / \mu_w$
$Sc$	Schmidt number $Sc = \mu_w / (\rho_w D_w)$
$Sh$	Sherwood number $Sh = k_L l_b / D_w$

### Greek letters

$\alpha$	Carbonate conversion [-]
$\theta$	Solvent loading [-]
$\mu$	Viscosity [ $\text{kg} \cdot \text{m} / \text{s}$ ]
$\rho$	Density [ $\text{kg} / \text{m}^3$ ]
$\omega$	Rotation speed of stirrer $\omega = \text{rpm} / 60$ [1/s]

### Subscripts and superscripts

$w$	Water
$i$	Interface
$\infty$	Infinite dilution



# Chapter 1

## Introduction

### 1.1. Global warming and climate change

The global average temperature has increased significantly over the past century, leading to global warming and climate change. Atmospheric concentrations of carbon dioxide ( $\text{CO}_2$ ) and other greenhouse gases (GHGs), namely, methane ( $\text{CH}_4$ ), nitrous oxide ( $\text{N}_2\text{O}$ ), and fluorinated gases [1], have shown a comparable increase over the same timeframe. Fig. 1.1 shows the development of the atmospheric  $\text{CO}_2$  concentrations since 1850 (panel (a)) together with the global average temperature relative to the 1861–1890 average (panel (b)). The pronounced increase in atmospheric  $\text{CO}_2$  concentrations since the mid-20<sup>th</sup> century directly relates to the growing reliance on fossil fuels to meet global energy demand, with  $\text{CO}_2$  emitted as the by-product of fossil fuel combustion. We know this because the fraction of atmospheric  $\text{CO}_2$  containing  $^{13}\text{C}$  and  $^{14}\text{C}$  isotopes has decreased, while the fraction containing  $^{12}\text{C}$ , characteristic of fossil carbon, has increased [2].

Despite short-term fluctuations, the rise in global average temperatures closely follows the increase in atmospheric  $\text{CO}_2$  and other GHGs\*<sup>†</sup>. The causal relationship between GHG concentrations and global average temperature is well established, and climate models clearly attribute global warming to GHG emissions. These models rely on our understanding of the greenhouse effect, based on which increasing GHG concentrations lead to a positive change in the net radiative flux in the climate system (known as radiative forcing). This change results in the accumulation of energy in the climate system and consequently an increase in global temperature [3, 4].

Global warming has thus far been moderated by Earth’s natural response through terrestrial and oceanic carbon sinks. These sinks have taken up the majority of our  $\text{CO}_2$  emissions, such that only a third of the emitted  $\text{CO}_2$

---

\*NASA. Methane - Earth Indicator

<sup>†</sup>N2OLEVELS.ORG. Present and historical nitrous oxide  $\text{N}_2\text{O}$  levels.

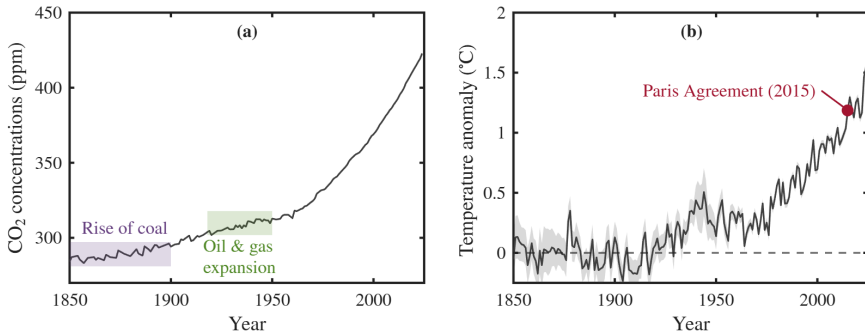


**Figure 1.1:** (a) Atmospheric CO<sub>2</sub> concentration [5], and (b) global average temperature relative to mean value in years 1861–1890 (shade indicates uncertainty) [6]. Data acquired from Our World in Data.

remains in the atmosphere [2]. Continued oceanic uptake of CO<sub>2</sub> has led to ocean acidification. Moreover, warmer surface temperatures reduce both the solubility of CO<sub>2</sub> in the water and the effectiveness of its transport to the deep ocean, thereby weakening the oceanic sink. On land, global warming threatens the integrity of the biosphere through more frequent droughts and forest fires, reducing the capacity of terrestrial carbon sinks. The weakening of natural carbon sinks may be further compounded by processes such as thawing of permafrost and the potential conversion of forests to net CO<sub>2</sub> emitters [2]. Together, these processes accelerate the accumulation of CO<sub>2</sub> in the atmosphere and amplify the broader impacts of climate change, including more frequent extreme weather events, rising sea levels, and higher mortality risks [2, 7].

## 1.2. Becoming net zero

To mitigate the risks of climate change, the Paris Agreement of 2015, signed by nearly all nations, established the goal of limiting global temperature rise relative to pre-industrial levels to below 1.5 °C, and otherwise within a critical threshold of 2 °C. The fact that global warming has already approached the lower limit of 1.5 °C, as seen in Fig. 1.1.(b), highlights the challenge of achieving these ambitions and the urgency of rapid action.

Climate models show that virtually all viable pathways that limit global warming require achieving net-zero, i.e., anthropogenic GHG emissions are balanced by removals from the atmosphere such that a constant radiative forcing can be achieved [3, 4]. To attain net-zero, three sets of mitigation strategies must be pursued: (i) reduction of CO<sub>2</sub> emissions, (ii) reduction of non-CO<sub>2</sub> GHG emissions, and (iii) removal of CO<sub>2</sub> from the atmosphere through negative emission technologies (NETs) [8].

As the most abundant and long-lived GHG, reduction of CO<sub>2</sub> emissions assumes by far the largest share of net-zero mitigation efforts. Optimization of urban areas and changes in consumer behavior, lifestyle, and demand can lead to some emission reductions [9]. However, the primary mitigation pathways involve reducing our dependence on fossil-based carbon through combinations of transition to clean and renewable energy sources, electrification, and improved efficiencies in power production, transport, and industrial sectors. Carbon capture and storage (CCS), applied to fossil CO<sub>2</sub>-emitting industries, represents another emission reduction pathway. In CCS, CO<sub>2</sub> is separated from dilute streams such as combustion flue gas to produce high-purity CO<sub>2</sub>, which is subsequently sequestered on near-permanent timescales in deep geological formations [10–13].

Non-CO<sub>2</sub> greenhouse gases, primarily CH<sub>4</sub> and N<sub>2</sub>O, occur at atmospheric concentrations two to three orders of magnitude lower than CO<sub>2</sub>. Although these gases have significantly shorter atmospheric lifetimes, they exhibit stronger radiative forcing. Reductions in the emissions of these gases can be achieved by phasing out fossil fuels and by preventing emissions at production sources, e.g., agricultural waste, biogas and waste water treatment plants (CH<sub>4</sub>), and chemical plants (N<sub>2</sub>O) [1, 14].

Nevertheless, a group of *hard-to-abate* emitters remain, including the agricultural sector, steel and cement production, and the shipping and aviation industries. Complete elimination of GHG emissions from these sectors is considered unfeasible with available technologies [15]. Atmospheric removal of CO<sub>2</sub> through NETs is therefore required to compensate for these emissions and, beyond net zero, to reduce atmospheric CO<sub>2</sub> concentrations [8, 11, 16–18].

NETs such as afforestation and reforestation, enhanced weathering, and ocean alkalization aim to strengthen natural terrestrial and oceanic carbon sinks by increasing their storage capacity or CO<sub>2</sub> uptake rates. Direct air carbon capture and storage (DACCS) represents another NET pathway that actively removes CO<sub>2</sub> from the atmosphere. Bio-energy with carbon capture and storage (BECCS), which captures CO<sub>2</sub> from biogenic sources, also results in net removal of CO<sub>2</sub> from the atmosphere, provided that the biomass feedstock regrows, thus absorbing the atmospheric CO<sub>2</sub> via photosynthesis [19–21]. NETs are typically evaluated in terms of their scalability and their contribution to net zero goals, as well as costs, land competition with other sectors, bio-diversity impacts, pollution, and the Earth system response [19, 20, 22]. The permanence of geological CO<sub>2</sub> storage, which effectively removes CO<sub>2</sub> from the carbon cycle, distinguishes BECCS and DACCS from sequestration pathways in the biosphere or surface ocean. Together with their potential for large-scale deployment, this permanence makes BECCS and DACCS attractive NET options despite their high cost compared to other NETs, such as afforestation and reforestation [21, 23, 24].

### 1.3. Swedish context

The Climate Policy Framework adopted by the Swedish Parliament in 2018 established a national net zero target for 2045. The framework sets interim emission-reduction targets of 63% by 2030 and 75% by 2040 compared to 1990 levels, with the 2045 target requiring an emission reduction of at least 85%. The remainder, approximately 11 Mton CO<sub>2</sub>-equivalents per year, represent hard-to-abate emissions that must be compensated for by NETs or mitigation projects abroad [25].

Sweden is well-positioned for BECCS deployment due to its existing large-scale biomass-based infrastructure, particularly within the pulp and paper industry, combined heat and power (CHP) plants, and waste incinerators [26, 27]. The country also benefits from close proximity and shipping access to the North Sea, where most CO<sub>2</sub> storage facilities are located. In addition, access to clean<sup>‡</sup> and low-cost electricity<sup>§</sup> in Sweden supports the energy demand for carbon capture processes. The estimated negative emission potential for BECCS in Sweden is 25–28 Mton CO<sub>2</sub>/y [26, 27]. This potential is sufficient not only to meet Sweden’s net zero target but also to generate additional negative emissions that could be sold to international actors, thereby creating economic incentives for carbon capture deployment [27].

These factors have contributed to Sweden becoming a frontrunner in BECCS deployment. Several utility facilities across the country, including Stockholm Exergi Värtaverket<sup>¶</sup> (CHP) and Öresundskraft Filbornaverket<sup>||</sup> (waste incinerator) are planning to begin BECCS operation by 2030, creating a combined negative emission capacity of nearly 1 Mton CO<sub>2</sub>/y.

### 1.4. Aim statement

The research presented in this thesis was conducted within the context of ongoing efforts to mitigate GHG emissions. It focuses on absorption-based processes for CO<sub>2</sub> capture using aqueous potassium carbonate (K<sub>2</sub>CO<sub>3</sub>) as solvent. Technologies based on aqueous K<sub>2</sub>CO<sub>3</sub>, commonly referred to as hot potassium carbonate (HPC) processes, have been employed in gas purification for decades and are therefore well established. Their application to BECCS, however, is recent and follows their selection in several BECCS projects (e.g., Stockholm Exergi AB [28]).

Despite the apparent advantages of the HPC process, its performance is limited by the slow absorption rate of CO<sub>2</sub> into aqueous K<sub>2</sub>CO<sub>3</sub>. This thesis

---

<sup>‡</sup>International Energy Agency (IEA). Energy system of Sweden. (Version: 2024)

<sup>§</sup>Eurostat. Electricity price statistics. (Last update: Oct. 2025)

<sup>¶</sup>Stockholm Exergi. BECCS Stockholm. (Accessed: Mar. 2026)

<sup>||</sup>Öresundskraft. Vad är CCS och varför är det viktigt för Helsingborg. (Last update: Mar. 2025)

addresses this limitation by investigating the use of solvent additives known as rate promoters. In particular, the study focuses on vanadium pentoxide ( $V_2O_5$ ) and boric acid ( $B(OH)_3$ ), which form the basis of industrial Catacarb solvent blends\*\*[29]. Accordingly, the aims of this thesis are:

- Design of an experimental setup to enable robust and reproducible measurements of  $CO_2$  absorption rates.
- Screening of different rate promoters to qualitatively assess their influence on the absorption rate.
- Detailed characterization of the rate promoters vanadium pentoxide ( $V_2O_5$ ) and boric acid ( $B(OH)_3$ ) in terms of absorption and reaction rates, using unpromoted  $K_2CO_3$  as a baseline.
- Development of kinetic rate models for unpromoted as well as vanadium and boron-promoted  $K_2CO_3$ , capable of describing the experimental observations.

This thesis provides comprehensive absorption rate data on promoted and unpromoted aqueous  $K_2CO_3$  across operational conditions relevant to HPC applications. The experimental observations are supported with mechanistic explanations, linking the measured rates to the underlying  $CO_2$  reactions in the solvent. In particular, this work shows that  $V_2O_5$  exhibits a comparable rate enhancement to amine-based rate promoters, such as monoethanolamine (MEA) and glycine. The results further identify operational and concentration ranges where  $V_2O_5$  is most effective as a rate promoter and demonstrate that the promotion occurs through complex formation between  $CO_2$  and a monovanadate species. Moreover, the thesis demonstrates that  $B(OH)_3$  has a minor influence on the reaction kinetics of  $CO_2$ , but increases the absorption capacity of aqueous  $K_2CO_3$ . These findings contribute to the large-scale implementation of HPC-based carbon capture by rationalizing the roles of  $V_2O_5$  and  $B(OH)_3$ . In addition, the kinetic rate models developed in this work reduce uncertainties during process design and support process and solvent-blend optimization.

This summary is structured as follows. In the next chapter, a brief background is provided on state of the art of the CCS supply chain. This is followed by a description of the absorption process and of aqueous  $K_2CO_3$  and amine-based solvents, reflecting their prominence in industrial carbon capture. A review of rate promoters for aqueous  $K_2CO_3$  is then presented. Subsequent chapters describe the experimental setup and procedure, the methods for interpreting and processing of experimental data, and the presentation and discussion of the results. The thesis concludes with a summary of the appended papers, reflections on contributions of this research to the Sustainable Development Goals (SDGs), and potential directions for future research.

---

\*\*Catacarb Homepage. (Accessed: March 2026)

# Chapter 2

## Background

### 2.1. Carbon dioxide supply chain

Carbon capture and storage (CCS) consists of a series of interdependent steps. First, *(i)* CO<sub>2</sub> is separated from a feed gas (dilute stream) in the carbon capture process, producing a high-purity CO<sub>2</sub> stream. Next, *(ii)* the captured CO<sub>2</sub> undergoes conditioning, which includes removal of trace gases to meet end-use or storage requirements, as well as compression and liquefaction. The CCS chain further involves *(iii)* transportation from capture and conditioning facilities to the storage sites, where *(iv)* the CO<sub>2</sub> is geologically stored in suitable rock formations and thereby removed from the active carbon cycle. Alternatively, CO<sub>2</sub> may be utilized, e.g., as a feedstock for products or for enhanced oil recovery (EOR), in which case it remains within the active carbon cycle (a value chain referred to as carbon capture and utilization).

The different steps are typically carried out by different operators. For CCS to be realized at scale, all parts of the supply chain must be deployed and matured simultaneously [30]. Furthermore, requirements imposed by one stage can influence process selection and system design at other stages of the supply chain.

#### 2.1.1. Carbon capture

Carbon capture refers to the separation of CO<sub>2</sub> from a dilute gas stream to produce a concentrated CO<sub>2</sub> product. As gas separation is a non-spontaneous process, all carbon capture technologies require energy input in the form of heat, electricity, or both. The energetic cost of capture per unit mass of CO<sub>2</sub> is strongly influenced by the CO<sub>2</sub> concentration in the feed gas. A tenfold decrease in feed gas concentration approximately doubles the Gibbs free energy of demixing. Moreover, achieving high CO<sub>2</sub> purities from increasingly dilute

streams incurs additional penalties due to a decreasing second law efficiency (i.e., minimum work to actual work) [31–33].

Point-source CO<sub>2</sub> emitters, e.g., heat and power plants and the steel and cement industries, account for a substantial share of global CO<sub>2</sub> emissions. These emissions arise primarily from the combustion of carbon-based fuels (coal, methane, biomass, waste) for energy production [34], making these sectors key targets for CCS deployment. These industries largely rely on conventional combustion processes (using excess air) and produce flue gases composed mainly of N<sub>2</sub>, with CO<sub>2</sub> concentrations of up to 20 vol% on a dry basis. Such high CO<sub>2</sub> concentrations result in significantly lower energy demand for carbon capture compared to DACCS, where CO<sub>2</sub> concentrations are 400–500 ppm. Post-combustion carbon capture aims to retrofit capture units to existing combustion systems with minimal modifications to the upstream process (in contrast to oxyfuel combustion or pre-combustion processes), thereby avoiding complete replacement of the energy infrastructure [35–37].

Among different separation processes, absorption is the most established and cost-effective technology for large-scale post-combustion carbon capture. Its relative insensitivity to impurities, combined with decades of industrial experience in gas treating, renders operational challenges well understood and manageable. Owing to its maturity and technical reliability, absorption is expected to constitute a substantial share of first-generation carbon capture facilities [36–38]. Other technologies, adsorption and membrane-based processes, benefit from relative simplicity and modular configurations, but become competitive only at smaller scales or as costs are driven down through expanded deployment [38, 39].

### 2.1.2. Conditioning and transport

Carbon capture facilities will be more geographically dispersed than geological storage sites, which are limited to specific locations with suitable subsurface formations. This is particularly the case in Europe, where most planned geological storage capacity is located offshore in the North Sea\* or the Adriatic<sup>†</sup>, and onshore in Iceland<sup>‡</sup>. Consequently, CO<sub>2</sub> transport forms an important logistic component of CCS chains [30]. Requirements imposed on the captured CO<sub>2</sub> by transport and storage operators determine downstream processes to the carbon capture unit. These processes are collectively referred here to as gas conditioning, and consist of units for removal of impurities from the captured CO<sub>2</sub> and its pressurization or liquefaction to meet transport specifications.

The composition of gas impurities depends on the upstream processes and may include moisture, light gases (e.g., N<sub>2</sub>, O<sub>2</sub>), hydrocarbons, and sulfur compounds (H<sub>2</sub>S, SO<sub>x</sub>) [40]. The presence of impurities in the CO<sub>2</sub> both limits the

---

\*Northern Lights. Homepage. (Accessed: March 2026)

<sup>†</sup>Ravenna CCS. Homepage. (Accessed: March 2026)

<sup>‡</sup>Carbfix Coda Terminal. Homepage. (Accessed: March 2026)

transport capacity and introduces parasitic energy demand for the compression of non-CO<sub>2</sub> components. Some impurities can further cause operational issues such as corrosion and freezing during the CO<sub>2</sub> transport or storage [40–42].

Depending on the mode of transport, CO<sub>2</sub> must be compressed and even liquefied to cryogenic conditions. Both approaches rely on multiple stages of compressors, intercoolers, and condensers to increase pressure while controlling temperature. Liquefaction can be achieved in an open-cycle process through isenthalpic expansion of compressed CO<sub>2</sub> (typically 60–80 bar) to transport pressures. Alternatively, CO<sub>2</sub> can be liquefied in a closed-cycle process using the latent heat of an external refrigerant (e.g., ammonia, propane). In this configuration, CO<sub>2</sub> is compressed only moderately above transport pressure, shifting part of the energy demand to refrigerating the coolant [42].

The electricity demand for liquefying CO<sub>2</sub> is within ranges of 60–120 kWh/ton CO<sub>2</sub>, depending on process configuration, inlet pressure from the capture unit, and target conditions for transport [40, 42]. Open-cycle designs are more feasible for more extreme cryogenic conditions (lower transport pressures) for which common refrigerants become ineffective. However, under conditions where both options are possible, closed-cycle liquefaction requires less energy [41–43].

Transport of CO<sub>2</sub> can be done continuously by pipelines or batch-wise in containers. Pipeline transport occurs at near-ambient temperatures (10–20 °C), with CO<sub>2</sub> in gaseous form (20–30 bar) or, alternatively, as a dense fluid (100–150 bar) to reduce the pipeline footprint. This mode of transport benefits from economies of scale and lower emissions and operating costs [30]. However, pipeline infrastructure in Europe is currently limited and largely confined to short connections between coastal terminals and offshore storage sites. Expansion of pipeline networks requires significant investment and becomes viable only upon deployment of CCS at scale [30, 44, 45].

Batch-wise transport is therefore expected to dominate early phases of CCS deployment in Europe, using trucks, rail, and barges to deliver CO<sub>2</sub> containers to shipping hubs, followed by ship-transport to offshore storage sites. However, reliance on fossil fuel-based transport leads to indirect CO<sub>2</sub> emissions that may reach up to  $\approx 20\%$  of the stored CO<sub>2</sub>, depending on travel distance and vehicle type [46]. In batch-wise transport, CO<sub>2</sub> is transported as a liquid at around -27 °C and 16 barA, reflecting the container conditions of CO<sub>2</sub> for food and beverage industries. Lower temperatures (e.g., -46 °C and 8 barA) increase liquid density, thereby reducing transport costs. However, transport under higher temperature conditions is expected to dominate initially due to technological maturity and lower liquefaction energy demand [30, 45, 47, 48].

### 2.1.3. Geological storage

Global geological storage capacity is estimated at 5,000–40,000 Gton CO<sub>2</sub> under optimistic assumptions [49, 50] and 1,300–2,700 Gton CO<sub>2</sub> under more

conservative assumptions [50]. Given cumulative anthropogenic emissions of approximately 1,800 Gton CO<sub>2</sub> since pre-industrial times, these capacities are, in principle, sufficient to support long-term mitigation strategies [51].

Key risks associated with geological storage include induced seismicity, CO<sub>2</sub> leakage to the surface or into shallow groundwater, and contamination of potable aquifers by displaced brine. These risks impose strict site selection criteria and require extensive site characterization and long-term monitoring beyond the injection period [49, 50]. In addition, the presence of impurities in the injected CO<sub>2</sub> can affect phase behavior and well integrity, influencing both storage capacity and storage security [52, 53]. As a result, storage operators impose stringent purity requirements exceeding 99 mol% CO<sub>2</sub> (e.g., Northern Lights), which in turn constrain conditioning requirements at upstream capture facilities [54].

The primary storage options include saline aquifers, depleted gas and oil fields, and basalt formations. Saline aquifers are porous formations which contain concentrated brine not suitable for human consumption or agriculture. They are geographically widespread, offer large storage capacities and high injection rates, and benefit from extensive field experience [49, 53]. Depleted hydrocarbon fields provide well-characterized reservoirs and existing infrastructure, but are geographically limited. Moreover, legacy wells (originating from hydrocarbon extraction) introduce additional leakage risks and monitoring requirements [49, 51, 53]. Basalt formations enable rapid mineralization of injected CO<sub>2</sub>, reducing long-term leakage risks and eliminating the need for caprock sealing. This allows injection at relatively shallow depths (350–500 m), but requires significant water input since CO<sub>2</sub> is injected in dissolved form [53, 55]. All these storage options are at advanced stages of implementation across northern Europe, with projects such as Northern Lights (saline aquifers), Porthos (depleted fields), and the Coda Terminal (basalt formations) already in (or close to) operation, with a total storage capacity of over 95 Mton CO<sub>2</sub> [53].

#### 2.1.4. Utilization

Utilization of CO<sub>2</sub> encompasses a wide range of activities, from established uses in food and beverage industries to broader definitions that include binding of CO<sub>2</sub> through biomass growth or mineral carbonation in construction materials, where CO<sub>2</sub> may be bound on timescales of decades to centuries [56].

Catalytic or electrochemical conversion of CO<sub>2</sub> to chemicals and hydrocarbon fuels represents another utilization pathway [57]. However, this approach does not result in removal of CO<sub>2</sub> from the active carbon cycle, as CO<sub>2</sub> is eventually re-emitted upon combustion. Consequently, chemical conversion of CO<sub>2</sub> requires carbon-free electricity or hydrogen input to avoid net emissions. Given the re-emission of CO<sub>2</sub> and high energy demand, the overall mitigation potential of CO<sub>2</sub> conversion remains limited, with estimates suggesting this pathway to

contribute less than 0.5% to global emission reduction targets (less than 4 Gton CO<sub>2</sub> by 2050) [58].

Projected CO<sub>2</sub> demand for enhanced oil recovery (EOR) is substantially larger, with estimated capacities ranging from 40–140 Gton CO<sub>2</sub>. EOR is operationally similar to geological storage, i.e., dense or supercritical CO<sub>2</sub> is injected into partially depleted oil or gas reservoirs. However, the primary objective of EOR is to displace and extract the remaining hydrocarbons from the reservoir, while offsetting the capture costs by producing crude oil or gas [56, 58]. Hydrocarbons extracted through EOR are eventually combusted, leading to additional CO<sub>2</sub> emissions. Net-negative operation may be achieved during early injection phases if more CO<sub>2</sub> is injected into the reservoir than that released through combustion. However, this balance reverses over time, resulting in net-positive cumulative emissions from the reservoir [58, 59].

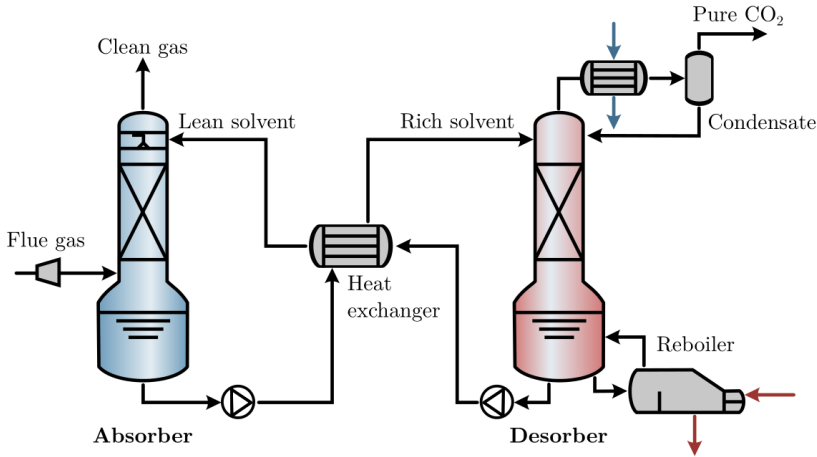
## 2.2. Carbon capture by absorption

Fig. 2.1 shows a diagram of an absorption-based carbon capture process. The process consists of an absorber and a desorber column, operating in counter-current mode, with a solvent that circulates between the two columns. The columns are equipped with packings, i.e., internal structures that provide a large interface area between gas and liquid phases, thereby improving mass transfer rates [60, 61].

In the absorber, CO<sub>2</sub> is removed from the flue gas and taken up by the solvent, resulting in a CO<sub>2</sub>-clean gas exiting at the top of the column and a CO<sub>2</sub>-rich solvent leaving from the bottom of the column. Compression of the incoming flue gas may be required to increase the CO<sub>2</sub> partial pressure and thus the driving force for absorption [61–63].

The desorber operates at temperatures close to the boiling point of the solvent, increasing the driving force for CO<sub>2</sub> desorption. In the desorber, CO<sub>2</sub> is released from the rich solvent in the presence of steam, which acts as a carrier for the desorbed CO<sub>2</sub> and maintains the desorption temperature throughout the column. The steam is generated in a reboiler at the bottom of the desorber, in which the solvent is partially evaporated. The CO<sub>2</sub>-steam mixture leaving at the top of the desorber is cooled and condensed. The condensed water is refluxed back to the column, and the remaining gas, consisting primarily of CO<sub>2</sub>, exits the process for downstream conditioning. The regenerated lean solvent from the reboiler is recirculated to the absorber. A cross-flow heat exchanger is employed to cool the hot lean solvent to absorption temperatures while simultaneously preheating the cold rich solvent prior to desorption [61–63].

The main energy demands of the carbon capture process arise from heat supplied to the reboiler and electricity used for flue gas compression. Energy recovery occurs primarily via the overhead condenser and the expansion of the clean gas after absorption. Overall energy consumption can also be lowered by



**Figure 2.1:** Schematics of absorption-based carbon capture process. Credit: Matthias U. Babler.

modifications which aim at improving heat integration with the emitter plant and efficient use of energy streams via flow splitting or flash drums [38, 64–66].

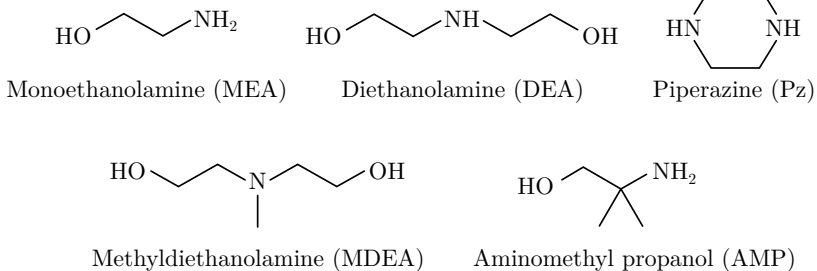
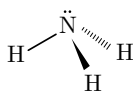
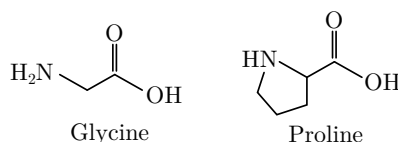
One of the primary factors determining the configuration of the capture process, equipment sizing, operating conditions, and heat and electricity demand is the choice of solvent [61, 63, 64]. Accordingly, the remainder of this section discusses the most established solvent types for post-combustion carbon capture, namely, aqueous solutions of amines, ammonia, amino acids, and carbonates [63, 67–69]. Hydroxides, which are prominent in direct air capture, are only discussed insofar as relevant to carbonates given their similar chemistry.

### 2.2.1. Amine-based solvents

A broad range of amines exhibit high capacity and fast reactivity toward  $\text{CO}_2$ . These characteristics make amines highly effective for absorption processes. The most prominent amines (see Fig. 2.2) have been extensively studied from lab to pilot scale, and their handling and operation are well established in industry [61, 69].

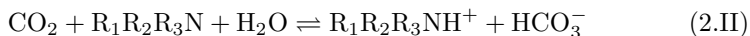
The substituents on the nitrogen atom strongly influence amine performance in terms of absorption. Primary and secondary amines such as MEA, DEA, and Pz (see Fig. 2.2 for full names) contain at least one hydrogen substituent and react with  $\text{CO}_2$  to form carbamates. The stoichiometry of this reaction, written for the nominal amine  $\text{R}_1\text{R}_2\text{NH}$ , reads as [69, 70]:



**Amines****Ammonia****Amino acids**

**Figure 2.2:** Molecular structure of select amines and amino acids, and ammonia.

Tertiary amines (e.g., MDEA), lacking N–H bonds, cannot form carbamates. The main product of CO<sub>2</sub> reaction with tertiary amines is instead bicarbonate, in a stoichiometry which reads as [70, 71]:



The protonated amine is a shared product regardless of the reaction pathway, reflecting the acidic nature of CO<sub>2</sub>. Carbamate formation consumes two moles of amine per mole of CO<sub>2</sub>, whereas bicarbonate formation proceeds on a 1:1 mole ratio of amine to CO<sub>2</sub>. Upon complete consumption of the amine, CO<sub>2</sub> absorption proceeds physically. Consequently, for the same amine concentration, the chemical capacity of tertiary amines is double that of primary or secondary amines. Piperazine (Pz) represents a special case due to additional dicarbamate formation, resulting in a stoichiometric coefficient (reaction 2.I) between 1 and 2 for Pz [70, 72].

For tertiary amines, bicarbonate formation proceeds via CO<sub>2</sub> hydrolysis, with the amine providing the capacity and supply of hydroxide ions for maintaining reaction (2.II) at a reasonable rate. Due to the inherent alkalinity of primary and secondary amines, the hydrolysis pathway also contributes to the CO<sub>2</sub> reaction in these solutions. However, the direct reaction between CO<sub>2</sub> and amine to form carbamates is significantly faster and dominates the overall reaction and absorption rates [69, 70].

Sterically-hindered amines (e.g., AMP), i.e., primary or secondary amines with bulky substituents, form carbamates at somewhat slower rates than conventional amines. The structure of hindered amines renders the carbamate unstable

such that it dissociates into bicarbonate upon formation, thereby re-releasing the amine. Consequently, they react with  $\text{CO}_2$  following the stoichiometry of reaction (2.II) [71]. Blends of tertiary or hindered amines with primary or secondary amines (e.g., AMP/Pz (CESAR1) or MDEA/Pz) are employed to combine the high absorption capacities of the former with the fast reactions of the latter [73–75].

Due to the fast reaction of  $\text{CO}_2$  in amine systems, the absorption column can be operated at atmospheric pressure. To increase the absorption capacity and to prevent amine losses due to evaporation, absorption temperatures are maintained at 40–60 °C. Emissions of amines and their degradation products are further mitigated using water or acid wash in the form of additional packing above the absorber [38, 63, 76]. Desorption columns for amines are operated at over-atmospheric pressures, typically 1.5–2 barA (corresponding to 110–120 °C), depending on the amine-type. Higher temperatures favor desorption both thermodynamically and kinetically, producing a leaner solvent for absorption [67, 76].

Despite their positive characteristics, the use of amines presents several operational challenges. The heat demand for breaking the strong carbamate bonds and releasing the  $\text{CO}_2$  is high [63]. Oxygen in the flue gas leads to oxidative degradation of amines in the absorber, forming aldehydes, carboxylic acids, and amides [69]. Additionally, amine reactions with  $\text{NO}_x$ , either during capture or via amine aerosols in the atmosphere, lead to formation of carcinogenic nitrosamines [69, 77]. Thermal degradation occurs via carbamate polymerization under desorption temperatures, thereby constraining the upper temperature limit for solvent regeneration [69]. MEA degrades relatively quickly compared to other amines, whereas tertiary and sterically-hindered amines generally exhibit greater stability [69]. Nevertheless, extensive industrial experience exists in managing corrosion, solvent reclamation, and the disposal or destruction of spent solvents, evident in the handling of MEA in gas cleaning operations [61].

### 2.2.2. Ammonia

The chemistry of  $\text{CO}_2$  absorption in aqueous ammonia is similar to that of amines and proceeds via carbamate formation. The lower stability of ammonium carbamate relative to carbamates formed by primary and secondary amines leads to higher absorption capacities, without the same degradation or nitrosamine formation issues [78]. Presence of  $\text{SO}_2$  and  $\text{NO}_2$  instead leads to the formation and precipitation of ammonium sulfate and nitrate salts, respectively, which can be recovered as fertilizers [79].

The thermal stability of ammonia enables operation of the desorber at higher pressures compared to amines, while the high volatility of ammonia necessitates absorption at ambient or colder temperatures (5–15 °C), as in the chilled ammonia process (CAP) [68, 80]. Under these temperatures, the  $\text{CO}_2$  absorption rate in ammonia is a factor two lower than that of MEA. In addition,

the low solubility of the reaction product, ammonium bicarbonate, particularly at high loadings, imposes a lower limit on the absorption temperature [81].

The process layout for ammonia-based capture shares many features with that of amine systems. The primary differences are the need for chillers and additional units for ammonia recovery, namely a secondary absorption-desorption unit and a reclamation unit downstream of solvent regeneration. Despite the need for additional reboilers, both techno-economic analyses and pilot studies suggest significant reductions in heat consumption for CAP relative to amines, albeit at the expense of extra cooling demand [68, 79, 80]. Operating in a mode that allows for the formation of ammonium bicarbonate precipitates, where  $\text{CO}_2$  is desorbed from a concentrated slurry (e.g., via a rich solvent cyclone), reduces the amount of solvent processed in the desorber. Although this decreases the sensible head demand for solvent regeneration, pilot-scale tests report operational instability in this configuration, with only marginal energy savings [80].

### 2.2.3. Amino acids

Structurally, amino acids consist of a carbon atom bonded to a carboxylic acid group and an amino group (Fig. 2.2). The presence of the amino group renders the chemistry and reaction rate of amino acids with  $\text{CO}_2$  similar to those of amines. Since the deprotonated amino acid is the species that forms carbamates in reaction with  $\text{CO}_2$ , absorption solvents based on amino acids contain a hydroxide salt in equimolar amounts [69, 82–84].

Several characteristics make amino acids attractive as solvent technology. Because the solvent species are predominantly ionic, evaporative losses of amino acids are lower than for amines. Many amino acids are considered non-toxic, with some occurring naturally, and exhibit lower oxidative degradation compared to common amines such as MEA or Pz [69, 85, 86].

On the other hand, amino acid salts and their carbamate products have lower solubilities than amines and exhibit poor thermal stability under desorption temperatures [69, 85]. The reboiler duties for glycinate and sarcosinate, two prominent amino acid systems, are reported to be higher than that for MEA by 50% [87–90]. A pilot study on glycinate salts also indicates overall poorer performance compared to MEA, where lower cyclic capacity necessitated significantly higher liquid-to-gas flow ratios in the absorber [89]. It should be noted, however, that this study was conducted in a column designed for amine operation. Considering the reported operational issues, it appears that optimal process design and operating conditions for amino acid-based solvents may differ significantly from those of amines.

Recent research on amino acids has identified a promising approach to circumvent conventional desorption by replacing it with a chemical loop. In this approach, solid bis-iminoguanidine, in contact with loaded solvent, protonates and crystallizes as a bicarbonate salt, thereby regenerating the alkaline form of

the amino acid on timescales comparable to absorption.  $\text{CO}_2$  is subsequently recovered from the precipitated salt by heating at temperatures as low as  $80\text{ }^\circ\text{C}$ , enabling the use of low-grade heat [91, 92].

#### 2.2.4. Carbonates

Carbonate-based absorption solvents have been widely used in hot potassium carbonate (HPC) or Benfield processes for gas cleaning applications [61, 62]. Potassium carbonate ( $\text{K}_2\text{CO}_3$ ) is preferred due to the higher solubility of both carbonate and bicarbonate salts compared to other counter-ions (e.g., sodium, lithium) [93]. Carbonates are virtually non-degradable and non-volatile, rendering solvent losses negligible [94]. These characteristics make carbonate-based solvents particularly attractive for carbon capture applications near urban areas, where elevated  $\text{NO}_x$  concentrations and amine aerosol emissions could otherwise lead to atmospheric nitrosamine formation. Despite the additional electricity demand for flue gas compression, the HPC process becomes competitive with amine-based technologies in heat production applications. This advantage arises from the lower regeneration temperature and the higher heat recovery potential of the HPC processes, enabling the production of low-grade heat suitable for applications such as district heating [95, 96].

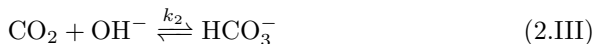
Literature also reports lower reboiler duties as a benefit of aqueous  $\text{K}_2\text{CO}_3$  [94]. The latter aligns with a lower heat of absorption ( $15\text{--}25\text{ kJ/mol}$  [67, 97]) compared to that of amines ( $80\text{--}85\text{ kJ/mol}$  for MEA [67, 87]). However, this is not immediately clear from post-combustion carbon capture studies where reboiler duties for the HPC process span a wide range of  $3\text{--}5\text{ GJ/ton CO}_2$  [64, 65, 96], overlapping with values for MEA [89, 96, 98]. These comparable reboiler duties may arise from a larger latent heat demand for regenerating aqueous  $\text{K}_2\text{CO}_3$ .

A main limitation of aqueous  $\text{K}_2\text{CO}_3$  is the slow absorption rate of  $\text{CO}_2$ , necessitating high absorption temperatures and pressures. The original Benfield process addresses this by operating under pressure swing, with absorption pressures of  $15\text{--}20\text{ bar}$  and temperatures as high as  $120\text{ }^\circ\text{C}$  [61–63]. However, this implementation is not feasible in post-combustion carbon capture applications due to the high compression requirements. The HPC process for post-combustion carbon capture is instead operated with absorber pressures as high as  $8\text{ barA}$  and near-atmospheric desorption. The temperature swing is smaller than in amine systems, with absorber temperatures up to  $90\text{ }^\circ\text{C}$  and desorption at  $\approx 100\text{ }^\circ\text{C}$ , resulting in smaller cross-flow heat exchangers [99, 100].

Under these operating conditions, column sizing for HPC process is significantly larger than for amine-based processes [63]. To address this limitation, rate promoters are added to aqueous  $\text{K}_2\text{CO}_3$  to enhance the  $\text{CO}_2$  absorption rates, providing additional flexibility in operation (by lowering absorption pressure) or design (by reducing column size) [61, 64].

### 2.3. Chemistry of aqueous $\text{K}_2\text{CO}_3$

**Reaction mechanism.** Absorption of  $\text{CO}_2$  in aqueous  $\text{K}_2\text{CO}_3$  proceeds via reaction with hydroxide ions:



Reaction (2.III), with forward rate constant  $k_2$ , is treated as elementary, with a forward rate expression that reads as  $r_f = k_2[\text{CO}_2][\text{OH}^-]$  ([.] refers to species concentration). Hydrolysis of  $\text{CO}_2$  by water also occurs, but its rate constant is significantly lower than  $k_2[\text{OH}^-]$  at the pH values relevant for carbonate absorption (pH > 9) [101]. Hydrolysis of  $\text{CO}_2$  by water is therefore neglected for the present analysis.

The role of carbonate is to maintain the hydroxide concentration through the  $\text{CO}_3^{2-}/\text{HCO}_3^-$  buffer equilibrium [93, 102, 103]:



This deprotonation is effectively instantaneous relative to reaction (2.III). On the timescale of reaction (2.III), the hydroxide concentration can therefore be considered constant. As a result, reaction (2.III) is rate-limiting and governs  $\text{CO}_2$  absorption in aqueous  $\text{K}_2\text{CO}_3$ . Combining the two reactions yields the overall stoichiometry [102, 103]:



That is, carbonate and  $\text{CO}_2$  react on 1:1 molar basis to produce two moles of bicarbonate.

The chemistry of aqueous  $\text{K}_2\text{CO}_3$  is closely related to that of hydroxide solutions. Absorption of  $\text{CO}_2$  into aqueous KOH, NaOH, or LiOH proceeds via reaction (2.III), which, due to the higher pH, proceeds substantially faster than in  $\text{K}_2\text{CO}_3$ . However, in hydroxide solutions, reaction (2.IV) shifts in the opposite direction and the overall stoichiometry (with potassium as counter-ion) becomes:



In conventional desorption columns, regeneration of KOH from  $\text{K}_2\text{CO}_3$  is impractical because the equilibrium  $\text{CO}_2$  partial pressure is extremely low; in practice, regeneration would require complete evaporation of the solvent [92, 93]. Regeneration of hydroxide solvents instead relies on a chemical looping process in which  $\text{CO}_2$  is first precipitated as  $\text{BaCO}_3$  or  $\text{CaCO}_3$ , followed by thermal decomposition to reform  $\text{Ba}(\text{OH})_2$  or  $\text{Ca}(\text{OH})_2$  [92].

**Speciation.** Speciation in aqueous KOH and K<sub>2</sub>CO<sub>3</sub> is governed by the same set of equilibria:



where  $K$  refers to the equilibrium constants. The mass action laws in this work are written in terms of concentrations rather than activities. Deviations arising from finite concentrations and ionic effects are incorporated into reaction rate constants.

In principle, CO<sub>2</sub> acts as an acid and lowers the pH through proton release, which is neutralized by OH<sup>-</sup> or CO<sub>3</sub><sup>2-</sup>. The amount of CO<sub>2</sub> taken up by the solvent is expressed through the solvent loading  $\theta$ , defined here in terms of atom concentrations of potassium ( $C_K$ ) and carbon ( $C_{\text{carbon}}$ ) in the solvent:

$$\theta = \frac{C_{\text{carbon}}}{\frac{1}{2}C_K} - 1 \quad (2.1)$$

The definition is consistent with those commonly used in the literature, while highlighting the link between aqueous KOH and K<sub>2</sub>CO<sub>3</sub>. Specifically, a solvent at  $\theta = 0$  corresponds to a blend of water and K<sub>2</sub>CO<sub>3</sub>; a solvent at  $\theta = -1$  ( $C_{\text{carbon}} = 0$ ) to a blend of water and KOH;  $\theta = 1$  to a blend of water and KHCO<sub>3</sub>; and  $\theta > 1$  to a blend which contains both KHCO<sub>3</sub> and free-CO<sub>2</sub>.

Fig. 2.3 shows the speciation of aqueous K<sub>2</sub>CO<sub>3</sub> as a function of the solvent loading, in form of pH (panel (a)) and species concentrations (panel (b)). Speciation was calculated by solving the equilibria of reactions (2.VII)-(2.IX) together with charge balance and carbon atom balance. The resulting profiles can be divided into three regions, distinguished by trends in concentration and dominant reaction regimes.

In the  $\theta$  range of -1 to 0 (region (I)), KOH is limiting and absorption follows the stoichiometry of reaction (2.VI). The high pH ( $> 12$ ) ensures that absorbed CO<sub>2</sub> is present predominantly as CO<sub>3</sub><sup>2-</sup>, while bicarbonate and free-CO<sub>2</sub> concentrations remain negligible. In region (II) ( $0 < \theta < 1$ ), K<sub>2</sub>CO<sub>3</sub> is limiting and absorption follows the stoichiometry of reaction (2.V). Coexistence of CO<sub>3</sub><sup>2-</sup> and HCO<sub>3</sub><sup>-</sup> establishes a buffer, maintaining a relatively stable pH ( $8.5 < \text{pH} < 11.5$ ) as solvent loading increases. The buffer capacity is exhausted at  $\theta = 1$ , reflected in the flattening of the HCO<sub>3</sub><sup>-</sup> profile. Region (III) ( $\theta > 1$ ) denotes a fully exhausted buffer, with essentially no remaining chemical absorption capacity. In this region, CO<sub>2</sub> uptake is primarily due to physical dissolution, and species concentrations other than dissolved CO<sub>2</sub> change only marginally.

The low hydroxide concentrations ( $10^{-5}$ – $10^{-3}$  M) in the relevant solvent loading range for aqueous K<sub>2</sub>CO<sub>3</sub> (region (II)) contribute to the low CO<sub>2</sub>

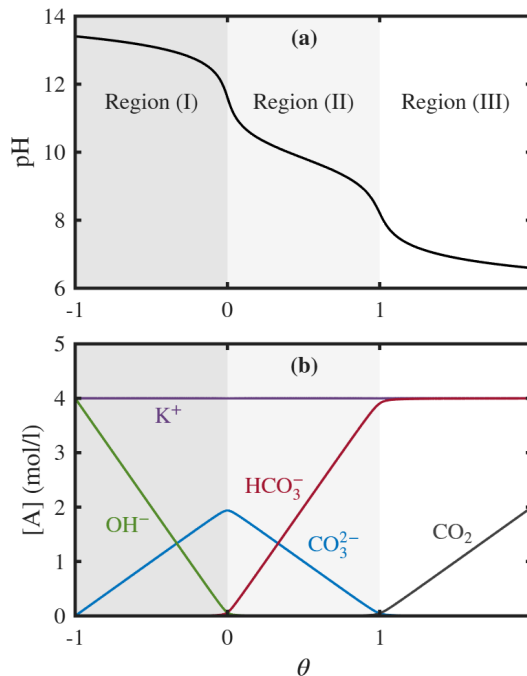


**Figure 2.3:** (a) pH and (b) species concentrations as functions of the solvent loading  $\theta$  for aqueous  $\text{K}_2\text{CO}_3$ . Temperature:  $70\text{ }^\circ\text{C}$ . Potassium concentration ( $C_K$ ): 4 M. Equilibrium constants adopted from Imle et al. [104].

reaction rates and, consequently, its slow absorption rate. Rate promoters increase the absorption rate by catalyzing the  $\text{CO}_2$  reaction in the solvent. In such systems,  $\text{K}_2\text{CO}_3$  supplies the chemical capacity for absorption, while the promoter enables a faster reaction pathway.

## 2.4. Rate promoters for aqueous $\text{K}_2\text{CO}_3$

Rate promoters enhance the reaction rate of  $\text{CO}_2$  in the solvent by providing an additional pathway for conversion of  $\text{CO}_2$  to bicarbonate. This occurs via the reaction of  $\text{CO}_2$  with an active species of the rate promoter, typically a basic form given the acidic nature of  $\text{CO}_2$ . A general catalytic mechanism for the reaction of  $\text{CO}_2$  with a rate promoter has been proposed by Astarita et al.

[103]. The two-step reaction mechanism reads as:



In the first step,  $CO_2$  reacts with the active base ( $B$ ) to produce an intermediate, e.g., a complex ( $BCO_2$ ). This is followed by reformation of the active species through the reaction of the intermediate with hydroxide, releasing  $CO_2$  as bicarbonate. The overall stoichiometry is equivalent to reaction (2.III), highlighting that the rate promoter essentially acts as catalyst for this reaction. The role of the carbonate buffer is implicit in supplying the hydroxide ions required for intermediate dissociation. According to this mechanism, the forward rate of  $CO_2$  conversion arises from contributions of reactions (2.III) and (2.X). If both steps are treated as elementary, the forward reaction rate  $r_f$  reads as [103, 105]:

$$r_f = [CO_2](k_2[OH^-] + k_b[B]) \quad (2.2)$$

where the product  $k_b[B]$  represents the contribution of the rate promoter to the  $CO_2$  reaction rate. The rate constant  $k_b$  is an inherent property of the rate promoter and a function of temperature, following Arrhenius behavior. The concentration of the active species  $[B]$  depends on promoter speciation, total promoter concentration, and pH.

The reactivity of rate promoters has been suggested to follow a Brønsted-type relation, in which higher reaction rate constants correlate with higher  $pK_a$ . In one such study, Sharma and Danckwerts [105] investigated the reaction of  $CO_2$  in buffered solutions containing sulfite, inorganic acids (e.g., germanic acid, silicic acid), chloral hydrates and alcoholates, aldehydes (e.g., formaldehyde hydrate), and sugars (e.g., sucrose). Their results showed that the Brønsted relation is broadly followed. However, their data suggest the  $CO_2$  reaction to be at least an order of magnitude slower for all these potential rate promoters compared to arsenite, despite the latter having an intermediate  $pK_a$  value among the studied compounds.

Rate constants measured by Phan et al. [106] suggest that phosphates, arsenates, and sulfates also have limited, if any, catalytic behavior. The results of Phan et al. [106, 107] indicate that both phosphites and vanadates have significantly higher  $CO_2$  activity than the other investigated alternatives. Phan et al. [106, 107] proposed that the  $CO_2$  reaction proceeds via a hydrated active base, whose electrostatic charge was shown to broadly correlate with the rate constant  $k_b$ , with more negatively charged species correlating with higher  $k_b$ . Kim et al. [108] proposed a similar hypothesis, showing that deprotonated hydrogen peroxide and hypochlorite, with high electronegativity on the nucleophile atom (central oxygen and chloride atoms, respectively), exhibit substantially greater rate enhancement than monoborate (boron atom).

The remainder of this section discusses prominent rate promoters, considering their industrial application or their prominence in the scientific literature. Amines, such as diethanolamine (Benfield process) [109], the amino acid glycine

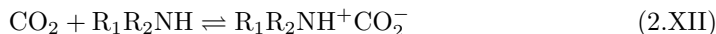
(Giammarco-Vetrocoke process) [61], as well as vanadium pentoxide and boric acid (Catacarb process) [29] are among the rate promoters used in gas cleaning applications. Despite a catalytic effect on the same orders of magnitude as vanadates, the use of carcinogenic arsenite is now obsolete [61, 103]. Newer generations of rate promoters, developed specifically for carbon capture, include the enzyme carbonic anhydrase and piperazine, both of which have undergone extensive lab-scale and pilot-scale studies [110–114].

### 2.4.1. Amines and amino acids

Given their fast reaction with  $\text{CO}_2$ , primary and secondary amines and amino acids are effective rate promoters. However, degradation of these rate promoters introduces the same issues as when they are used as base solvents [86]. Literature has shown that prominent amines such as MEA, DEA, and Pz effectively enhance  $\text{CO}_2$  absorption rates. Pz, in particular, exhibits high stability and fast reaction rates, with absorption rates a decade higher than the unpromoted  $\text{K}_2\text{CO}_3$ , approaching those of aqueous MEA [72, 111, 115, 116].

Even higher rate enhancements have been reported by Thee et al. [117] upon addition of potassium salts of glycinate, prolinatate, and sarcosinate to aqueous  $\text{K}_2\text{CO}_3$ . However, this enhancement was accompanied by an increase in pH by 1–3 units, which significantly increases the rate of  $\text{CO}_2$  and  $\text{OH}^-$  reaction. The screening experiments of Li et al. [118] provide a more consistent comparison. They show that absorption rates into 1 M  $\text{K}_2\text{CO}_3$  in the presence of amino acid salts are higher than those for the unpromoted solvent over a wide solvent loading range, although absorption rates remain slower compared to MEA solutions. The absorption rates were largely similar across the tested amino acids, except at low solvent loadings, where argininate and lysinate exhibited higher absorption rates than glycinate. The data of Li et al. [118] further indicate a lower  $\text{CO}_2$  absorption capacity in the presence of glycinate and lysinate compared to the unpromoted  $\text{K}_2\text{CO}_3$ , but a higher capacity in the presence of argininate.

The intermediate species ( $\text{BCO}_2$ ) in the case of amines and amino acids is the corresponding carbamate, whose formation is described via a two-step zwitterion reaction mechanism. In the zwitterion mechanism,  $\text{CO}_2$  reacts with the active amine to form carbamic acid (a zwitterion), which subsequently undergoes rapid deprotonation to form carbamate [72, 82, 83, 119]:



Here,  $\text{B}'$  denotes a proton-accepting base. In the absence of carbonates,  $\text{B}'$  corresponds to the alkaline form of the amine or amino acid, and the combination of reactions (2.XII) and (2.XIII) leads to reaction (2.I) [70]. In aqueous  $\text{K}_2\text{CO}_3$ , both the active amine (or amino acid) and  $\text{CO}_3^{2-}$  can act as bases. Given their similar basicity, the contributions of  $\text{CO}_3^{2-}$  and the active amine (or amino

acid) to reaction (2.XIII) are comparable, resulting in lower amine consumption per mole of  $CO_2$  compared to systems without carbonate [115]. By treating the carbamic acid intermediate ( $R_1R_2NH^+CO_2^-$ ) at quasi-steady state, the zwitterion mechanism explains the apparent reaction order with respect to the active amine or amino acid, which has been observed to exceed unity (e.g., DEA, sarcosine) [83, 115, 119].

### 2.4.2. Enzymes

The enzyme carbonic anhydrase (CA) can catalyze  $CO_2$  hydrolysis in the pH range relevant to operation of aqueous  $K_2CO_3$ . Even crude CA at dosages of tens of ppm can increase absorption rates by more than a factor of three [120], while engineered CA (Novonesis, previously Novozymes A/S) developed specifically for carbon capture, can achieve rate enhancements of up to a factor of eight [113, 121].

Several issues stall the expansion of enzyme-based carbon capture. In particular, enzyme activity decreases with increasing temperature [120], and the high temperatures in the desorber can lead to rapid degradation of the enzyme [122, 123]. Even engineered CA has been shown to lose most of its activity within 100 days at moderate temperatures (50–60 °C), although it exhibits high resistance to chloride, sulfate, and nitrate impurities [112]. The rapid loss of enzyme activity may necessitate additional units for separation of degraded enzyme, while the high costs associated with enzyme synthesis could make continuous dosing economically challenging [123].

To prevent thermal denaturation of enzymes, absorption occurs at relatively low temperatures (30–40 °C) and desorption is performed under vacuum (10–60 kPa), limiting the boiling point of the solvent to 50–70 °C. The low bicarbonate solubility at these temperatures constrains  $K_2CO_3$  concentration and, consequently, the absorption capacity [114, 122].

While the enzyme does increase  $CO_2$  reaction rates at low temperatures [122], these rates are comparable to those of unpromoted  $K_2CO_3$  at 80–90 °C typical for HPC operation. This suggests that, under optimal operating conditions, differences in column size or flue gas compression between enzyme-promoted and unpromoted systems may be smaller than implied by the large rate enhancements reported at low temperatures. Accordingly, at their current state of the art, the primary benefit of enzymatic promoters is the possibility of using low-grade heat for desorption due to operation under vacuum [114, 122]. The latter could presumably be enabled by catalysis of the reverse reaction, allowing desorption under similar column lengths to absorption despite the lower temperatures compared to the unpromoted  $K_2CO_3$ .

### 2.4.3. Vanadium pentoxide

Vanadium pentoxide ( $V_2O_5$ ) exhibits several characteristics that make it an attractive rate promoter. Namely, it is non-volatile and, being in its highest oxidation state, is resistant to oxidative degradation. As part of the Catacarb blend, it can be operated under conditions similar to the unpromoted solvent without significantly affecting the reboiler duty [29, 124, 125]. In addition to enhancing the  $CO_2$  absorption rate,  $V_2O_5$  acts as a corrosion inhibitor in aqueous  $K_2CO_3$ . This effect occurs presumably via a redox reaction converting  $V^{5+}$  to  $V^{4+}$ , and in turn, oxidizing iron(II) to iron(III), forming a protective oxide layer on the steel surface [110, 125, 126]. Additional reduction of  $V^{5+}$  may occur in the presence of impurities that can act as reducing agents (e.g.,  $H_2S$ ) [127]. However, dosing with a strong oxidant (e.g.,  $H_2O_2$ ) or the oxygen in the flue gas could maintain the high  $V^{5+}$  concentrations [125, 128].

Addition of vanadium pentoxide to aqueous  $K_2CO_3$  has been shown to increase the absorption rate by a factor of 2 or more, depending on the vanadium concentration, although the rate enhancement decreases at high vanadium concentrations. This effect is ascribed to the availability of the active vanadate species, which is dictated by the speciation of vanadium(V) in alkaline solutions [129, 130].

The identity of the active species remains uncertain. Qinghua et al. [129] assumed the divanadate ion  $V_2O_7^{4-}$  to be the active species, but do not motivate this assumption. Phan et al. [107] considered hydrogen monovanadate  $HVO_4^{2-}$  as the active species, which, considering the low concentrations involved, appears more reasonable. The most comprehensive work in this regard has been performed by Nicholas et al. [130], who correlated trends in their absorption rate measurements to both  $HVO_4^{2-}$  and hydrogen divanadate  $HV_2O_7^{3-}$ . Nevertheless, the conclusions of Nicholas et al. [130] require further scrutiny, as their indirect estimation of vanadate speciation could be erroneous. Specifically, it involved UV-vis spectrometry to infer solvent loading, from which species concentrations were estimated by interpolating  $^{51}V$ -NMR spectra of a calibration set based on highly concentrated solutions. In particular, the activity of  $HV_2O_7^{3-}$  is questionable, as its concentration is expected to be very low within most of their experimental pH ranges ( $> 11$ ).

### 2.4.4. Boric acid

Boric acid ( $B(OH)_3$ ) or borate salts are stable, non-volatile additives that form the second component of Catacarb blends. Borates are reported to significantly increase the effectiveness of  $V_2O_5$  by increasing the  $CO_2$  absorption capacity [29, 124]. However, this effect is not explicitly supported by the scientific literature. Instead, several studies on vapor-liquid equilibrium of aqueous  $K_2CO_3$  promoted with boric acid demonstrate an increase in equilibrium partial

pressure of  $CO_2$  upon addition of boric acid (especially in the high solvent loading ranges) [131–133].

Earlier studies suggested that borates strongly catalyze  $CO_2$  hydrolysis, although these conclusions were based on limited datasets [105, 134, 135]. More recent literature suggests that boric acid exhibits limited rate enhancement [108, 133, 136], a conclusion also reflected in pilot studies by the CO2CRC project [137], where boric acid was employed in aqueous  $K_2CO_3$  in the absence of  $V_2O_5$ .

The observed rate enhancement in the presence of boron is typically associated with a direct reaction between monoborate ( $B(OH)_4^-$ ) and  $CO_2$ , following the catalytic mechanism described in section 2.4 (reactions (2.X) and (2.XI)) [108, 136, 138]. However, Imle et al. [104] report that their NMR studies did not identify any stable intermediate or reaction product between  $CO_2$  and borates. The absence of such a complex, despite the extensive study of borates in aqueous and ocean chemistry, suggests that the applicability of the catalytic pathway of reactions (2.X) and (2.XI) to borates remains uncertain.

# Chapter 3

## Methods

### 3.1. Gas-liquid contactor configurations

Measurement of absorption rates imposes several requirements on the experimental configuration. Namely, the gas-liquid contactor must provide a constant and well-defined gas-liquid interface area throughout the absorption experiment, and an observable property must change upon absorption in a manner that can be measured accurately. Furthermore, sufficient agitation is required to reduce the sensitivity of the system to perturbations by decreasing diffusion distances. Based on their configuration, gas-liquid contactors can broadly be classified into three categories (see Fig. 3.1): continuous gas-continuous liquid, continuous gas-batch liquid, and batch gas-batch liquid.

**Continuous gas–continuous liquid.** Wetted-wall columns [72, 136] (Fig. 3.1.(a)), liquid jets [139], and strings of discs or spheres [102, 140] are typically employed in fully continuous configurations. In addition to the contactor, these systems require auxiliary units such as pumps, mass flow controllers, gas pre-saturation, and gas analysis [72, 136, 140]. Despite their operational complexity, the various adjustable variables (e.g., flow rates, gas composition, pressure) make these systems flexible.

The transient mass balances for  $\text{CO}_2$ , expressed in terms of partial pressure ( $p_{\text{CO}_2}$ ) and the outgoing solvent loading ( $\theta$ ) for aqueous  $\text{K}_2\text{CO}_3$  (see eq. (2.1)), assuming ideal gas behavior and treating each phase as a continuous stirred-tank reactor, read as:

$$\frac{dp_{\text{CO}_2}}{dt} = \frac{G}{V_g}(p_{\text{CO}_2, \text{in}} - p_{\text{CO}_2}) - N_{\text{CO}_2}RT \frac{S}{V_g} \quad (3.1)$$

$$\frac{d\theta}{dt} = \frac{L}{V_L}(\theta_{\text{in}} - \theta) + N_{\text{CO}_2} \frac{S}{1/2C_K V_L} \quad (3.2)$$

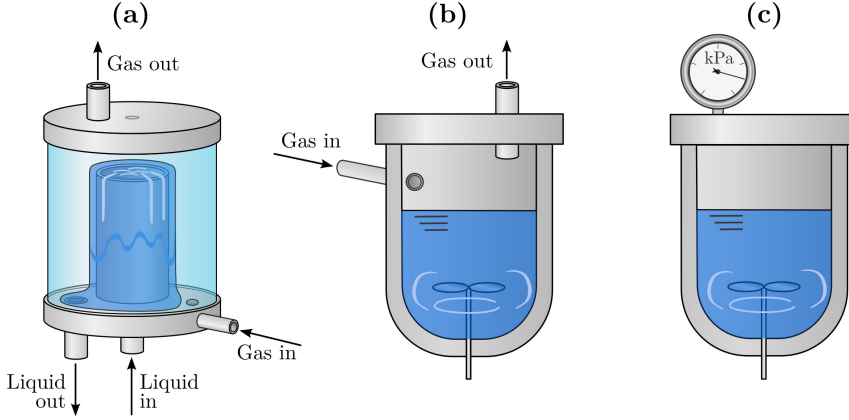


**Figure 3.1:** Schematic diagrams of operational modes for absorption experiments: (a) continuous gas-continuous liquid; (b) continuous gas-batch liquid; and (c) batch gas-batch liquid. Credit: Matthaus U. Babler.

where  $G$  and  $L$  are the volumetric gas and liquid flow rates, respectively,  $V_g$  and  $V_L$  are the volumes occupied by the gas and the liquid, respectively,  $N_{\text{CO}_2}$  is the absorption flux,  $S$  is the interface area,  $R$  is the gas constant, and  $T$  is temperature. Subscript *in* denotes inlet conditions. Eqs. (3.1)-(3.2) are derived under the assumption that gas and liquid flow rates do not change significantly after passing through the contactor.

For a constant  $N_{\text{CO}_2}$ , eqs. (3.1)-(3.2), subject to the initial conditions  $p_{\text{CO}_2}|_{t=0} = p_{\text{CO}_2, \text{in}}$  and  $\theta|_{t=0} = \theta_{\text{in}}$ , admit an analytical solution that reads as:

$$p_{\text{CO}_2} = p_{\text{CO}_2, \text{in}} - \tau_g \left[ 1 - \exp(-t/\tau_g) \right] N_{\text{CO}_2} RT \frac{S}{V_g} \quad (3.3)$$

$$\theta = \theta_{\text{in}} + \tau_L \left[ 1 - \exp(-t/\tau_L) \right] N_{\text{CO}_2} \frac{S}{\frac{1}{2} C_K V_L} \quad (3.4)$$

where  $\tau_g = V_g/G$  and  $\tau_L = V_L/L$  are the gas and liquid residence times, respectively. Eqs. (3.3)-(3.4) show that, following a perturbation (e.g., shift from air to  $\text{CO}_2$ -rich gas), the time required for the system to reach steady state depends on  $\tau_g$  and  $\tau_L$ , while the absorption flux governs the steady state composition of the outlet streams. Accordingly, the experimental design aims to lower the residence times, while the steady state operation allows for multiple measurements of absorption flux for a single experiment.

Under typical operation, the liquid residence time is much shorter than that of the gas. For sufficiently high solvent concentration ( $C_K \approx 1 \text{ M}$ ), this results in  $\theta \approx \theta_{\text{in}}$ , making changes in solvent loading too small to determine

experimentally. Consequently, monitoring the outlet gas stream is sufficient for determining the absorption rate.

**Continuous gas–batch liquid.** In semi-continuous systems, gas flows over or through a stirred liquid phase (Fig. 3.1.(b)). While bubbling reactors fall within this category, in such setups, the gas-liquid interface area is not well defined. These setups cover wide solvent loading ranges, and hence, are used in early screening studies [108, 118]. The transient liquid-side mass balance for this system reads as:

$$\frac{d\theta}{dt} = N_{\text{CO}_2} \frac{S}{\frac{1}{2}C_K V_L} \quad (3.5)$$

In this configuration, the solvent loading increases continuously as  $\text{CO}_2$  is absorbed, eventually reaching steady state as the solvent becomes saturated in  $\text{CO}_2$ . The rate of change in  $\theta$  is proportional to the absorption flux. Consequently, monitoring the time evolution of  $\theta$  via, e.g., pH, spectroscopy, or titration, provides a measure of the absorption rate.

Under typical experimental conditions, the solvent loading increases significantly over the course of the experiment, rendering semi-continuous systems more suitable for measuring average fluxes and assessing solvent performance over large solvent loading ranges in a single experiment. Composition-representative fluxes can be estimated by dividing the experimental data into segments where the change in  $\theta$  is sufficiently small ( $< 1\%$ ).

**Batch gas–batch liquid.** Fully batch configurations involve relatively few components and are operationally simpler than other designs. Suitable contactors are typically pressure vessels, as operation may span from sub-atmospheric pressures ( $\approx 1$  kPa) to over-atmospheric pressures (for high temperature experiments). The liquid mass balance reads the same as eq. (3.5), while the gas-side mass balance reads as:

$$\frac{dp_{\text{CO}_2}}{dt} = -N_{\text{CO}_2} RT \frac{S}{V_g} \quad (3.6)$$

Eq. (3.6) shows that the rate of change of  $\text{CO}_2$  partial pressure is proportional to  $N_{\text{CO}_2}$ . Hence, a batch system allows for single point measurements of  $N_{\text{CO}_2}$  as a function of  $p_{\text{CO}_2}$  and  $\theta$ .

In a typical bench-scale setup, large pressure decays can be achieved without significantly altering the solvent composition. This becomes evident upon dividing eq. (3.6) by eq. (3.5), leading to:

$$-dp_{\text{CO}_2} = \frac{1}{2}C_K RT \frac{V_L}{V_g} d\theta \quad (3.7)$$

The prefactor on the right-hand side is typically on the order of  $\approx 1$  MPa. Accordingly, a 1% change in solvent loading corresponds to a pressure decrease of  $\approx 10$  kPa. This decrease in pressure can be monitored accurately with standard instrumentation. The relatively small variation in  $\theta$  under these

conditions indicates that gas pressure is a suitable observable property for absorption, provided that  $\text{CO}_2$  is the only component transferring between gas and liquid. As such, the rate of pressure decay provides a direct measure of the absorption flux.

A batch configuration was selected for the experiments in this work due to its simplicity and relatively short experimental duration. These systems provide both transient rate data and the equilibrium pressure corresponding to the solvent composition, as the experiment proceeds until  $N_{\text{CO}_2} = 0$ . Nevertheless, the same interface phenomena (dictating  $N_{\text{CO}_2}$ ) apply to all contactor types or configurations, with the primary distinction between them lying in their macroscopic mass balances.

### 3.2. Experimental setup

Fig. 3.2 shows a diagram of the batch experimental setup employed in this work. The gas-liquid contactor consists of a stirred stainless steel reactor (Miniclave, Büchiglas, 400 ml) loaded with solvent. The reactor is connected to a gas storage unit (double-ended gas sampling cylinder, Swagelok), from which known amounts of  $\text{CO}_2$  were injected into the reactor. The system was evacuated of air prior to operation. Thus, the gas phase consists primarily of  $\text{CO}_2$  saturated with water, and the absorption rate could be determined from pressure decay. Pressure was monitored using two sensors (DMP 331i, BD Sensors) with absolute ranges of 0–100( $\pm 0.1$ ) kPa and 0–1000( $\pm 1$ ) kPa. Liquid-phase mixing was provided by magnetic stirring, and internal baffles ensured a relatively flat gas-liquid interface (inspected visually prior to sealing the reactor).

In a typical experiment, the reactor was filled with 200 ml solvent and was sealed from the atmosphere. The entire system was evacuated at room temperature, reaching a pressure of 2–3 kPa, corresponding to the vapor pressure at room temperature. After evacuation, the valve between the reactor and the storage unit was closed and the storage unit was pressurized to 200–500 kPa, depending on the required amount of  $\text{CO}_2$ . Subsequently, water circulation and stirring in the reactor were initiated, and the system was allowed to equilibrate to the set temperature and its corresponding pressure. Rotation of the magnetic stirrer was verified during heating via the liquid temperature response; upon stopping the stirring, the rate of temperature increase decreased noticeably.

The absorption experiment was initiated by briefly opening the valve between the storage unit and the reactor, resulting in a rapid pressure increase in the reactor due to  $\text{CO}_2$  injection. The amount of injected  $\text{CO}_2$  was regulated using a secondary needle valve. Given the short opening period, the  $\text{CO}_2$  taken up by the solvent during the transfer from the storage unit to the reactor is assumed negligible. Following valve closure, the pressure gradually decreased as  $\text{CO}_2$  was absorbed by the liquid, and stabilized to equilibrium. Absorption was accompanied by a temperature increase due to the exothermic reaction,

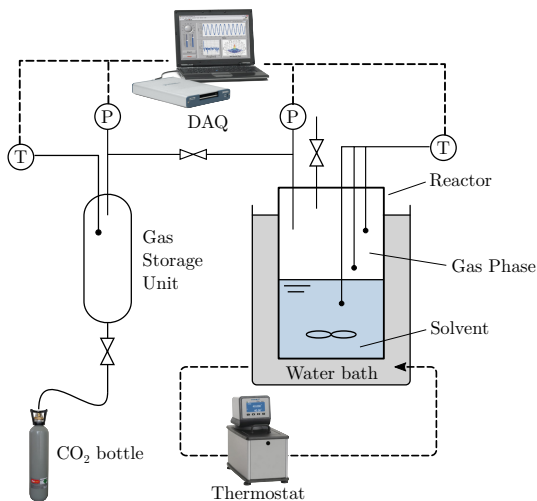


**Figure 3.2:** Process flow diagram for experimental setup. Adapted from **Paper II**.

reaching up to 0.5 °C depending on the absorption rate. These temperature variations are considered negligible in the data analysis.

Changes in solvent loading were determined by a mass balance over the storage unit and the reactor before and after each injection:

$$\theta_f = \theta_i + \frac{1}{\frac{1}{2}C_K V_L} \left[ \frac{\bar{p}_{S,i} - \bar{p}_{S,f}}{\bar{T}_s} \frac{V_S}{R} - \left( \frac{\bar{p}_{\infty,f}}{\bar{T}_{g,f}} - \frac{\bar{p}_{\infty,i}}{\bar{T}_{g,i}} \right) \frac{V_g}{R} \right] \quad (3.8)$$

where overbars denote mean values of temperature and pressure over stable periods of the experiments. The subscript  $S$  refers to the storage unit,  $g$  refers to the gas phase, and  $i$  and  $f$  refer to properties before and after injection, respectively. The pressure and loading terms in eq. (3.8) are illustrated in Fig. 3.3.

In most experimental runs, multiple injections were performed before re-opening the reactor. The procedure for subsequent injections followed the same protocol. When a new temperature set-point was required, the system was allowed to re-equilibrate prior to injection. Larger intermediate injections (300–500 kPa) were occasionally performed to increase solvent loadings (5–7% for 25 wt% K<sub>2</sub>CO<sub>3</sub>), thereby reducing chemical consumption.

### 3.3. Data processing

The absorption flux  $N_{\text{CO}_2}$  is expressed proportional to a driving force:

$$N_{\text{CO}_2} = K_g (p_{\text{CO}_2} - p_{\text{CO}_2}^*) \quad (3.9)$$

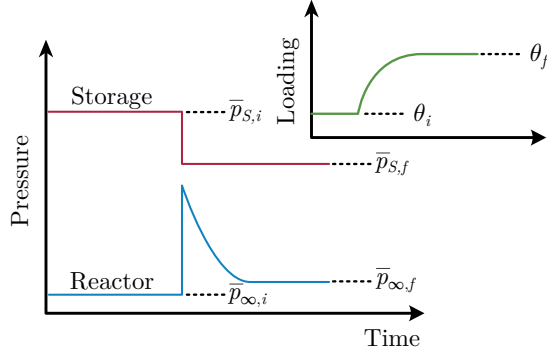


**Figure 3.3:** Schematics of pressure evolution in the reactor and the storage unit before and after an injection. Inset: solvent loading profile upon CO<sub>2</sub> injection.

where  $p_{\text{CO}_2}^*$  is the equilibrium partial pressure of CO<sub>2</sub> and  $K_g$  is the overall mass transfer coefficient which lumps together the reaction-diffusion phenomena at the gas-liquid interface. The derivation of eq. (3.9), as well as a physical interpretation of  $K_g$  are provided in the appendix (chapter A), using the framework of film theory.

In the evacuated reactor, gas impurities are negligible, and the water vapor pressure, as the only other significant gas component, varies only weakly with solvent composition [97, 141]. Accordingly, the driving force in eq. (3.9) can be described in terms of total pressure in the reactor:

$$p_{\text{CO}_2} - p_{\text{CO}_2}^* = p - p_{\infty} \quad (3.10)$$

where  $p$  is the total pressure in the reactor and  $p_{\infty}$  is the asymptotic pressure corresponding to the equilibrium pressures of CO<sub>2</sub> and water.

Under conditions relevant to this work, in which the depletion of non-CO<sub>2</sub> species at the interface is negligible (i.e., pseudo-first order reaction regime applies; see section A.2.2),  $K_g$  is independent of the driving force ( $p - p_{\infty}$ ) and depends only on the reaction-diffusion at the interface. In chemical absorption, due to the high capacity for CO<sub>2</sub> and the small change in the solvent loading during the experiment, both  $K_g$  and  $p_{\infty}$  can be assumed constant. Combining eqs. (3.9) and (3.10) with eq. (3.6), and integrating subject to the initial condition  $p|_{t=0} = p_0$  yields:

$$\frac{p - p_{\infty}}{p_0 - p_{\infty}} = \exp\left(-K_g RT \frac{S}{V_g} t\right) \quad (3.11)$$

For physical absorption (e.g., in water), absorbed CO<sub>2</sub> remains in free form, and the equilibrium pressure is not constant throughout the experiment. In

this case, the time evolution of free- $\text{CO}_2$  in water reads as:

$$\frac{d[\text{CO}_2]}{dt} = H_w \frac{dp_{\text{CO}_2}^*}{dt} = N_{\text{CO}_2} \frac{S}{V_L} \quad (3.12)$$

where  $[\text{CO}_2]$  is the bulk  $\text{CO}_2$  concentration and  $H_w$  is the Henry constant for  $\text{CO}_2$  in water. Dividing eq. (3.12) by eq. (3.6) and integrating with  $[\text{CO}_2]|_{t=0} = 0$  gives:

$$p_{\text{CO}_2}^* = (p_0 - p) \frac{1}{RT H_w} \frac{V_g}{V_L} \quad (3.13)$$

Integration of eq. (3.6) together with eqs. (3.10)-(3.13) yields the pressure evolution for a physical solvent:

$$\frac{p - p_\infty}{p_0 - p_\infty} = \exp \left\{ -K_{g,w} \left( RT \frac{S}{V_g} + \frac{S}{V_L H_w} \right) t \right\} \quad (3.14)$$

where  $K_{g,w}$  is the overall mass transfer coefficient for water.

Eqs. (3.11) and (3.14) show that the decrease of pressure in the reactor for both solvent and water can be described as an exponential decay, with the exponent proportional to the overall mass transfer coefficient  $K_g$  (for solvent; eq. (3.11)) or  $K_{g,w}$  (for water; eq. (3.14)).

To estimate kinetic rate constants from  $K_g$ , absorption experiments were conducted in the pseudo-first order reaction regime (see section A.2.2). In aqueous  $\text{K}_2\text{CO}_3$ , the conditions for achieving the pseudo-first order reaction regime are dictated by the Danckwerts criterion (eq. (A.19)), which can be satisfied by lowering the  $\text{CO}_2$  injection pressures. Under these conditions, the pressure decay becomes nearly independent of the stirring rate (which controls diffusion distances), and  $K_g$  can be related directly to the reaction rate via the pseudo-first order rate constant  $k_1$  (see section A.2.2 for the relations). The forward reaction rate for  $\text{CO}_2$  hydrolysis with  $\text{OH}^-$  (reaction (2.III)) reads as:

$$r_f = k_2[\text{CO}_2][\text{OH}^-] \quad (3.15)$$

where  $r_f$  is the forward reaction rate. The pseudo-first order rate constant corresponding to this reaction reads as:

$$k_1 = k_2[\text{OH}^-] \quad (3.16)$$

Thus, variations in hydroxide concentration (controlled by solvent loading) affect  $k_1$  and, consequently,  $K_g$ . Determination of reaction rate constants therefore requires knowledge of species concentrations. In this work, speciation was estimated by solving the chemical equilibrium (charge and atom balances combined with laws of mass action) assuming an ideal solution. The use of equilibrium concentrations for determining rate constants is justified under the pseudo-first order reaction regime, which dictates that the bulk liquid remains at equilibrium.

## Chapter 4

# Results and discussion

Absorption experiments were conducted using various blends of aqueous  $\text{K}_2\text{CO}_3$ , with and without rate promoters, over temperature ranges of 27–85 °C and solvent loadings ( $\theta$ ) spanning from low, non-buffered carbonate solutions to more  $\text{CO}_2$ -saturated regions (the method for preparing loaded samples by blending chemicals is described in the appendix).

Experiments with water were used to isolate the contribution of diffusion, represented by the liquid-side mass transfer coefficient  $k_L$  (see section A.1), which was subsequently used in the kinetic analysis of aqueous  $\text{K}_2\text{CO}_3$  blends. Unpromoted  $\text{K}_2\text{CO}_3$  was used to validate the experimental setup by comparing the measured vapor-liquid equilibrium pressure with literature data and by confirming the validity of the gas phase mass balances over the setup. Unpromoted  $\text{K}_2\text{CO}_3$  also serves as a baseline for assessing the performance of rate promoters and for isolating the reaction rate between  $\text{CO}_2$  and  $\text{OH}^-$ . The study then examines absorption in the presence of vanadium pentoxide and boric acid, comparing their performance with that of MEA, piperazine, and glycine rate promoters, and investigating their reaction mechanisms with  $\text{CO}_2$ .

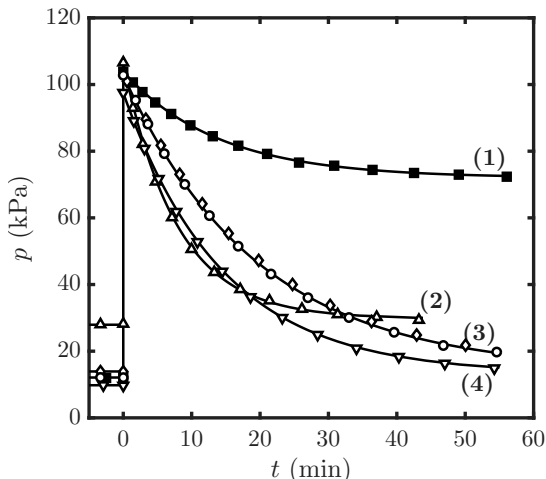
### 4.1. Raw pressure-time data

Fig. 4.1 shows the pressure evolution in the reactor over time for unpromoted  $\text{K}_2\text{CO}_3$  at different solvent loadings and temperatures. Data for water as solvent (curve 1) are also shown. Dataset (3) includes two sets of experiments (circles and diamonds), whose overlap demonstrates the reproducibility of the absorption experiments.

Before injection, the solvent is at equilibrium with the gas phase, with a higher temperature corresponding to a higher vapor-liquid equilibrium pressure. Upon introduction of  $\text{CO}_2$  ( $t = 0$ ), the pressure increases rapidly within a few seconds, followed by a gradual decrease over time due to  $\text{CO}_2$  absorption. The relaxation time serves as a qualitative indicator of the absorption rate and

is faster at low solvent loadings and high temperatures, reflecting the faster reaction of  $\text{CO}_2$ . For aqueous  $\text{K}_2\text{CO}_3$  (cases (2)-(4)), the high capacity for  $\text{CO}_2$  results in stabilization of pressure close to its pre-injection value. In contrast, for water (case (1)), where  $\text{CO}_2$  dissolves in free form, the pressure stabilizes to a significantly higher value than before injection.

The lines in Fig. 4.1 represent exponential fits to the pressure-time data. Eq. (3.11) is used for aqueous  $\text{K}_2\text{CO}_3$  (fitting parameters:  $p_\infty$  and  $K_g$ ), while eq. (3.14) is used for water (fitting parameters:  $p_\infty$  and  $K_{g,w}$ ). The relative uncertainties in asymptotic pressure and overall mass transfer coefficients (estimated from 95% confidence interval in parameter fitting), across different absorption experiments, are below 0.1% and 3–5%, respectively. The low uncertainties confirm the validity of the exponential pressure decay behavior.



**Figure 4.1:** Pressure decay inside the reactor. Symbols: downsampled data. Lines: exponential fits. Open symbols: aqueous 25 wt%  $\text{K}_2\text{CO}_3$ . (1) Water, 50 °C; (2) 10% loading, 70 °C; (3) 30% loading, 50 °C; (4) 10% loading, 50 °C. Adapted from **Paper II**.

## 4.2. Setup characterization

### 4.2.1. Mass balance over setup

The solvent loading after absorption was estimated from mass balances over the gas phase in the reactor and the storage unit (eq. (3.8)). At the end of each experiment, the solvent loading was also determined by titration of the liquid phase (see section B.2). Fig. 4.2 presents these measurements as a parity plot

for unpromoted  $\text{K}_2\text{CO}_3$ , showing that the solvent loading calculated from gas phase mass balance (including cases with multiple intermediate injections and temperature steps) agree well with values obtained from titration. This close agreement indicates that the gas pressure provides an accurate measure of  $\text{CO}_2$  in the gas phase and its uptake by the liquid, and supports the assumptions that  $\text{CO}_2$  absorption during injection and losses during evacuation are negligible.

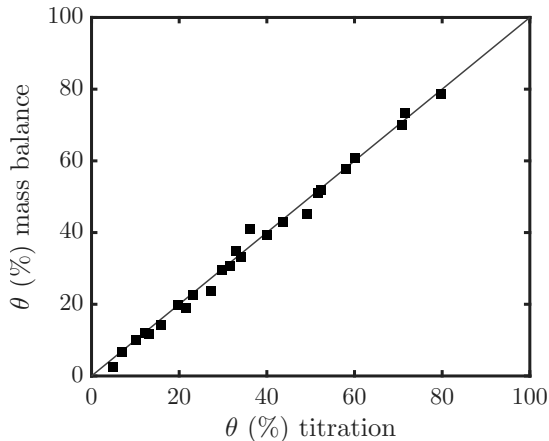


**Figure 4.2:** Solvent loading estimated by mass balance over the system (eq. (3.8)) against solvent loading measured by titration (eq. (B.9)) for unpromoted  $\text{K}_2\text{CO}_3$ .

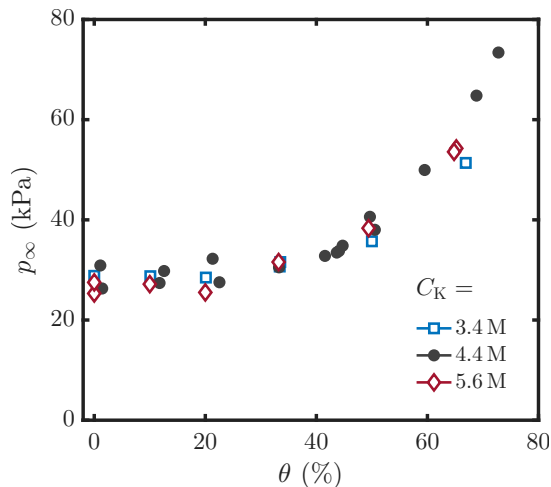
#### 4.2.2. Vapor-liquid equilibrium

Fig. 4.3 shows the asymptotic pressure  $p_\infty$  as a function of solvent loading  $\theta$  for 25 wt%  $\text{K}_2\text{CO}_3$ , together with data from Tosh et al. [97] at 70 °C. The close agreement between the present data (25 wt%  $\text{K}_2\text{CO}_3$ ) and literature values (20 and 30 wt%  $\text{K}_2\text{CO}_3$ ) supports the validity of the setup.

Fluctuations at low solvent loading ( $\theta < 20\%$ ), where water vapor dominates the gas phase equilibrium, indicate that the setup is not well suited for accurate vapor-liquid equilibrium measurements in this region. Such measurements would require knowledge of different gas component concentrations, e.g., through accurate gas analysis instrumentation. For this reason, no empirical model for the Henry constant of  $\text{CO}_2$  in aqueous  $\text{K}_2\text{CO}_3$  was developed and literature models [142, 143] were employed in later analysis.

#### 4.2.3. Liquid-side mass transfer coefficient

The liquid-side mass transfer coefficient  $k_L$  was estimated from absorption experiments in water. Fig. 4.4 shows  $k_L$  as a function of temperature at a



**Figure 4.3:** Asymptotic pressure  $p_\infty$  as a function of solvent loading  $\theta$  for unpromoted  $\text{K}_2\text{CO}_3$  at 70 °C. Filled symbols: this work, 25 wt%  $\text{K}_2\text{CO}_3$  ( $C_K = 4.4$  M). Open symbols: Tosh et al. [97], 20 and 30 wt%  $\text{K}_2\text{CO}_3$  ( $C_K = 3.4$  and 5.6 M). Comparison reported in Supplementary Information of **Paper IV**.

constant stirring rate (500 rpm). The inset shows the corresponding overall mass transfer coefficient  $K_{g,w}$ , which fluctuates around a constant value, indicating weak temperature dependence. The observed temperature dependence of  $k_L$  therefore arises primarily from its derivation via eq. (A.6), in which Henry’s constant (defined in eq. (A.3)) decreases strongly with temperature.

The line represents a Sherwood ( $Sh$ ) correlation of the form  $Sh = aRe^bSc^c$ , where the exponents for the Reynolds ( $Re$ ) and Schmidt ( $Sc$ ) numbers were taken from Hikita et al. [144] (see Notations for the definitions of  $Re$ ,  $Sc$ , and  $Sh$ ). The prefactor was fitted to the measured  $k_L$  values and is approximately a factor of five lower than that reported by Hikita et al. [144]. Despite this difference, the trends governed by the  $Re$  and  $Sc$  exponents are in close agreement, which is notable given differences in reactor size and aspect ratios, higher temperatures and stirring rates, and the absence of gas-stirring in this work compared to Hikita et al. [144].

Fig. 4.5 shows  $k_L$  as a function of liquid stirring rate at a constant temperature (50 °C). The inset shows the corresponding  $K_{g,w}$ , which increases significantly with stirring rate. The increase in  $k_L$  with stirring rate is well captured by the Sherwood correlation introduced previously (Fig. 4.4). Notably, the correlation was adjusted only to the temperature data shown in Fig. 4.4. The agreement seen in Fig. 4.5 thus underlines the robustness of the Sherwood correlation.

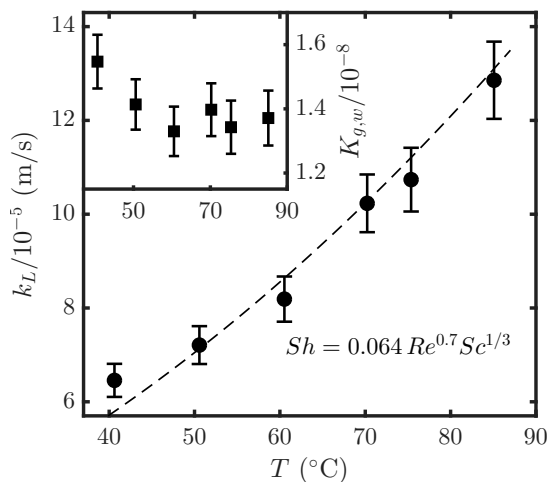


**Figure 4.4:** Liquid-side mass transfer coefficient  $k_L$  (at 500 rpm) as a function of temperature. Symbols: experiments. Line: Sherwood correlation. Inset: overall mass transfer coefficient  $K_{g,w}$  (unit: mol/m<sup>2</sup>.Pa.s) as a function of temperature (solvent: water). Error bars: 95% confidence interval from parameter fitting and error propagation. Adapted from **Paper II**.

### 4.3. Absorption into unpromoted $K_2CO_3$

**Absorption rate.** Fig. 4.6.(a) shows the overall mass transfer coefficient  $K_g$  as a function of solvent loading  $\theta$  for 25 wt% aqueous  $K_2CO_3$ . The vertical error bars represent the uncertainty from the fitting procedure (95% confidence interval). The horizontal error bars indicate uncertainty from titration and mass balances over the system.

The close values between repeated experiments (shown as separate data points) demonstrate experimental reproducibility. The larger variation at  $\theta \approx 0$  is an exception but is expected. In this region, aqueous  $K_2CO_3$  is not buffered and small amounts of absorbed atmospheric  $CO_2$  can significantly affect the  $OH^-$  concentration (see Fig. 2.3.(a)).

The influence of the chemical reaction is evident from the increase of  $K_g$  with temperature at a given  $\theta$ . In the absence of reaction (e.g., water), the temperature dependence of  $K_g$  is very weak (Fig. 4.4). At fixed temperature,  $K_g$  decreases monotonically with increasing  $\theta$  due to the corresponding decrease in  $OH^-$  concentration. Panel (b) in Fig. 4.6 shows the apparent enhancement factor  $E_{app}$ , derived from the absorption rate into aqueous  $K_2CO_3$  ( $K_g$ ) and into water ( $K_{g,w}$ ):

$$E_{app} = \frac{K_g}{K_{g,w}} \quad (4.1)$$

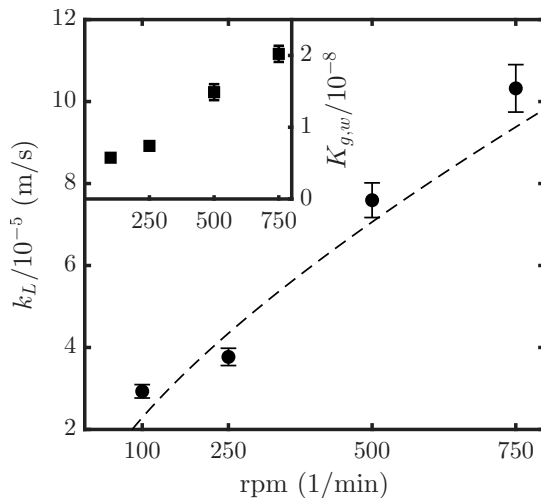


**Figure 4.5:** Liquid-side mass transfer coefficient  $k_L$  (at 50 °C) as a function of stirring rate. Symbols: experiments. Line: Sherwood correlation. Inset: overall mass transfer coefficient  $K_{g,w}$  (unit: mol/m<sup>2</sup>.Pa.s) as a function of stirring rate (solvent: water). Error bars: 95% confidence interval from parameter fitting and error propagation.

At high  $\theta$ ,  $E_{\text{app}}$  approaches unity. Under these conditions, absorption resembles that in water, although aqueous  $\text{K}_2\text{CO}_3$  remains thermodynamically favorable due to its lower equilibrium pressure.

**Rate constant.** The experimentally derived mass transfer coefficient  $K_g$  was used to determine the reaction rate constant  $k_2$ . For low solvent loadings ( $\theta < 10\%$ ),  $k_2$  was obtained by solving the reaction-diffusion problem numerically due to mild violation of the Danckwerts criterion. For higher solvent loadings, where the criterion was satisfied,  $k_2$  was determined using the analytical solutions corresponding to the pseudo-first order reaction regime.

Fig. 4.7 shows the rate constant  $k_2$  (reaction (2.III)) as a function of temperature in an Arrhenius plot for 25 wt%  $\text{K}_2\text{CO}_3$  at  $\theta = 0$ , together with data from Knuutila et al. [140] and Ye and Lu [145] at 20 and 30 wt%. The lines represent fits to the Arrhenius equation:

$$\ln k_2(\theta = 0) = \ln A - \frac{E_a}{RT} \quad (4.2)$$

where  $A$  is the pre-exponential factor and  $E_a$  is the activation energy. The present measurements lie closest to those of Knuutila et al. [140] at 20 wt%, which are consistently higher than those of Ye and Lu [145], although the activation energy obtained here is closer to the latter.

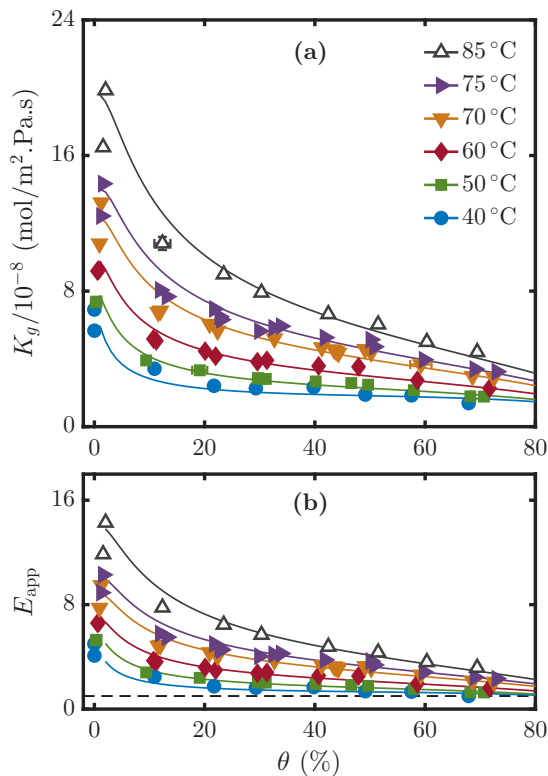


**Figure 4.6:** (a) Overall mass transfer coefficient  $K_g$  as a function of solvent loading  $\theta$  for unpromoted  $\text{K}_2\text{CO}_3$  (25 wt%). Symbols: experiments. Lines: recalculated  $K_g$  from ion-contribution model (eq. (4.7)). Error bars: (vertical) 95% confidence interval from parameter fitting; (horizontal) uncertainty in titration and setup mass balances. (b) Apparent enhancement factor as a function of solvent loading  $\theta$ . Dashed line:  $E_{\text{app}} = 1$ . Adapted from **Paper II**.

Notably, kinetic comparison of unpromoted  $\text{K}_2\text{CO}_3$  at  $\theta = 0$  is inherently challenging. The  $\text{OH}^-$  concentration is highly sensitive to small amounts of absorbed  $\text{CO}_2$ , and the pseudo-first order reaction regime is most easily violated at  $\theta = 0$ . This point was nevertheless selected due to the scarcity of kinetic data at higher  $\theta$ . Considering differences in experimental setups and data processing methods, the observed difference between  $k_2$  from this work and those reported in the literature is acceptable.

Fig. 4.8 shows the logarithm of the rate constant  $k_2$  (derived from the data in Fig. 4.6) as a function of solvent loading  $\theta$ . At fixed temperature and potassium concentration  $C_K$ , the rate constant  $k_2$  increases with  $\theta$ . This increasing trend in  $k_2$  has been indicated in the literature, albeit with more

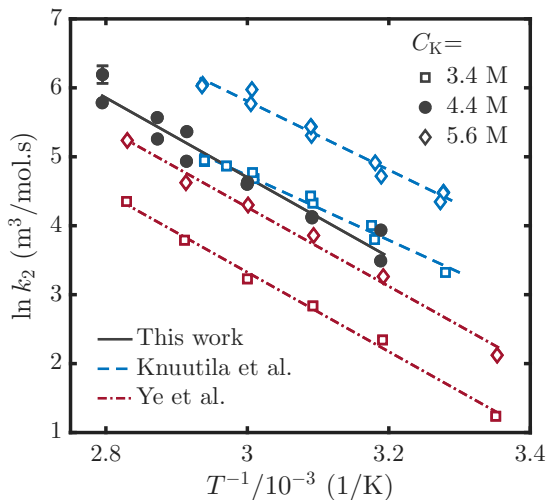


**Figure 4.7:** Arrhenius plots of rate constant  $k_2$  for reaction (2.III) zero-loading ( $\theta = 0$ ). Filled symbols: this work, 25 wt%  $\text{K}_2\text{CO}_3$  ( $C_K = 4.4$  M). Open symbols: data of Knuutila et al. [140] and Ye and Lu [145], 20 and 30 wt%  $\text{K}_2\text{CO}_3$  ( $C_K = 3.4$  and 5.6 M). Lines: fits to Arrhenius equation (eq. (4.2)). Adapted from **Paper II**.

limited datasets [145–147]. The variation in  $k_2$  arise from solution non-idealities [148, 149] and are assigned to the changes in the solvent composition.

The effects of solvent composition on the rate constant  $k_2$  were further explored by absorption experiments in 2.5–25 wt%  $\text{K}_2\text{CO}_3$  at fixed temperature (27 °C) and solvent loading ( $\theta = 20\%$ ). Fig. 4.9 shows the logarithm of the rate constant  $k_2$  as a function of the potassium concentration  $C_K$  for these experiments. The observed increase in  $k_2$  with  $C_K$  is consistent with previous literature on the reaction between  $\text{CO}_2$  and  $\text{OH}^-$  in both hydroxide and carbonate solutions [140, 145, 150–152].

**Ion-contribution model.** To describe the trends in  $k_2$ , an ion-contribution model accounting for the effects of solution non-idealities was developed. A similar framework was applied in **Paper II** for the data shown in Fig. 4.8. Here, the model is re-derived to also account for variations in potassium concentration. The ion-contribution model, originally proposed by Pohorecki and Moniuk [153], reads as:

$$\ln k_2 = \ln k_2^{(\infty)} + \sum_A \frac{1}{2} z_A^2 b_A [A] \quad (4.3)$$

where  $k_2^{(\infty)}$  is the rate constant at infinite dilution,  $z_A$  is the charge of species  $A$ , and  $b_A$  is an ion-specific coefficient. Eq. (4.3) reduces to a form equivalent to

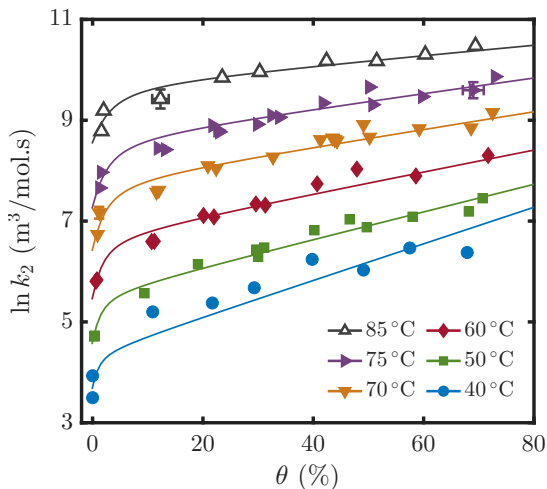


**Figure 4.8:** Logarithm of rate constant  $k_2$  for reaction (2.III) as a function of solvent loading  $\theta$ . Symbols: experiments. Lines: ion-contribution model (eq. (4.7)). Error bars: (vertical) error propagation from data processing; (horizontal) uncertainty in titration and setup mass balances. Data for different temperatures are incrementally shifted upwards by factor 0.6 to avoid congestion. Adapted from **Paper II**.

the model of Pinsent et al. [150], if  $b_A$  is assumed species independent ( $b_A = b$ ):

$$\ln k_2 = \ln k_2^{(\infty)} + b \underbrace{\sum_A \frac{1}{2} z_A^2 [A]}_I \quad (4.4)$$

where  $I$  is the ionic strength. A mechanistic interpretation of eq. (4.4) can be obtained from the Debye-McAulay framework for salting-out of non-electrolytes in electrolyte solutions, which predicts an exponential dependence of  $CO_2$  activity on ionic strength near infinite dilution [151, 154].

In the present implementation, ion-contributions from  $K^+$ ,  $CO_3^{2-}$ ,  $HCO_3^-$ , and  $OH^-$  are included, while  $H^+$  is neglected due to its low concentration. For the  $\theta$  range considered in this work, the hydroxide concentration reads as:

$$[OH^-] = -\frac{1}{2} C_K \theta - \frac{1}{2} \frac{K_w}{K_2} + \frac{1}{2} \sqrt{(C_K \theta)^2 + 2 C_K \frac{K_w}{K_2} + \left(\frac{K_w}{K_2}\right)^2} \quad (4.5)$$

where the equilibrium constants  $K_2$  and  $K_w$  (defined in section 2.3) were obtained from Imle et al. [104]. Since potassium does not participate in any reaction,  $[K^+] = C_K$ . The concentrations of  $CO_3^{2-}$  and  $HCO_3^-$  are linearly related to the potassium concentration and solvent loading through the stoichiometry

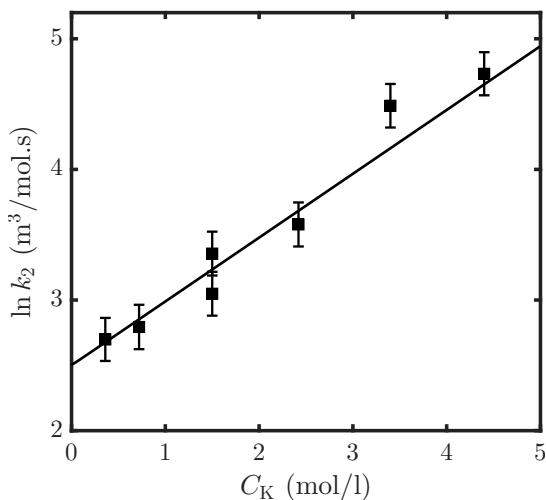


**Figure 4.9:** Logarithm of rate constant  $k_2$  for reaction (2.III) as a function of potassium concentration  $C_K$  at 27 °C and solvent loading  $\theta = 20\%$ . Symbols: experiments. Line: ion-contribution model (eq. (4.7)). Error bars: (vertical) error propagation from data processing.

of reaction (2.V):

$$[\text{CO}_3^{2-}] = \frac{1}{2}C_K(1 - \theta), \quad [\text{HCO}_3^-] = C_K\theta \quad (4.6)$$

Substituting these relations into eq. (4.3) yields:

$$\ln k_2 = \ln k_2^{(\infty)} + \beta_0 C_K + \beta_1 C_K \theta + \beta_2 [\text{OH}^-] \quad (4.7)$$

where  $\beta_0$ ,  $\beta_1$ , and  $\beta_2$  are lumped coefficients for the combined ion-contributions to  $k_2$ :

$$\beta_0 = \hat{b}_{K^+} + \frac{1}{2}\hat{b}_{\text{CO}_3^{2-}}, \quad \beta_1 = \hat{b}_{\text{HCO}_3^-} - \frac{1}{2}\hat{b}_{\text{CO}_3^{2-}}, \quad \beta_2 = \hat{b}_{\text{OH}^-} \quad (4.8)$$

where  $\hat{b}_A = \frac{1}{2}z_A^2 b_A$ . Eq. (4.7) was fitted to the entire dataset shown in Figs. 4.8 and 4.9. Since variations in  $C_K$  were conducted at a single temperature,  $\beta_0$  was treated independent of temperature, while the coefficients  $\beta_1$  and  $\beta_2$  were expressed as polynomial functions of temperature. The infinite dilution rate constant  $k_2^{(\infty)}$  was described using Arrhenius equation (eq. (4.2)), with the Arrhenius pre-factor as a fitting parameter. The activation energy  $E_a$  was fixed at the value determined for 25 wt% at zero loading, as it has been shown to be independent of potassium concentration [115, 140, 145].

The temperature-dependent polynomials and Arrhenius parameters are reported in Tab. 4.1. The coefficient  $\beta_2$  is only a weak function of temperature, while  $\beta_1$  decreases by a factor 2–3 within the range 40–85 °C. The lines in

Fig. 4.8 and 4.9 represent  $k_2$  recalculated using eq. (4.7). The ion-contribution model was subsequently used to recalculate the overall mass transfer coefficient  $K_g$  (lines in Fig. 4.6). The model reproduces both the magnitude and the trends across different temperatures, solvent loadings, and potassium concentrations. At constant solvent loading, where variations in  $\text{OH}^-$  are negligible,  $k_2$  increases exponentially with potassium concentration due to the positive  $\beta_0$  (Fig. 4.9). The increase in  $k_2$  at low solvent loadings ( $\theta = 0\text{--}10\%$ ) is governed by the negative  $\beta_2$  term combined with the rapid decrease in  $\text{OH}^-$  concentration, while the increase in  $k_2$  at  $\theta > 10\%$  is governed by the positive  $\beta_1$  term (Fig. 4.8).

**Table 4.1:** Arrhenius parameters and polynomial functions for  $\beta$  coefficients in eq. (4.7) for aqueous  $\text{K}_2\text{CO}_3$ . Values in parenthesis indicate 95% confidence interval from optimization.  $\ln k_2^{(\infty)} = \ln A^{(\infty)} - \frac{E_a}{RT}$ .  $\beta_i[\text{m}^3/\text{mol}] = a_0 + a_1T + a_2T^2 + a_3/T$ .

	$\ln A^{(\infty)} (\text{m}^3/\text{mol.s}) = 21.7(\pm 0.2)$		$E_a = 48.0(\pm 7.9) \text{ kJ/mol}$		
	$a_0$	$a_1$	$a_2$	$a_3$	
$\beta_0$	$2.390 \times 10^{-4}$	-	-	-	
$\beta_1$	$-6.840 \times 10^{-1}$	$2.004 \times 10^{-3}$	$7.827 \times 10^1$	$-1.965 \times 10^{-6}$	
$\beta_2$	$1.183 \times 10^1$	$-7.359 \times 10^{-3}$	-	$1.123 \times 10^{-5}$	

#### 4.4. Rate promoter screening

Fig. 4.10.(a) shows the overall mass transfer coefficient  $K_g$  as a function of solvent loading  $\theta$  for blends of 25 wt%  $\text{K}_2\text{CO}_3$  and different rate promoters at 70 °C. The rate promoter concentration (3 wt%) was selected based on typical values reported in the literature [72, 116, 118, 130]. For boric acid, a higher concentration (6 wt%) was used due to the mild effect of this rate promoter. For the acidic rate promoters  $\text{V}_2\text{O}_5$ ,  $\text{B}(\text{OH})_3$ , and glycine, the pH was adjusted by adding KOH, while maintaining a constant potassium concentration ( $C_K = 4.4 \text{ M}$ ). Because such blends contain less carbon to potassium, the solvent loading, by definition (eq. (2.1)), takes negative values ( $\theta < 0$ ).

In all cases,  $K_g$  decreases with increasing solvent loading. Among the tested promoters, piperazine (Pz) exhibits the largest rate enhancement over the entire range  $\theta > 0$ . This is illustrated in Fig. 4.10.(b) in terms of the apparent promotion factor, defined as:

$$P_{\text{app}} = \frac{K_g}{K_{g,0}} \quad (4.9)$$

where  $K_{g,0}$  refers to the overall mass transfer coefficient for the unpromoted solvent at the same solvent loading. A promotion factor  $P_{\text{app}} \approx 10$  at low  $\theta$  is consistent with values reported by Cullinane and Rochelle [72].

The rate enhancement provided by  $V_2O_5$ , MEA, and glycine is more modest than that of Pz but remains significant, with  $P_{app}$  generally exceeding two. At  $\theta > 25\%$ , MEA and  $V_2O_5$  exhibit similar  $K_g$ , followed by glycine at somewhat lower values. At low  $\theta$ , both MEA and glycine are significantly more effective than  $V_2O_5$ , but their performance declines rapidly with increasing  $CO_2$  uptake.

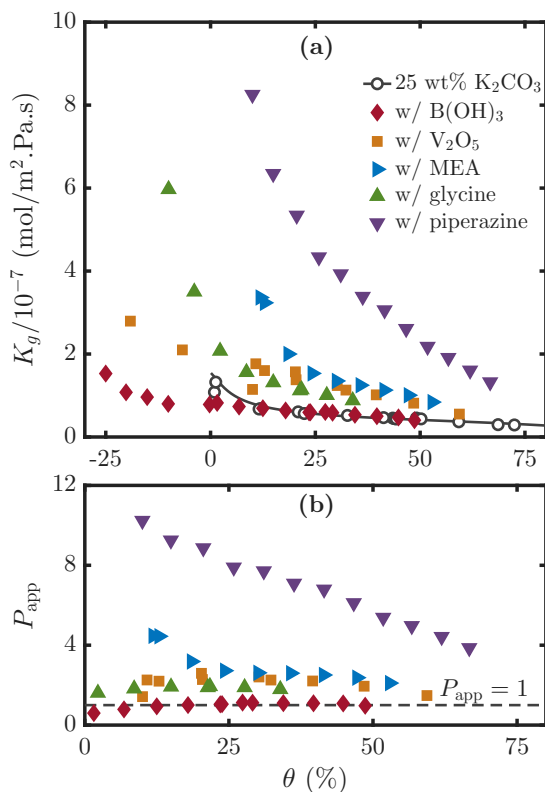
The addition of acidic compounds ( $V_2O_5$ ,  $B(OH)_3$ , and glycine) to aqueous  $K_2CO_3$  at constant  $\theta$  lowers the pH. This reduces the contribution of the hydrolysis reaction between  $CO_2$  and  $OH^-$  (reaction (2.III)) to  $CO_2$  consumption and, consequently, the absorption rate. For  $V_2O_5$  and glycine, the catalytic effect is strong enough that absorption remains faster despite the decrease in pH. In contrast, the near unity promotion factor observed for  $B(OH)_3$  indicates that its promoting effect is just sufficient to compensate for the decrease in pH.

Fig. 4.11 shows  $K_g$  for 25 wt%  $K_2CO_3$  in the presence of boric acid, vanadium pentoxide, or mixtures thereof, similar to Catacarb-type solvent blends [29]. In these experiments, high injection pressures ( $\approx 400$  kPa) were used, leading to an increase in solvent loading by  $\approx 10\%$  during each experiment. The  $K_g$  values therefore represent averages and their lower values compared to those reported in Fig. 4.10 are due to the lower pH. Increasing  $B(OH)_3$  concentration in the presence of  $V_2O_5$  suppresses the positive effect of vanadium. This is attributed to further pH reduction and a corresponding decrease in the concentration of active vanadium species, indicating no apparent synergy between  $V_2O_5$  and  $B(OH)_3$  in terms of reaction rates.

While piperazine provides the highest rate enhancement, the general behavior of amines is well understood and can be described with accurate kinetic and speciation models [72, 111, 155, 156]. In contrast, the behavior of  $V_2O_5$  and  $B(OH)_3$  remains less understood, and existing models fail to adequately capture the observed trends [130, 136]. Use of these rate promoters can be motivated by their non-volatility and their oxidation and thermal stability compared to amines, amino acids, and enzymes. The following sections therefore focus on these rate promoters to determine their mechanistic roles and kinetic characteristics in  $CO_2$  absorption.

#### 4.5. Absorption in $V_2O_5$ -promoted solvent

**Absorption rate.** Fig. 4.12.(a) shows the overall mass transfer coefficient  $K_g$  as a function of  $V_2O_5$  concentration (up to 6 wt%) in 25 wt%  $K_2CO_3$  at  $\theta = 10\%$ , while Fig. 4.12.(b) shows the corresponding promotion factor  $P_{app}$ . The  $K_g$  increases with increasing  $V_2O_5$  concentration up to  $\approx 0.2$  M (3 wt%), beyond which it plateaus and slightly decreases. At temperatures relevant to HPC operation ( $> 70$  °C), the promotion factor remains slightly above two, but reaches up to three at lower temperatures, suggesting a lower activation energy than that of reaction (2.III).



**Figure 4.10:** (a) Overall mass transfer coefficient  $K_g$  as a function of solvent loading  $\theta$  for aqueous  $K_2CO_3$  (25 wt%) in presence of various rate promoters ( $B(OH)_3$  at 6 wt%; others at 3 wt%) at 70 °C. Symbols: experiments. Line: recalculated  $K_g$  for unpromoted  $K_2CO_3$  from ion-contribution model (4.7). (b) Apparent promotion factor  $P_{app}$  as a function of solvent loading.

Fig. 4.13.(a) shows  $K_g$  as a function of solvent loading  $\theta$  at 3 wt%  $V_2O_5$ , while Fig. 4.13.(b) shows the corresponding promotion factor  $P_{app}$ . Fig. 4.13 indicates that  $V_2O_5$  remains effective within the entire range of  $\theta > 0$ . The low  $P_{app}$  at  $\theta = 0$  arises from the high  $OH^-$  concentration in the unpromoted solvent, which results in a larger  $K_{g,0}$ . The subsequent increase in  $P_{app}$  reflects the rapid decrease in  $K_{g,0}$  with  $\theta$ .

**Active species.** The active vanadate species that describes the trends in both Figs. 4.12 and 4.13 was identified as hydrogen monovanadate  $HVO_4^{2-}$ . This identification was based on comparison between trends in  $K_g$  and the concentrations of individual vanadate species (obtained from vanadium(V)

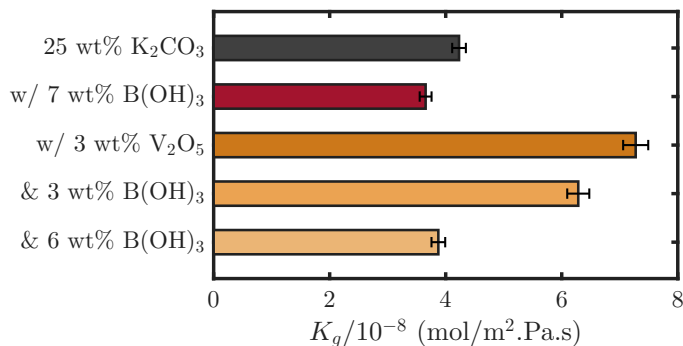


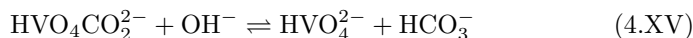
**Figure 4.11:** Overall mass transfer coefficients for 25 wt%  $\text{K}_2\text{CO}_3$  with initial solvent loading  $\theta = 0$  and 50 °C, containing boric acid, vanadium pentoxide, or mixtures thereof. Modified from **Paper I**.

equilibria reported by Imle et al. [104]). Accordingly, the plateau in  $K_g$  with increasing  $\text{V}_2\text{O}_5$  concentration and constant  $\theta$  (Fig. 4.12.(a)) occurs because the  $\text{HVO}_4^{2-}$  concentration reaches a maximum, due to polyvanadate formation and a decrease in pH. Similarly, the decrease in  $K_g$  with increasing  $\theta$  reflects reductions in  $\text{HVO}_4^{2-}$  as well as  $\text{OH}^-$  concentrations (Fig. 4.13.(a)).

The role of hydrogen monovanadate as active species in vanadium-promoted aqueous  $\text{K}_2\text{CO}_3$  can be explained through a complex-formation mechanism. Dissolved  $\text{CO}_2$  reacts with  $\text{HVO}_4^{2-}$  to form a carbonato-vanadate complex:



where  $k_v$  is the second order rate constant. The existence of carbonato-vanadate complexes has been demonstrated spectroscopically in the literature [130, 157–159]. The complex  $\text{HVO}_4\text{CO}_2^{2-}$  subsequently dissociates in the presence of  $\text{OH}^-$  to reform  $\text{HVO}_4^{2-}$  and release the carbon as  $\text{HCO}_3^-$ :



Since the reaction rate (reflected in  $K_g$ ) follows the concentration of  $\text{HVO}_4^{2-}$ , the complex formation (reaction (4.XIV)) is identified as the rate-limiting step.

**Reaction kinetics.** Based on the reaction mechanism given above,  $\text{CO}_2$  reacts in vanadium-promoted  $\text{K}_2\text{CO}_3$  via two pathways: direct hydrolysis by hydroxide and reaction with hydrogen monovanadate. The pseudo-first order rate constant  $k_1$  accounting for these two reactions reads as:

$$k_1 = k_2[\text{OH}^-] + k_v[\text{HVO}_4^{2-}] \quad (4.10)$$

To determine the rate constant  $k_v$ ,  $k_1$  was estimated from the measured  $K_g$  values and the  $k_2$  was obtained from the ion-contribution model (section 4.3).

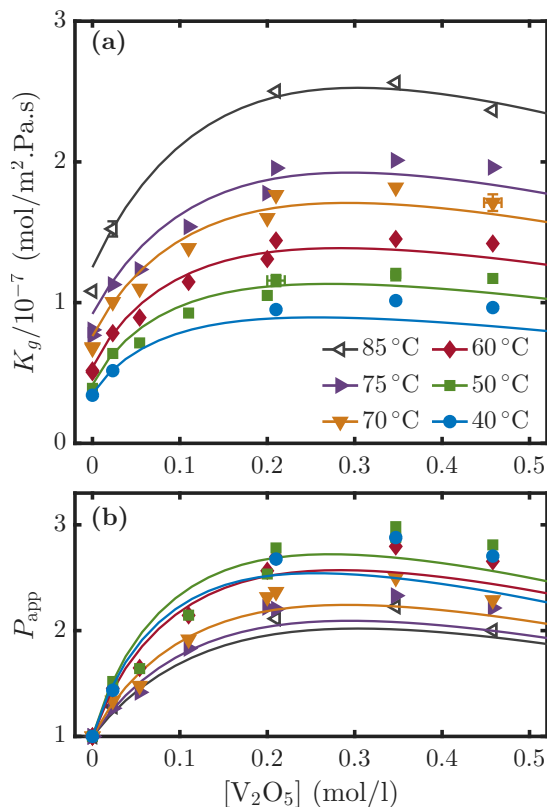


**Figure 4.12:** (a) Overall mass transfer coefficient  $K_g$  as a function of  $V_2O_5$  concentration at  $\theta = 10\%$ . Symbols: experiments. Error bars: (vertical) 95% confidence interval from parameter fitting; (horizontal) uncertainty in titration and setup mass balances. Lines: kinetic model (eq. (4.11)). (b) Apparent promotion factor as a function of solvent loading  $\theta$ . Adapted from **Paper III**.

$OH^-$  and  $HVO_4^{2-}$  concentrations were determined from the speciation model of Imle et al. [104]. Measurements violating the Danckwerts criterion were excluded from the kinetic analysis, due to the large number of species and the lack of available physical property data. The resulting  $k_v$  shows a pronounced dependence on the ionic strength of the solution, as shown in Fig. 4.14. Within the experimental range, the increase in  $k_v$  is well described by an exponential function of the form:

$$k_v = k_v^{(\infty)} \exp(\beta_v I) \quad (4.11)$$

where  $k_v^{(\infty)}$  is the rate constant at infinite dilution, following an Arrhenius-type temperature dependence, and  $\beta_v$  is a weak function of temperature (see Tab. 4.2).

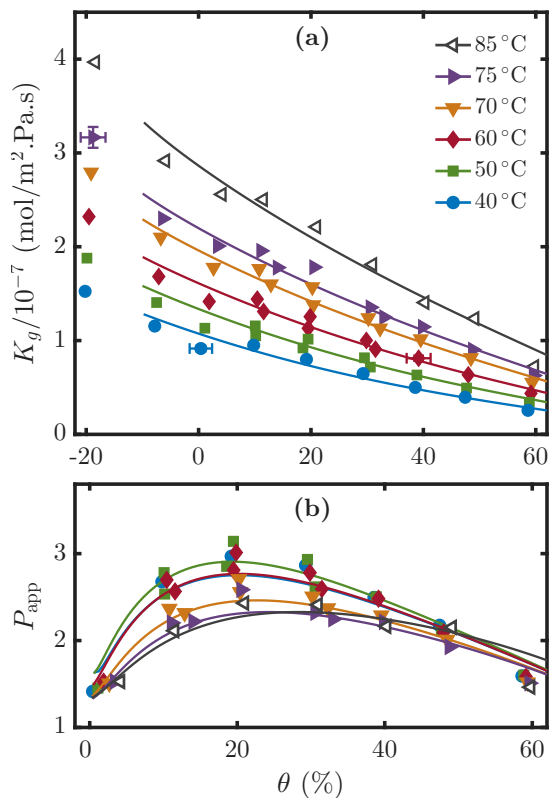


**Figure 4.13:** (a) Overall mass transfer coefficient  $K_g$  as a function of solvent loading for 0.21 M  $V_2O_5$  (3 wt%). Symbols: experiments. Error bars: (vertical) 95% confidence interval from parameter fitting; (horizontal) uncertainty in titration and setup mass balances. Lines: kinetic model (eq. (4.11)). (b) Apparent promotion factor as a function of solvent loading  $\theta$ . Adapted from **Paper III**.

The lines in Fig. 4.12 and 4.13 show the recalculated values of  $K_g$  using eq. (4.11) (data at  $\theta = -20\%$  were excluded due to a violation of the Danckwerts criterion). The close agreement between model predictions and measured  $K_g$  supports the validity of the model and indicates that fluctuations in  $k_v$  around the fitted model (Fig. 4.14) are not significant. The model predicts  $k_v$  values a factor 10 lower than  $k_2$ . However, for  $V_2O_5$  concentrations higher than 0.1 M, the concentration of  $HVO_4^{2-}$  is 2–3 orders of magnitude higher than that of  $OH^-$ . As a result, the vanadium pathway dominates the reaction with  $CO_2$  over a wide range of solvent loadings.

**Table 4.2:** Arrhenius parameters and polynomial for the coefficient  $\beta_v$  for the rate constant  $k_v$  (eq. (4.11)). Values in parenthesis indicate 95% confidence interval from optimization.  $\ln k_v^{(\infty)} = \ln A_v - E_v/RT$ . Adapted from **Paper III**.

$E_v$ (kJ/mol)	35.94(±14.41)			
$\ln A_v$ (m <sup>3</sup> /mol.s)	13.24(±6.68)			
$\beta_v$ (m <sup>3</sup> /mol) = $a_0 + a_1T + a_2/T + a_3T^2$				
	$a_0$	$a_1$	$a_2$	$a_3$
	$2.3788 \times 10^{-1}$	$-7.1978 \times 10^{-4}$	$-2.6146 \times 10^1$	$7.29 \times 10^{-7}$

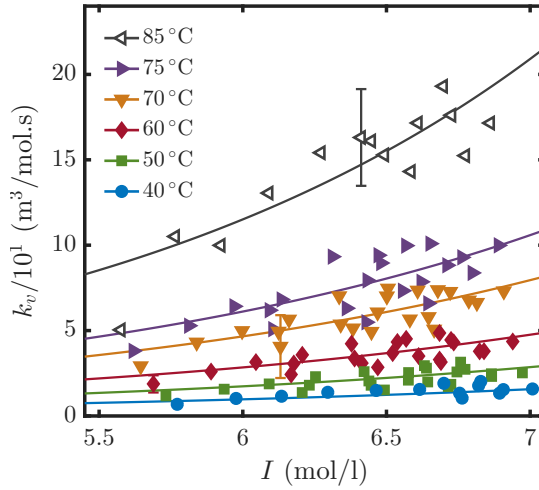


**Figure 4.14:** Rate constant  $k_v$  for reaction (4.XIV) as a function of ionic strength  $I$ . Symbols: experiments. Error bars: (vertical) uncertainty in  $k_v$  (error propagation from  $K_g$ ). Lines: kinetic model (eq. (4.11)). Adapted from **Paper III**.

## 4.6. Absorption in presence of B(OH)<sub>3</sub>

**Absorption rate.** In contrast to V<sub>2</sub>O<sub>5</sub>, boric acid shows minor effects on CO<sub>2</sub> absorption rates. However, the lowering of pH in the presence of boron at fixed  $\theta$  (Fig. 4.10) prevents a firm assessment regarding possible catalytic effects.

Fig. 4.15 shows  $K_g$  as a function of boric acid concentration  $C_B$  for 25 wt% K<sub>2</sub>CO<sub>3</sub>. The pH was fixed at 10.5 (calculated from the carbonate-borate equilibria [104]) by adjusting  $\theta$ . With an increasing  $C_B$ , the solvent loading  $\theta$  must be decreased to maintain constant pH. While the measured pH deviated

from the calculated values, the difference did not exceed 0.3 units across the range of boron concentrations.

At constant pH, where the rate of reaction (2.III) between  $\text{CO}_2$  and  $\text{OH}^-$  is expected to remain unchanged,  $K_g$  increases mildly upon addition of boron and eventually plateaus at about 3 wt%  $\text{B}(\text{OH})_3$  (0.6 M). The behavior is similar across all temperatures, suggesting that the activation energy for the  $\text{CO}_2$  reaction is independent of boron concentration. The mild increase in  $K_g$  aligns with pilot tests reporting no improvement in  $\text{CO}_2$  uptake upon addition of  $\text{B}(\text{OH})_3$  [137], as this rate enhancement is sufficiently small that it may not be observed within the experimental error of such complex pilot processes.

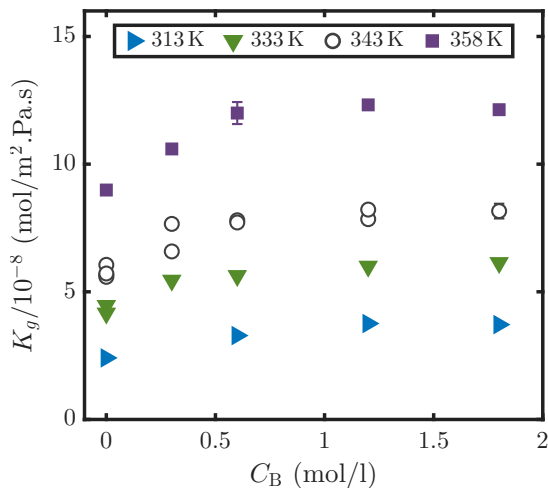


**Figure 4.15:** Overall mass transfer coefficient  $K_g$  as a function of boron concentration  $C_B$  (up to 9 wt%  $\text{B}(\text{OH})_3$ ) for 25 wt%  $\text{K}_2\text{CO}_3$  ( $C_K = 4.5$  M) at fixed pH of 10.5. Error bars: (vertical) 95% confidence interval from parameter fitting. Adapted from Paper IV.

**Borate buffering.** The primary motivation for employing boric acid appears to be to increase the  $\text{CO}_2$  absorption capacity, as suggested by Eickmeyer [29] and Field [124]. The increase in  $\text{CO}_2$  capacity arises because monoborate  $\text{B}(\text{OH})_4^-$  buffers within the operating pH range of the HPC process. The buffering capacity of a  $\text{K}_2\text{CO}_3$ - $\text{B}(\text{OH})_3$  solution can be derived from the governing equilibria as:

$$\bar{C} = \frac{1}{2}C_K \left( 1 + \frac{C_B}{C_K} \right) \quad (4.12)$$

where  $\bar{C}$  is the theoretical moles of  $\text{CO}_2$  taken up by the buffer per unit volume of solution to fully convert carbonate to bicarbonate. More comprehensive

equilibrium models, including polyborate species [104], also predict that  $\bar{C}$  increases with boron concentration, albeit at a lower rate than given by eq. (4.12).

To account for the effect of borate buffering across different compositions, the experimental data are instead analyzed in terms of carbonate conversion  $\alpha$ , defined as:

$$\alpha = \frac{[\text{CO}_3^{2-}]_{\theta=\theta_0} - [\text{CO}_3^{2-}]_{\theta>\theta_0}}{[\text{CO}_3^{2-}]_{\theta=\theta_0}} \quad (4.13)$$

where  $[\text{CO}_3^{2-}]_{\theta=\theta_0}$  and  $[\text{CO}_3^{2-}]_{\theta>\theta_0}$  are the carbonate concentrations in the non-buffered solution and the buffered solution (i.e., after CO<sub>2</sub> uptake), respectively. The solvent loading corresponding to the non-buffered solution ( $\theta_0$ ) reads as:

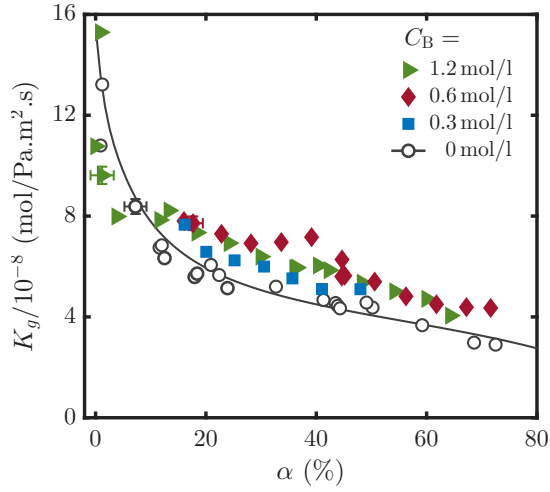
$$\theta_0 = -\frac{C_B}{C_K} \quad (4.14)$$

According to eq. (4.14),  $\theta_0$  represents a blend in which B(OH)<sub>3</sub> and KOH are added in equimolar amounts to K<sub>2</sub>CO<sub>3</sub>. At the low B-to-K ratios considered here,  $\alpha$  represents the extent to which the buffering capacity is exhausted relative to the initial state at  $\theta_0$ , where carbon is predominantly present as CO<sub>3</sub><sup>2-</sup>.

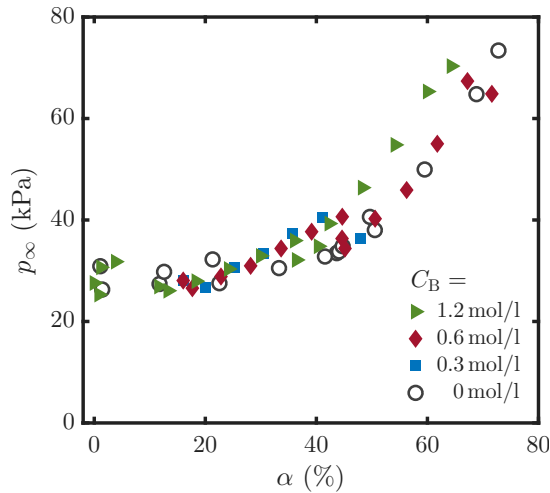
Fig. 4.16 shows the overall mass transfer coefficient  $K_g$  as a function of carbonate conversion  $\alpha$  for 25 wt% K<sub>2</sub>CO<sub>3</sub> at 70 °C and various boron concentrations. While expressing the data in terms of  $\theta$  stretches the boron data to the negative  $\theta$  region (see Fig. 4.10), expressing  $K_g$  as a function of  $\alpha$  largely collapses the data. The resulting  $K_g$  behavior and values against  $\alpha$  become nearly independent of boron concentration. Consequently,  $K_g$  predicted from the ion-contribution model for unpromoted K<sub>2</sub>CO<sub>3</sub> (line), where  $\alpha = \theta$ , adequately describes the trends in the presence of boron, albeit with a slight underestimation. This indicates that accurate speciation models are sufficient to capture the effect of boron on the absorption rate.

Fig. 4.17 shows the asymptotic pressure  $p_\infty$  established in the reactor as a function of carbonate conversion. Previous studies have shown that the addition of boric acid to aqueous K<sub>2</sub>CO<sub>3</sub> increases the equilibrium CO<sub>2</sub> pressure [131–133]. This is consistent with polyborate formation and weak acidic effects of boron, but appears counterintuitive to the notion of increased absorption capacity. Replotting the asymptotic pressure  $p_\infty$  against carbonate conversion  $\alpha$  largely resolves this deviation. The remaining deviation at  $C_B = 1.2$  M (high  $\alpha$ ) is in comparison minor and could be due to solution non-idealities.

**Reaction kinetics.** While the rate model for unpromoted K<sub>2</sub>CO<sub>3</sub>, combined with borate speciation, predicts absorption rates reasonably well, it slightly underestimates  $K_g$  (Figs. 4.15–4.16). This deviation has been attributed in the literature to a parallel reaction between CO<sub>2</sub> and B(OH)<sub>4</sub><sup>-</sup> [135, 136, 138]. However, since B(OH)<sub>4</sub><sup>-</sup> increases monotonically with  $C_B$ , such a mechanism would imply a stronger and more systematic dependence of  $K_g$  on boron concentration than is observed.



**Figure 4.16:** Overall mass transfer coefficient  $K_g$  as a function of carbonate conversion  $\alpha$  for 25 wt%  $\text{K}_2\text{CO}_3$  ( $C_K = 4.5$  M) at 70 °C. Symbols: experiments. Line: recalculated  $K_g$  from ion-contribution model for unpromoted solvent (eq. (4.7)). Error bars: (vertical) 95% confidence interval from parameter fitting; (horizontal) uncertainty in solvent loading from titration and setup mass balances. Adapted from **Paper IV**.



**Figure 4.17:** Asymptotic pressure  $p_\infty$  as a function of carbonate conversion  $\alpha$  for 25 wt%  $\text{K}_2\text{CO}_3$  ( $C_K = 4.5$  M) at 70 °C. Adapted from **Paper IV**.

Instead, the data suggest that borates influence the hydrolysis reaction between CO<sub>2</sub> and OH<sup>-</sup> (reaction (2.III)) indirectly through the rate constant  $k_2$ . In this interpretation, absorption proceeds via a single reaction, i.e., CO<sub>2</sub> reacting with OH<sup>-</sup> with  $r_f = k_2[\text{CO}_2][\text{OH}^-]$ , where the presence of borate species affects the value of  $k_2$ . Fig. 4.18 shows the logarithm of  $k_2$  as a function of carbonate conversion  $\alpha$ , with  $k_2$  derived from measured  $K_g$  under this single-reaction assumption. The trends mirror those of unpromoted K<sub>2</sub>CO<sub>3</sub>, with a rapid increase at low  $\alpha$  followed by a slower exponential rise. The primary difference is an upward shift with increasing boron concentration.

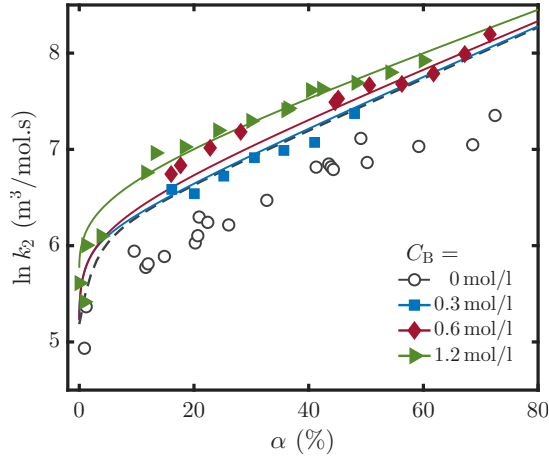


**Figure 4.18:** Logarithm of rate constant  $k_2$  for reaction (2.III) between CO<sub>2</sub> and OH<sup>-</sup> as a function of carbonate conversion  $\alpha$ . Symbols: experiments. Lines: kinetic model (eq. (4.15); solid: with boron; dashed: without boron). Adapted from **Paper IV**.

Accordingly, the effects of boron on the reaction rate of CO<sub>2</sub> are described within the framework of the ion-contribution model, with an additional term to account for borate species. The rate constant  $k_2$  relative to its value at a reference state (unpromoted solvent at the same  $C_K$  and  $\alpha = \theta = 0$ ), can be expressed as:

$$\ln k_2 - \ln k_2(\alpha = 0) = \hat{b}_{\text{CO}_3^-}([\text{CO}_3^{2-}] - [\text{CO}_3^{2-}]_0) + \hat{b}_{\text{HCO}_3^-}[\text{HCO}_3^-] + \hat{b}_{\text{OH}^-}([\text{OH}^-] - [\text{OH}^-]_0) + \hat{b}_B[\text{B(OH)}_4^-] \quad (4.15)$$

where  $k_2(\alpha = 0)$  follows the Arrhenius equation and corresponds to non-buffered K<sub>2</sub>CO<sub>3</sub> in the absence of boron (eq. (4.2)). Tab. 4.3 lists the parameter values obtained by fitting eq. (4.15) to the experimentally determined  $k_2$  values. The lines in Fig. 4.18 show the corresponding model predictions. The model shows close agreement with the data, with the boron contribution ( $\hat{b}_B$ ) capturing the

**Table 4.3:** Coefficients  $\hat{b}$  [ $\text{m}^3/\text{mol}$ ] for 25 wt%  $\text{K}_2\text{CO}_3$  in the presence of boric acid at 70 °C (eq. (4.15)). Adapted from **Paper IV**.

$\hat{b}_{\text{CO}_3^{2-}}$	$\hat{b}_{\text{HCO}_3^-}$	$\hat{b}_{\text{OH}^-}$	$\hat{b}_{\text{B}}$
$-1.82 \times 10^{-3}$	$-3.24 \times 10^{-4}$	$-1.45 \times 10^{-2}$	$-1.24 \times 10^{-3}$

upward shift with increasing boron concentration. The dashed line shows the model prediction for unpromoted  $\text{K}_2\text{CO}_3$ . Its inability to reproduce the boron-free data (not included in the fitting) arises primarily from an overestimation of  $\hat{b}_{\text{OH}^-}$  (by  $\approx 40\%$ ), which leads to an exaggerated increase in  $k_2$  at low  $\alpha$  (0–10%).

# Chapter 5

## Conclusions

### 5.1. Summary and conclusions

This thesis presents CO<sub>2</sub> absorption rate data in aqueous potassium carbonate (K<sub>2</sub>CO<sub>3</sub>) in the presence of inorganic rate promoters vanadium pentoxide (V<sub>2</sub>O<sub>5</sub>) and boric acid (B(OH)<sub>3</sub>). Given their established use in conventional gas cleaning, these rate promoters are expected to feature in the first-generation of hot potassium carbonate (HPC)-based post-combustion carbon capture. The thesis addresses the mechanisms underlying the rate enhancement by V<sub>2</sub>O<sub>5</sub> and B(OH)<sub>3</sub>, which have been unclear in current literature.

To determine the roles of V<sub>2</sub>O<sub>5</sub> and B(OH)<sub>3</sub>, absorption experiments were conducted in a stirred batch reactor across a wide range of temperatures, solvent loadings, and promoter concentrations, reflecting the operating conditions of the HPC process. Baseline measurements were performed with unpromoted aqueous K<sub>2</sub>CO<sub>3</sub> and the performances of V<sub>2</sub>O<sub>5</sub> and B(OH)<sub>3</sub> were compared to other established rate promoters, namely, monoethanolamine (MEA), piperazine (Pz), and glycine. The experimental observations were supported with mechanistic explanations and kinetic models capable of describing trends in the data, through resolving the reaction-diffusion phenomena at the gas-liquid interface and the equilibrium of the chemical species.

This thesis summarizes results from four appended papers:

**Paper I** presents a screening of rate promoters under fixed conditions. The investigation was motivated by a lack of comparative studies of amine (MEA, Pz) and inorganic rate promoters (B(OH)<sub>3</sub>, V<sub>2</sub>O<sub>5</sub>). The experiments showed the fastest absorption rates in the presence of MEA and Pz but could not distinguish their reaction rates with CO<sub>2</sub>, due to high injection pressures causing significant depletion of non-CO<sub>2</sub> species at the gas-liquid interface. Nevertheless, **Paper I** (*i*) confirms the responsiveness of the experimental setup to different rate promoters; (*ii*) qualitatively demonstrates the influence of combined V<sub>2</sub>O<sub>5</sub> and B(OH)<sub>3</sub>

blends and highlights the importance of pH control; and *(iii)* identifies limitations of the setup under extreme conditions. In this thesis, complementary experiments with MEA, piperazine, and glycine promoters are provided under controlled conditions across a wider range of solvent loadings (Fig. 4.10).

**Paper II** reports experiments on unpromoted  $\text{K}_2\text{CO}_3$  (25 wt%) across a solvent loading range of 0–70% and a temperature range of 40–85 °C. The study addresses gaps in absorption rate data at high loadings where existing kinetic models are insufficient. **Paper II** *(i)* determines the liquid-side mass transfer coefficient ( $k_L$ ) of the reactor through absorption experiments in water; *(ii)* validates the setup by comparing the measured rate constant  $k_2$  (reaction (2.III)) at zero loading with literature; *(iii)* demonstrates the strong dependence of  $k_2$  on ionic composition and shows that this dependence cannot be eliminated by diffusion considerations; and *(iv)* proposes an ion-contribution model that closely captures the observed trends. This thesis further extends the analysis with experiments examining the effect of potassium concentration on  $k_2$  (Fig. 4.9).

**Paper III** investigates vanadium-promoted  $\text{K}_2\text{CO}_3$  (25 wt%) across  $\text{V}_2\text{O}_5$  concentrations up to 6 wt%, solvent loadings -20 to 60%, and temperatures 40–85 °C. The study was motivated by conflicting accounts on the mechanism of  $\text{CO}_2$  reaction in the vanadium-promoted solvent and the limited absorption data. **Paper III** *(i)* quantifies the effects of  $\text{V}_2\text{O}_5$  on the  $\text{CO}_2$  absorption rate, identifying optimal promoter concentration and solvent loading ranges; *(ii)* identifies hydrogen monovanadate  $\text{HVO}_4^{2-}$  as the active species catalyzing  $\text{CO}_2$  hydrolysis via a complex formation-dissociation mechanism. This conclusion partially contradicts previous literature [129, 130], but is supported by a larger dataset and consistency with comprehensive speciation models [104, 158, 160]. Furthermore, the paper *(iii)* demonstrates that the rate constant  $k_v$  for the reaction between  $\text{CO}_2$  and  $\text{HVO}_4^{2-}$  (reaction (4.XIV)) depends on the solvent composition, attributed to ionic strength effects.

**Paper IV** studies boron-promoted  $\text{K}_2\text{CO}_3$  (25 wt%) across  $\text{B}(\text{OH})_3$  concentrations up to 9 wt% and solvent loadings -20 to 70%. The study rationalizes the use of boric acid in industrial blends given that previous literature report only a limited effect on  $\text{CO}_2$  reaction rates. **Paper IV** *(i)* demonstrates, through theoretical calculations and titration experiments, that boric acid increases the  $\text{CO}_2$  absorption capacity by buffering at the operating pH; *(ii)* demonstrates that anomalies in absorption rate and vapor-liquid equilibrium data due to the addition of  $\text{B}(\text{OH})_3$  are largely resolved when expressed in terms of buffering capacity; and *(iii)* demonstrates that the mild positive effect of boron on  $\text{CO}_2$  reaction rate can be described by including an additional term in the ion-contribution model.

## 5.2. Sustainability contribution

Sustainability forms a major aspect of education and research at KTH. As part of these efforts, PhD theses include a reflection on the contribution of the presented research to sustainable development goals (SDGs). Given the niche scope of this work, addressing knowledge gaps on the chemistry of an existing absorption technology, it does not directly contribute to any SDG. Nevertheless, the work supports the SDGs indirectly through improved understanding of carbon capture processes, providing the tools for decision-makers to assess specific options for carbon capture. With these considerations, this section reflects instead on the broader aspects of CCS implementation.

CCS deployment directly contributes to goal (13) **climate action** by emissions reduction or CO<sub>2</sub> removal. This is closely connected to goals (14) **life below water** and (15) **life on land**, by slowing or preventing ocean acidification and rise in sea levels. Considering the impact of CO<sub>2</sub> emissions on global warming and its small utilization potential, CO<sub>2</sub> can be considered as a waste stream. From this perspective, CCS also contributes to goal (12) **responsible consumption and production**.

CCS deployment may also conflict with certain SDGs. It increases the cost of energy production from carbon-based sources, which may translate into higher energy prices. There are also very valid concerns that CCS enables continued reliance on fossil fuels. Consequently, even though CCS could lead to a cleaner energy product, it may conflict with goal (7) **clean and affordable energy**. CCS currently relies heavily on public funding due to high capital costs and the limited economic value of captured CO<sub>2</sub>, which may place a financial burden on taxpayers. Therefore, it may also conflict with goal (8) **decent work and economic growth**.

Some critiques of BECCS implementation point out to potential competition between food and energy crops production, thus contributing against goal (2) **zero hunger**. While this is a valid concern, it would require substantial replacement of existing infrastructure with bio-energy which appears unlikely given the availability of alternative low-carbon energy sources.

## 5.3. Future work

Despite the contributions of this thesis in the form of comprehensive absorption rate data and kinetic models for first-generation inorganic rate promoters for aqueous K<sub>2</sub>CO<sub>3</sub>, further research is required to address remaining knowledge gaps.

- Desorption of CO<sub>2</sub> from loaded aqueous K<sub>2</sub>CO<sub>3</sub> is seldom studied [161]. The backward reaction rate constants relevant for desorption are typically estimated from the forward rate constants (such as those determined here), but this requires extrapolation to higher temperatures ( $\geq 100$  °C). Desorption

studies are further necessary to confirm whether substances which catalyze CO<sub>2</sub> absorption (e.g., V<sub>2</sub>O<sub>5</sub>, carbonic anhydrase, piperazine) can also act as rate promoters for desorption or not. The screening studies by Li et al. [118] indicates this to be the case for amino acid rate promoters. Eickmeyer [29] also claims that addition of the Catacarb rate promoters (vanadium pentoxide and boric acid) increased capture efficiency without substantially changing reboiler demand, supporting the notion that the desorption rate also increases. Nevertheless, limited quantitative studies on the effects of rate promoters on CO<sub>2</sub> desorption exist.

A primary challenge of measuring desorption rates is the control of the gas-liquid interface area. A continuous configuration (e.g., wetted-wall column) appears better suited for such experiments given that the gas composition can be adjusted such that CO<sub>2</sub> desorbs from the liquid. A stirred batch reactor such as that of this work could be used by removing equilibrated gas from the reactor, leading to release of CO<sub>2</sub> from the solvent until re-equilibration. Such rate measurements, however, rely on the dynamics of both CO<sub>2</sub> desorption and water evaporation, and also necessitate presence of a neutral gas component (e.g., nitrogen, helium) to prevent boiling of the solvent, and thus keeping the interface area flat.

- The rate promoters studied in this work likely form the first-generation of HPC-based carbon capture, due to their development in conventional gas cleaning processes. One could fairly point to an array of issues such as toxicity, comparably slow rates (with the exception of piperazine) to amine-based solvents, or even the limited number of available options. Further research could therefore aim at developing novel rate promoters. Such substances could include stable carbonic anhydrase variants or enzyme mimics (e.g., Zn(II)-cyclen [123]). Recent literature indicate also that substances synthesized from transition metal oxides (e.g., niobium, titanium) could form reaction products with CO<sub>2</sub> [162, 163], and thus could potentially serve as rate promoters. Supporting experiments conducted in this work using Zn(II)-cyclen [164] or niobium polyoxometalate [163] were inconclusive, highlighting either their limited effectiveness or the difficulty in reproducible synthesis.
- Few studies investigate the impact of rate promoters on the absorption process, by simulation or pilot tests. Simulation studies are crucial for transferring the knowledge developed in works such as this one, to the larger scale, demonstrating their potential effects on equipment sizing and compression duties, and determining the optimal operating conditions. Pilot studies are valuable because they can identify operational issues which could only occur upon extended use, e.g., formation of degradation products or accumulation of heat stable salts. While amines benefit from a great body of literature investigating their degradation and reclamation, there are few open literature

sources on spent inorganic blends (e.g.,  $V_2O_5$ ,  $B(OH)_3$ ). Beyond word-of-mouth evidence regarding their stability, there is limited empirical evidence on their longevity or response to gas impurities (e.g.,  $SO_x$ ,  $NO_x$ ,  $H_2S$ ).

## Appendix A

# Mass transfer across gas-liquid interface

### A.1. Two-film model

Absorption of  $\text{CO}_2$  can be represented as a sequence of transport steps.  $\text{CO}_2$  transfers from the bulk gas to the gas-liquid interface, through which it dissolves and diffuses into the liquid bulk where it reacts. These steps are schematically shown in Fig. A.1 and can be lumped into an overall mass transfer coefficient using the two-film model. The regions indicated as gas and liquid-side films represent zones where concentration gradients are significant and their depths of penetration reflects the mass transfer resistances in each phase [60].

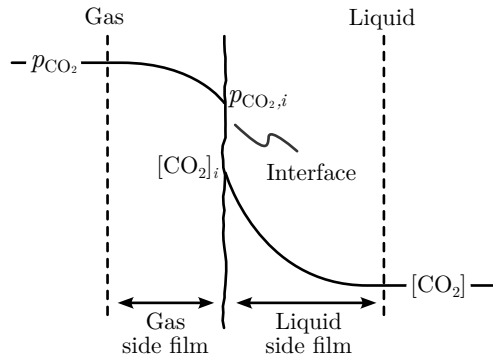


**Figure A.1:** General schematics of  $\text{CO}_2$  concentration profile from gas to liquid during absorption.

In the two-film model, CO<sub>2</sub> flux through gas and liquid is assumed proportional to the concentration (pressure for gas) difference at the boundaries of each respective phase, i.e., bulk and interface:

$$N_{\text{CO}_2} = k_g(p_{\text{CO}_2} - p_{\text{CO}_2,i}) \quad (\text{A.1})$$

$$N_{\text{CO}_2} = k_L E([\text{CO}_2]_i - [\text{CO}_2]) \quad (\text{A.2})$$

where  $p_{\text{CO}_2}$  and  $[\text{CO}_2]$  refer to CO<sub>2</sub> partial pressure in bulk gas and CO<sub>2</sub> concentration in bulk liquid, and subscripts  $i$  refers to these properties at interface.  $k_g$  and  $k_L$  are the gas-side and liquid-side mass transfer coefficients, respectively, incorporating both hydrodynamics of the gas-liquid contactor and physical properties in each phase. The enhancement factor  $E$  is defined as the ratio of absorption flux in the presence of reaction to that under purely physical absorption at the same driving force. Accordingly, for physical absorption  $E = 1$ . Determination of  $E$  requires solving the coupled reaction-diffusion problem in the liquid phase [60].

At the interface, fugacity continuity is described by Henry's law:

$$H = \frac{[\text{CO}_2]_i}{p_{\text{CO}_2,i}} = \frac{[\text{CO}_2]}{p_{\text{CO}_2}^*} \quad (\text{A.3})$$

where  $H$  is the Henry constant of CO<sub>2</sub>. Combining with eqs. (A.1)-(A.3) yields the absorption flux in terms of bulk concentrations:

$$N_{\text{CO}_2} = K_g \left( p_{\text{CO}_2} - \frac{[\text{CO}_2]}{H} \right) = K_g (p_{\text{CO}_2} - p_{\text{CO}_2}^*) \quad (\text{A.4})$$

The overall mass transfer coefficient  $K_g$  represents the resistances-in-series of gas and liquid phases, and reads as:

$$K_g = \left( \frac{1}{k_g} + \frac{1}{k_L E H} \right)^{-1} \quad (\text{A.5})$$

In the experiments of this work, the gas-side mass transfer resistance is negligible relative to liquid-side mass transfer resistance, due to a nearly pure CO<sub>2</sub> atmosphere, simplifying eq. (A.5) to:

$$K_g = k_L E H \quad (\text{A.6})$$

## A.2. Film theory

The differential mass balance for species  $A$  in the liquid phase adjacent to the interface reads as:

$$\frac{\partial c_A}{\partial t} = D_A \frac{\partial^2 c_A}{\partial x^2} + r_A \quad (\text{A.7})$$

where  $t$  is time,  $x$  is distance from the interface,  $c_A$  is the concentration of  $A$  within the film,  $D_A$  is diffusivity of  $A$  in the liquid phase, and  $r_A$  is its reaction rate. Eq. (A.7) neglects convective transport arising from liquid agitation. The convective effects are incorporated into the boundary conditions and into the

physical abstraction used to describe the mass transfer between the interface and the bulk liquid [102].

Here, this physical abstraction is represented by the film theory. In the film theory, hydrodynamic effects arising from convection are lumped into a stagnant layer at the interface, within which eq. (A.7) applies, while the bulk liquid is assumed to have a uniform concentration. The boundary conditions to eq. (A.7) for absorbing species  $A$  (representing  $\text{CO}_2$ ) and reactant  $B$  diffusing from the liquid bulk read as [102]:

$$\begin{cases} x = 0 : & c_A = [A]_i, \quad dc_B/dx = 0 \\ x = \delta : & c_A = [A], \quad c_B = [B] \end{cases} \quad (\text{A.8})$$

where  $\delta$  denotes the film thickness. Schematics of concentration profiles predicted by the film theory are depicted in Fig. A.2 for four cases. Case (a) represents physical absorption; case (b) represents the pseudo-first order reaction regime, where the concentration gradient of  $B$  within the film is negligible ( $[B]_i = [B]$ ); case (c) represents an intermediate regime with partial depletion of  $B$  at the interface; and case (d) represents the instantaneous reaction regime, in which  $A$  and  $B$  react immediately and irreversibly upon contact.

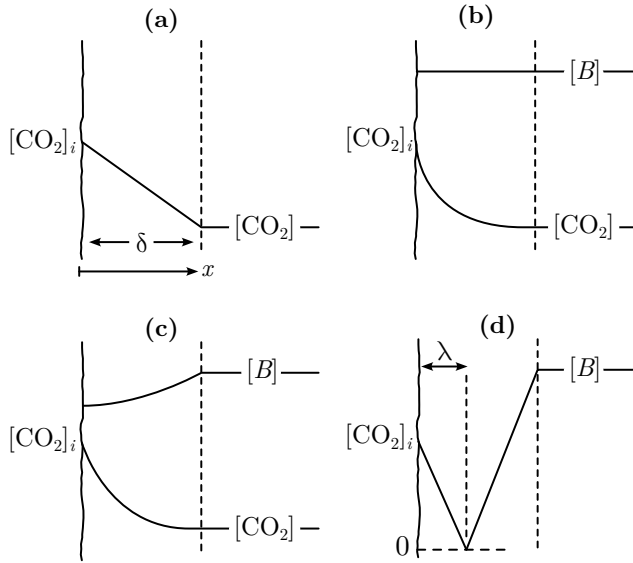


**Figure A.2:** Schematic concentration profiles in film model: (a) physical regime, and (b)-(d) reaction with nominal reactant  $B$ . (b) Pseudo-first order reaction regime; (c) partial depletion of  $B$ ; and (d) instantaneous regime.

The general case with finite reaction rate and partial depletion of  $B$  (case (c)) requires numerical solution of the coupled mass balances for  $A$  and  $B$ .

Analytical expressions for the limiting regimes (a), (b), and (d) are presented below.

### A.2.1. Physical absorption

For physical absorption, the reaction term  $r_A$  is zero. The steady-state solution of eq. (A.7), subject to boundary conditions in eq. (A.8), reads as:

$$c_A = -\frac{x}{\delta}([A]_i - [A]) + [A]_i \quad (\text{A.9})$$

Thus, in the absence of reactions, species  $A$  exhibits a linear concentration profile across the film. The absorption flux reads as:

$$N_A = -D_A \left. \frac{dc_A}{dx} \right|_{x=0} = \frac{D_A}{\delta}([A]_i - [A]) \quad (\text{A.10})$$

The prefactor in eq. (A.10) defines the liquid-side mass transfer coefficient  $k_L$ :

$$k_L = \frac{D_A}{\delta} \quad (\text{A.11})$$

Eq. (A.10) shows that without reactions, the absorption rate is proportional to the driving force ( $[A]_i - [A]$ ). The expression is therefore analogous to the liquid-side flux formulation in two-film theory (eq. (A.2)), indicating that  $K_g$  is independent of the driving force in this regime.

### A.2.2. Pseudo-first order reaction regime

Under pseudo-first order reaction regime, the concentration of the reactant  $B$  is uniform across the film (Fig. A.2.(b)) and can therefore be lumped together with the reaction rate constant, such that the resulting rate expression resembles that of a first-order system [102]. The reversible rate expression for the pseudo-first order reaction regime can be written as:

$$r_A = k_1 (c_A - [A]) \quad (\text{A.12})$$

where  $k_1$  is the pseudo first-order rate constant. The bulk concentration term in eq. (A.12) appears because the bulk liquid is assumed to be at equilibrium and ensures continuity at the film-bulk boundary. The steady state solution of eq. (A.7), subject to the boundary conditions in eq. (A.8) reads as [102]:

$$\frac{c_A - [A]}{[A]_i - [A]} = \frac{\sinh \left[ \left( \frac{D_A}{k_L} - x \right) \sqrt{\frac{k_1}{D_A}} \right]}{\sinh \left[ \frac{\sqrt{k_1 D_A}}{k_L} \right]} \quad (\text{A.13})$$

The corresponding absorption flux for a pseudo-first order reaction regime reads as:

$$N_A = -D_A \left. \frac{dc_A}{dx} \right|_{x=0} = k_L \frac{\sqrt{M}}{\tanh \sqrt{M}} ([A]_i - [A]) \quad (\text{A.14})$$

where  $\sqrt{M}$  is the Hatta number, representing the ratio of  $A$  reacting in the film to that reaching the bulk liquid:

$$M = \frac{k_1 D_A}{k_L^2} \quad (\text{A.15})$$

Comparison of eq. (A.14) with eq. (A.2) yields the enhancement factor for pseudo-first order reaction regime in the film theory:

$$E = \frac{\sqrt{M}}{\tanh \sqrt{M}} \quad (\text{A.16})$$

At sufficiently large Hatta numbers ( $\sqrt{M} > 3$ ), eq. (A.16) simplifies to  $E = \sqrt{M}$ . Combining this result with eq. (A.6) and eq. (A.15) gives the overall mass transfer coefficient  $K_g$  as:

$$K_g = H \sqrt{k_1 D_A} \quad (\text{A.17})$$

Under these conditions,  $K_g$  becomes independent of  $k_L$ . Consequently, variations in  $k_L$ , e.g., through changes in liquid agitation, no longer influence the absorption flux  $N_{\text{CO}_2}$ . Conversely, for very slow reactions ( $k_1 \rightarrow 0$ ), eq. (A.16) approaches  $E = 1$ , and the concentration profile approaches that of physical absorption.

For the reaction of  $\text{CO}_2$  and hydroxides (with the second order rate constant  $k_2$ ), the pseudo-first order reaction rate constant  $k_1$  is defined as:

$$r_f = \underbrace{k_2 [\text{OH}^-]}_{k_1} [\text{CO}_2] \quad (\text{A.18})$$

The conditions under which the pseudo-first order reaction regime applies were established by Danckwerts and Sharma [165]. For aqueous  $\text{K}_2\text{CO}_3$ , the Danckwerts criterion reads as:

$$([\text{CO}_2]_i - [\text{CO}_2]) \left( \frac{1}{[\text{CO}_3^{2-}]} + \frac{2}{[\text{HCO}_3^-]} \right) (E - 1) \ll 1 \quad (\text{A.19})$$

This conditions follows from the notion that the concentration difference of  $\text{OH}^-$  between the bulk and the interface, obtained by solving the hydroxide mass balance using the  $\text{CO}_2$  concentration profile of eq. (A.13), remains much smaller than its bulk concentration [102]. Because the absorption flux in the pseudo-first order reaction regime is sensitive to the reaction rate, the Danckwerts criterion allows for identifying the experimental conditions suitable for kinetic measurements. In aqueous  $\text{K}_2\text{CO}_3$ , this regime is often attainable due to the relatively low enhancement factors. Nevertheless, the criterion may be violated under high  $[\text{CO}_2]_i$  (resulting from high  $\text{CO}_2$  partial pressure), low  $[\text{CO}_3^{2-}]$  or  $[\text{HCO}_3^-]$  (resulting from low potassium concentration or low solvent loading), or in the presence of a fast rate promoter that increases  $E$ .

### A.2.3. Instantaneous regime

Instantaneous regime represents an asymptotic limit in which the reaction between  $A$  and  $B$  is infinitely fast. For an irreversible reaction, a reaction plane

exists within the film where the concentrations of both species are zero. The position of this reaction plane is denoted by  $\lambda$  in Fig. A.2.(d). The boundary conditions (assuming a reaction  $A + \nu B \rightarrow \text{Products}$ ) can be written as [102]:

$$\begin{cases} x = 0 : & c_A = [A]_i \\ x = \delta : & c_B = [B] \\ x = \lambda & c_A = c_B = 0, \quad -D_A \frac{dc_A}{dx} = \frac{1}{\nu} D_B \frac{dc_B}{dx} \end{cases} \quad (\text{A.20})$$

The second condition at  $x = \lambda$  reflects the stoichiometric requirement that species  $B$  must reach the reaction plane  $\nu$  times faster than species  $A$ . The concentration profiles for each species can be assumed linear and the concentration profile of  $A$  then becomes:

$$\frac{c_A}{[A]_i} = 1 - \frac{x}{\delta} \left( \frac{D_B [B]}{\nu D_A [A]_i} + 1 \right) \quad (\text{A.21})$$

Accordingly, the absorption flux of  $A$  under instantaneous regime reads as:

$$N_A = -D_A \left. \frac{dc_A}{dx} \right|_{x=0} = k_L [A]_i \left( 1 + \frac{1}{\nu} \frac{D_B [B]}{D_A [A]_i} \right) \quad (\text{A.22})$$

The enhancement factor in the instantaneous regime therefore reads as:

$$E = 1 + \frac{1}{\nu} \frac{D_B [B]}{D_A [A]_i} \quad (\text{A.23})$$

In this limit, the absorption rate is independent of reaction kinetics and is governed entirely by diffusion of the reactants toward the reaction plane. Integrating eq. (3.6) under instantaneous reaction regime (eq. (A.22)) yields the pressure decay profile for  $A = \text{CO}_2$ :

$$p_{\text{CO}_2} = \left( \frac{1}{\nu} \frac{D_B [B]}{D_{\text{CO}_2} H} + p_{\text{CO}_2,0} \right) \exp \left( -k_L R T H \frac{S}{V_g} t \right) - \frac{1}{\nu} \frac{D_B [B]}{D_{\text{CO}_2} H} \quad (\text{A.24})$$

It is evident that eq. (A.24) is not physically valid, as the asymptotic pressure ( $t \rightarrow \infty$ ) becomes negative. Nevertheless, it is notable that the exponential term depends on  $k_L$ , which in the stirred batch reactor is controlled by the stirring rate. Consequently, the response of the pressure decay to changes in stirring rate provides a clear indicator of significant depletion of non- $\text{CO}_2$  species at the gas-liquid interface.

These considerations explain the anomalies reported in **Paper I** for amine-promoted  $\text{K}_2\text{CO}_3$ . In those experiments, the pressure decay profiles in the presence of monoethanolamine (MEA) and piperazine (Pz) were observed to be very similar (Fig. 2 in **Paper I**). Additional experiments with these blends showed that the pressure decay became faster as the stirring rate was increased. Consequently, the absorption experiments in **Paper I** with MEA and Pz are inconclusive with respect to their effects on the  $\text{CO}_2$  reaction rate, other than indicating substantially faster reaction rates than blends containing  $\text{B}(\text{OH})_3$  and  $\text{V}_2\text{O}_5$ .

## Appendix B

# Sample preparation and characterization

### B.1. Blending of solvents

Aqueous  $K_2CO_3$  blends were prepared on a mass basis using  $K_2CO_3$  together with  $KHCO_3$  or  $KOH$  to obtain the desired solvent loading. The required component masses were determined from atom balances over potassium, carbon, hydrogen, and the central atom or molecule of the rate promoter (e.g., vanadium and boron in  $V_2O_5$  and  $B(OH)_3$ , the amine molecule in MEA).

For an aqueous  $K_2CO_3$  promoted with  $B(OH)_3$ , the blending problem is formulated as follows (other rate promoters follow the same procedure). At zero loading ( $\theta = 0$ ), the solvent has total mass  $m_0$  with mass fractions  $X_K$  and  $X_B$  of  $K_2CO_3$  and  $B(OH)_3$ , respectively. The water mass fraction follow the relation  $X_w = 1 - X_K - X_B$ .

Variation of solvent loading  $\theta$  by addition or removal of  $CO_2$  does not alter the total amounts of potassium, hydrogen, or boron. The corresponding atom balances read as:

$$K: \quad m_0 \frac{2X_K}{M_{K_2CO_3}} = \frac{2m_{K_2CO_3}}{M_{K_2CO_3}} + \frac{m_{KHCO_3}}{M_{KHCO_3}} + \frac{m_{KOH}}{M_{KOH}} \quad (B.1)$$

$$H: \quad m_0 \left( \frac{2X_w}{M_{H_2O}} + \frac{3X_B}{M_{B(OH)_3}} \right) = \frac{2m_{H_2O}}{M_{H_2O}} + \frac{m_{KHCO_3}}{M_{KCHO_3}} + \frac{m_{KOH}}{M_{KOH}} + \frac{3m_{B(OH)_3}}{M_{B(OH)_3}} \quad (B.2)$$

$$B: \quad m_0 \frac{X_B}{M_{B(OH)_3}} = \frac{m_{B(OH)_3}}{M_{B(OH)_3}} \quad (B.3)$$

where  $M_A$  denotes the molecular weight of  $A$ , and  $m_A$  is its mass in the blended solvent. At non-zero  $\theta$ , carbon is either added ( $\theta > 0$ ) or removed ( $\theta < 0$ ). Using the definition of  $\theta$  in terms of moles (eq. (2.1)), the carbon balance becomes:

$$C: \quad m_0 \frac{X_K}{M_{K_2CO_3}} (1 + \theta) = \frac{m_{K_2CO_3}}{M_{K_2CO_3}} + \frac{m_{KHCO_3}}{M_{KHCO_3}} \quad (\text{B.4})$$

The left-hand side of eqs. (B.1)-(B.4) correspond to the change in atom moles with respect to zero-loading.

The system of equations has a degrees of freedom +1 (no oxygen balance is written). This degree of freedom is replaced with the notion that  $KHCO_3$  and  $KOH$  cannot coexist, as upon mixing they form  $K_2CO_3$  until one reactant is exhausted. Consequently, only one can have a non-zero mass, depending on the sign of  $\theta$ :

$$\begin{cases} \theta \geq 0: & m_{KOH} = 0 \\ \theta \leq 0: & m_{KHCO_3} = 0 \end{cases} \quad (\text{B.5})$$

With this constraint, the solution of eqs. (B.1)-(B.4) becomes straightforward. This blending procedure represents a macroscopic formulation and does not account for the speciation upon mixing. Such effects are considered in this work by equilibrium calculations.

## B.2. Acid-base titration

Potentiometric titrations with  $HCl$  (1 M, standardized against  $KHCO_3$ ) were performed using an EasyPlus Easy pH titrator (Mettler Toledo) to determine the potassium concentration and solvent loading of a sample. In a titration experiment,  $HCl$  is gradually added to a diluted aliquot of the sample, while the pH and the added acid volume are recorded.

Fig. B.1 shows representative titration curves for unloaded ( $\theta = 0$ ) and loaded ( $\theta > 0$ ) aqueous  $K_2CO_3$ . Each titration is characterized by two inflection points. The first inflection ( $V_{IP_1}$ ) corresponds to consumption of  $CO_3^{2-}$ , which protonates to  $HCO_3^-$ . The second inflection ( $V_{IP_2}$ ) corresponds to further protonation of  $HCO_3^-$  to  $CO_2$ , including any pre-existing  $HCO_3^-$ . The mass balances over these inflections read as:

$$C_a V_{IP_1} = [CO_3^{2-}] V_s \quad (\text{B.6})$$

$$C_a (V_{IP_2} - V_{IP_1}) = ([CO_3^{2-}] + [HCO_3^-]) V_s \quad (\text{B.7})$$

where  $C_a$  is the monoprotic acid concentration and  $V_s$  is the aliquot volume. The concentrations of  $CO_3^{2-}$  and  $HCO_3^-$  are linked through charge and carbon atom balances. Neglecting  $H^+$ ,  $OH^-$ , and free  $CO_2$  simplifies these balances to:

$$C_K = 2[CO_3^{2-}] + [HCO_3^-], \quad C_{\text{carbon}} = [CO_3^{2-}] + [HCO_3^-] \quad (\text{B.8})$$

Solving eq. (B.6)–eq. (B.8) together with the definition of  $\theta$  (eq. (2.1)) gives:

$$C_K = C_a \frac{V_{IP_2}}{V_s}, \quad \theta = \frac{V_{IP_2} - 2V_{IP_1}}{V_{IP_2}} \quad (\text{B.9})$$

Eq. (B.9) shows that the first inflection shifts towards lower volumes as  $\theta$  increases, approaching zero when all carbon is present as  $\text{HCO}_3^-$ . The second inflection depends only on  $C_K$  and is independent of solvent loading.

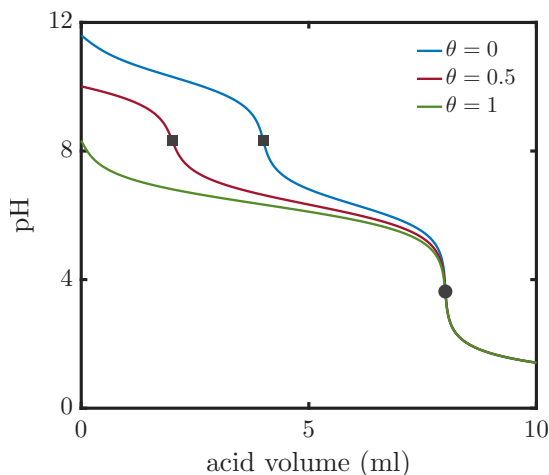


**Figure B.1:** Simulated titration curves showing pH as a function of added acid volume for aqueous  $\text{K}_2\text{CO}_3$ . Symbols: inflection points (square:  $V_{IP_1}$ , circle:  $V_{IP_2}$ ). Potassium concentration ( $C_K$ ): 4 M. Aliquot volume ( $V_s$ ): 2 ml. Acid concentration ( $C_a$ ): 1 M.

Titration of known aliquots containing boric acid showed that eq. (B.9) provides adequate predictions of  $C_K$  and  $\theta$ . Addition of  $\text{B}(\text{OH})_3$  to the alkaline solution partially protonates  $\text{CO}_3^{2-}$  while  $\text{B}(\text{OH})_3$  is converted to  $\text{B}(\text{OH})_4^-$ . The conjugate base  $\text{B}(\text{OH})_4^-$  does not produce a separate inflection, but instead contributes to  $V_{IP_1}$  due to a  $pK_a$  close to that of  $\text{HCO}_3^-$ . As a result, boron primarily dampens the first inflection without introducing a shift in the position of either inflection.

In the presence of  $\text{V}_2\text{O}_5$ , a semi-empirical model was used to determine  $\theta$  and  $C_K$ . Addition of  $\text{V}_2\text{O}_5$  lowers both inflection points without introducing additional ones. The shift in the first inflection can be interpreted by considering that vanadium undergoes two deprotonation steps to form  $\text{HVO}_4^{2-}$ , effectively acting as a strong acid. The second inflection exhibits a smaller but systematic decrease with increasing vanadium concentration. This effect could not be attributed to specific vanadate equilibria and was therefore treated empirically.

The resulting model reads as:

$$C_K = C_a \frac{V_{IP_2}}{V_s} + 2c \quad (\text{B.10})$$

$$\theta = \frac{C_a(V_{IP_2} - 2V_{IP_1}) - 2(C_V - c)V_s}{C_a V_{IP_2} + 2cV_s} \quad (\text{B.11})$$

where  $C_V$  is the vanadium concentration, accounting for the shift in the first inflection, and  $c$  is an empirical concentration term obtained from the shift in the second inflection upon addition of  $V_2O_5$  to the unpromoted mixture.

$$c = \frac{1}{2} C_a \frac{V_{IP_2}^{(w/V)} - V_{IP_2}^{(w/oV)}}{V_s} \quad (\text{B.12})$$

# Acknowledgements

First and foremost, I would like to express my sincere gratitude to my main supervisor, **Matthäus Bähler**, for his trust, patience, support, and guidance throughout this journey but even more, for his friendship. I will always be grateful for the honor to have worked with you.

I also thank my co-supervisor, **Efthymios Kantarelis**, for his support and guidance, particularly during the early stages of my PhD and in the lab, as well as for his patience in answering my many (read: trivial) questions.

I also thank dear friends and colleagues, past and present, at the Division of Process Technology for the emotional support. To my fellow PhD students, **Pol, Pedro, Soledad, Jacob, Ziqian, Malin, Giorgio**, and **Baláza**, good luck and thank you for making being at work fun. I send my love to **Steven, Ronald, Elise**, and **Marc** for the many great, mostly nonsensical, discussions, countless fika breaks, and most of all, their friendship.

I also thank **Erik Dahlén** and **Kåre Gustafsson** from Stockholm Exergi AB, **Jens Wolf** and **Ola Augustsson** from Captimise AB. It was a great privilege to be involved in the BECCS pilot and I am very grateful for this invaluable experience.

This work would not have been possible without the contributions of my former master's thesis students: **Arturo, Aishwarya**, and **Ville**. I hope they learned as much from me as I did from them. I would especially like to thank **Florian Walthert** for his diligent work on the absorption setup, who improved my original build to its much better, current state. Florian truly enabled the results of this work.

Financial support from the **Energimyndigheten** and **Stockholm Exergi AB** is gratefully acknowledged.

Most of all, I thank my wife **Sofia**, for her never-ending patience and support throughout these years, and for standing by me in my hardest moments. I am deeply grateful to my parents **Ali** and **Sharareh**, for inspiring and supporting me all my life. It was Dad who set me on the path to become a chemical engineer, and his memory is present in every line of this thesis.

**Use of Generative AI.** I declare the use of generative AI (**ChatGPT**) in writing this thesis. All the content presented in this thesis were collected, analyzed, and written by me. The use of AI was limited at the final step for identifying language issues. Any suggestions by the AI were reviewed and selected by me.

# Bibliography

- [1] P. L. Lucas, D. P. van Vuuren, J. G. J. Olivier, and M. G. J. den Elzen. Long-term reduction potential of non-CO<sub>2</sub> greenhouse gases. *Environmental Science & Policy*, 10(2):85–103, 2007. URL <https://doi.org/10.1016/j.envsci.2006.10.007>.
- [2] A. S. Denning. Where has all the carbon gone? *Annual Review of Earth and Planetary Sciences*, 50(1):55–78, 2022. URL <https://doi.org/10.1146/annurev-earth-032320-092010>.
- [3] M. R. Allen, P. Friedlingstein, C. A. J. Girardin, S. Jenkins, Y. Malhi, E. Mitchell-Larson, G. P. Peters, and L. Rajamani. Net zero: science, origins, and implications. *Annual Review of Environment and Resources*, 47(1):849–887, 2022. URL <https://doi.org/10.1146/annurev-environ-112320-105050>.
- [4] V. Bolongaro, V. Becattini, and M. Mazzotti. Understanding Climate Change by Modeling the Earth’s Atmosphere as a Well-Stirred Tank. *Chemie Ingenieur Technik*, 96(12):1779–1796, 2024. URL <https://doi.org/10.1002/cite.202400117>.
- [5] NOAA Global Monitoring Laboratory and United States Environmental Protection Agency. Dataset: Annual concentration of atmospheric carbon dioxide (major processing by Our World in Data). 2025. URL <https://archive.ourworldindata.org/20251117-103742/grapher/co2-long-term-concentration.html>.
- [6] Met Office Hadley Centre – HadCRUT5. Dataset: Global average temperature anomaly relative to 1861–1890 (major processing by Our World in Data). 2025. URL <https://ourworldindata.org/grapher/temperature-anomaly>.
- [7] S. Dietz, A. Bowen, B. Doda, A. Gambhir, and R. Warren. The economics of 1.5 °C climate change. *Annual Review of Environment and Resources*, 43(1):455–480, 2018. URL <https://doi.org/10.1146/annurev-environ-102017-025817>.
- [8] J. Rogelj, O. Geden, A. Cowie, and A. Reisinger. Net-zero emissions targets are vague: three ways to fix. *Nature*, 591(7850):365–368, 2021. URL <https://www.nature.com/articles/d41586-021-00662-3>.
- [9] V. M. Nik, A. T. D. Perera, and D. Chen. Towards climate resilient urban energy systems: a review. *National Science Review*, 8(3):nwaa134, 2021. URL <https://doi.org/10.1093/nsr/nwaa134>.

- [10] F. Creutzig, B. Fernandez, H. Haberl, R. Khosla, Y. Mulugetta, and K. C. Seto. Beyond Technology: Demand-Side Solutions for Climate Change Mitigation. *Annual Review of Environment and Resources*, 41(1):173–198, 2016. URL <https://doi.org/10.1146/annurev-environ-110615-085428>.
- [11] D. P. van Vuuren, E. Stehfest, D. E. H. J. Gernaat, M. van den Berg, D. L. Bijl, H. S. de Boer, V. Daioglou, J. C. Doelman, O. Y. Edelenbosch, M. Harmsen, A. F. Hof, and M. A. E. van Sluisvel. Alternative pathways to the 1.5 °C target reduce the need for negative emission technologies. *Nature Climate Change*, 8(5): 391–397, 2018. URL <https://doi.org/10.1038/s41558-018-0119-8>.
- [12] A. Gailani, S. Cooper, S. Allen, A. Pimm, P. Taylor, and R. Gross. Assessing the potential of decarbonization options for industrial sectors. *Joule*, 8(3):576–603, 2024. URL <https://doi.org/10.1016/j.joule.2024.01.007>.
- [13] T. P. Hendrickson, N. Abhyankar, P. Mohanty, K. K. Mayfield, W. Kirkendall, A. J. Stanley, S. Stack, H. Yang, and A. J. Satchwell. Decarbonizing the US Energy System. *Annual Review of Environment and Resources*, 49:163–189, 2024. URL <https://doi.org/10.1146/annurev-environ-112321-091927>.
- [14] Y. Ou, C. Roney, J. Alsalam, K. Calvin, J. Creason, J. Edmonds, A. A. Fawcett, P. Kyle, K. Narayan, P. O'Rourke, P. Patel, S. Ragnauth, S. J. Smith, and H. McJeon. Deep mitigation of CO<sub>2</sub> and non-CO<sub>2</sub> greenhouse gases toward 1.5 °C and 2 °C futures. *Nature Communications*, 12(1):6245, 2021. URL <https://doi.org/10.1038/s41467-021-26509-z>.
- [15] V. Dufour-Décieux, K. Sievert, B. Steffen, A. Bardow, and T. S. Schmidt. (How to) avoid the inflationary labeling of emissions as “hard to abate”. *Joule*, 9(7): 102039, 2025. URL <https://doi.org/10.1016/j.joule.2025.102039>.
- [16] S. Fankhauser, S. M. Smith, M. Allen, K. Axelsson, T. Hale, C. Hepburn, J. M. Kendall, R. Khosla, J. Lezaun, E. Mitchell-Larson, M. Obersteiner, L. Rjamani, R. Rickaby, N. Seddon, and T. Wetzer. The meaning of net zero and how to get it right. *Nature Climate Change*, 12(1):15–21, 2022. URL <https://doi.org/10.1038/s41558-021-01245-w>.
- [17] M. R. Allen, D. J. Frame, P. Friedlingstein, N. P. Gillett, G. Grassi, J. M. Gregory, W. Hare, J. House, C. Huntingford, S. Jenkins, C. D. Jones, R. Knutti, J. A. Lowe, H. D. Matthews, M. Meinshausen, N. Meinshausen, G. P. Peters, G. Plattner, S. Raper, J. Rogelj, P. A. Stott, S. Solomon, T. F. Stocker, A. J. Weaver, and K. Zickfeld. Geological Net Zero and the need for disaggregated accounting for carbon sinks. *Nature*, 638(8050):343–350, 2025. URL <https://doi.org/10.1038/s41586-024-08326-8>.
- [18] K. Kloesel, V. Bolongaro, P. Gabrielli, V. Becattini, and M. Mazzotti. Carbon Dioxide Reduction and Removal toward Net-Zero: A Needed Change of Narrative. *Industrial & Engineering Chemistry Research*, 64(31):15478–15486, 2025. URL <https://doi.org/10.1021/acs.iecr.5c00684>.

- [19] P. Williamson. Emissions reduction: Scrutinize CO<sub>2</sub> removal methods. *Nature*, 530(7589):153–155, 2016. URL <https://doi.org/10.1038/530153a>.
- [20] S. Fuss, W. F. Lamb, M. W. Callaghan, J. Hilaire, F. Creutzig, T. Amann, T. Beringer, W. de Oliveira Garcia, J. Hartmann, T. Khanna, G. Luderer, G. F. Nemet, J. Rogelj, P. Smith, J. L. Vicente Vicente, J. Wilcox, M. del Mar Zamora Dominguez, and J. C. Minx. Negative emissions – Part 2: Costs, potentials and side effects. *Environmental Research Letters*, 13(6):063002, 2018. URL <https://doi.org/10.1088/1748-9326/aabf9f>.
- [21] S. Chiquier, P. Patrizio, M. Bui, N. Sunny, and N. Mac Dowell. A comparative analysis of the efficiency, timing, and permanence of CO<sub>2</sub> removal pathways. *Energy & Environmental Science*, 15(10):4389–4403, 2022. URL <https://doi.org/10.1039/d2ee01021f>.
- [22] A. Deprez, P. Leadley, K. Dooley, P. Williamson, W. Cramer, J. Gattuso, A. Rankovic, E. L. Carlson, and F. Creutzig. Sustainability limits needed for CO<sub>2</sub> removal. *Science*, 383(6682):484–486, 2024. URL <https://doi.org/10.1126/science.adj6171>.
- [23] F. Cherubini, G. P. Peters, T. Berntsen, A. H. Strømman, and E. Hertwich. CO<sub>2</sub> emissions from biomass combustion for bioenergy: atmospheric decay and contribution to global warming. *GCB Bioenergy*, 3(5):413–426, 2011. URL <https://doi.org/10.1111/j.1757-1707.2011.01102.x>.
- [24] C. D. Jones, P. Ciais, S. J. Davis, P. Friedlingstein, T. Gasser, G. P. Peters, J. Rogelj, D. P. van Vuuren, J. G. Canadell, A. Cowie, R. B. Jackson, M. Jonas, E. Kriegler, E. Littleton, J. A. Lowe, J. Milne, G. Shrestha, P. Smith, A. Torvanger, and A. Wiltshire. Simulating the Earth system response to negative emissions. *Environmental Research Letters*, 11(9):095012, 2016. URL <https://doi.org/10.1146/10.1088/1748-9326/11/9/095012>.
- [25] Å. Persson, O. Johansson Stenman, E. Lerum Boasson, F. Johnsson, E. Kjellström, M. Pettersson, H. Smith, and H. Wibeck. Report of the Swedish Climate Policy Council 2025. URL <https://www.klimatpolitiskaradet.se/en/report-2025/>.
- [26] L. Rosa, D. L. Sanchez, and M. Mazzotti. Assessment of carbon dioxide removal potential via BECCS in a carbon-neutral Europe. *Energy & Environmental Science*, 14(5):3086–3097, 2021. URL <https://doi.org/10.1039/D1EE00642H>.
- [27] M. Dufour, K. Möllersten, and L. Zetterberg. How to maintain environmental integrity when using state support and the VCM to co-finance BECCS projects - a Swedish case study. *Frontiers in Environmental Science*, 12:1387138, 2024. URL <https://doi.org/10.3389/fenvs.2024.1387138>.
- [28] F. Levihn, L. Linde, K. Gustafsson, and E. Dahlen. Introducing BECCS through HPC to the research agenda: The case of combined heat and power in Stockholm. *Energy Reports*, 5:1381–1389, 2019. URL <https://doi.org/10.1016/j.egyrs.2019.09.018>.

- [29] A. G. Eickmeyer. Removal of CO<sub>2</sub> from gas mixtures, February 7 1984. US Patent 4,430,312.
- [30] P. Oeuuvray, J. Burger, S. Roussanaly, M. Mazzotti, and V. Becattini. Multi-criteria assessment of inland and offshore carbon dioxide transport options. *Journal of Cleaner Production*, 443:140781, 2024. URL <https://doi.org/10.1016/j.jclepro.2024.140781>.
- [31] K. Z. House, A. C. Baclig, M. Ranjan, E. A. Van Nierop, J. Wilcox, and H. J. Herzog. Economic and energetic analysis of capturing CO<sub>2</sub> from ambient air. *Proceedings of the National Academy of Sciences*, 108(51):20428–20433, 2011. URL <https://www.pnas.org/doi/abs/10.1073/pnas.1012253108>.
- [32] J. Wilcox, R. Haghpanah, E. C. Rupp, J. He, and K. Lee. Advancing Adsorption and Membrane Separation Processes for the Gigaton Carbon Capture Challenge. *Annual Review of Chemical and Biomolecular Engineering*, 5(1):479–505, 2014. URL <https://doi.org/10.1146/annurev-chembioeng-060713-040100>.
- [33] X. Wu, R. Krishnamoorti, and P. Bollini. Technological Options for Direct Air Capture: A Comparative Process Engineering Review. *Annual Review of Chemical and Biomolecular Engineering*, 13(1):279–300, 2022. URL <https://doi.org/10.1146/annurev-chembioeng-102121-065047>.
- [34] H. Ritchie. Sector by sector: where do global greenhouse gas emissions come from? *Our World in Data*, 2020. URL <https://archive.ourworldindata.org/20251125-173858/ghg-emissions-by-sector.html>.
- [35] S. Anderson and R. Newell. Prospects for carbon capture and storage technologies. *Annual Review of Environment and Resources*, 29(1):109–142, 2004. URL <https://doi.org/10.1146/annurev.energy.29.082703.145619>.
- [36] R. J. Notz, I. Toennies, N. McCann, G. Scheffknecht, and H. Hasse. CO<sub>2</sub> capture for fossil fuel-fired power plants. *Chemical Engineering & Technology*, 34(2):163–172, 2011. URL <https://doi.org/10.1002/ceat.201000491>.
- [37] C. Chao, Y. Deng, R. Dewil, J. Baeyens, and X. Fan. Post-combustion carbon capture. *Renewable and Sustainable Energy Reviews*, 138:110490, 2021. URL <https://doi.org/10.1016/j.rser.2020.110490>.
- [38] S. E. Zanco, J. F. Pérez-Calvo, A. Gasós, B. Cordiano, V. Becattini, and M. Mazzotti. Postcombustion CO<sub>2</sub> capture: a comparative techno-economic assessment of three technologies using a solvent, an adsorbent, and a membrane. *ACS Engineering Au*, 1(1):50–72, 2021. URL <https://doi.org/10.1021/acseengineeringau.1c00002>.
- [39] K. Sievert, T. S. Schmidt, and B. Steffen. Considering technology characteristics to project future costs of direct air capture. *Joule*, 8(4):979–999, 2024. URL <https://doi.org/10.1016/j.joule.2024.02.005>.

- [40] A. Aspelund and K. Jordal. Gas conditioning - The interface between CO<sub>2</sub> capture and transport. *International Journal of Greenhouse Gas Control*, 1(3):343–354, 2007. URL [https://doi.org/10.1016/S1750-5836\(07\)00040-0](https://doi.org/10.1016/S1750-5836(07)00040-0).
- [41] H. Deng, S. Roussanaly, and G. Skaugen. Techno-economic analyses of CO<sub>2</sub> liquefaction: Impact of product pressure and impurities. *International Journal of Refrigeration*, 103:301–315, 2019. URL <https://doi.org/10.1016/j.ijrefrig.2019.04.011>.
- [42] W. Gong, E. Remiezowicz, P. L. Fosbøl, and N. von Solms. Design and Analysis of Novel CO<sub>2</sub> Conditioning Process in Ship-Based CCS. *Energies*, 15(16):5928, 2022. URL <https://doi.org/10.3390/en15165928>.
- [43] Y. Seo, C. Huh, S. Lee, and D. Chang. Comparison of CO<sub>2</sub> liquefaction pressures for ship-based carbon capture and storage (CCS) chain. *International Journal of Greenhouse Gas Control*, 52:1–12, 2016. URL <https://doi.org/10.1016/j.ijggc.2016.06.011>.
- [44] V. E. Onyebuchi, A. Kolios, D. P. Hanak, C. Biliyok, and V. Manovic. A systematic review of key challenges of CO<sub>2</sub> transport via pipelines. *Renewable and Sustainable Energy Reviews*, 81:2563–2583, 2018. URL <https://doi.org/10.1016/j.rser.2017.06.064>.
- [45] V. Becattini, P. Gabrielli, C. Antonini, J. Campos, A. Acquilino, G. Sansavini, and M. Mazzotti. Carbon dioxide capture, transport and storage supply chains: Optimal economic and environmental performance of infrastructure rollout. *International Journal of Greenhouse Gas Control*, 117:103635, 2022. URL <https://doi.org/10.1016/j.ijggc.2022.103635>.
- [46] J. Nöhl, J. Burger, P. Oeuvray, V. Becattini, J. Seiler, D. Y. Shu, M. Mazzotti, and A. Bardow. How to transport carbon dioxide with minimal environmental impacts today and tomorrow? A prospective life cycle assessment. *Journal of Cleaner Production*, 514:145659, 2025. URL <https://doi.org/10.1016/j.jclepro.2025.145659>.
- [47] S. Roussanaly, H. Deng, G. Skaugen, and T. Gundersen. At what pressure shall CO<sub>2</sub> be transported by ship? An in-depth cost comparison of 7 and 15 barg shipping. *Energies*, 14(18):5635, 2021. URL <https://doi.org/10.3390/en14185635>.
- [48] J. Burger, J. Nöhl, J. Seiler, P. Gabrielli, P. Oeuvray, V. Becattini, A. Reyes-Lúa, L. Riboldi, G. Sansavini, and A. Bardow. Environmental impacts of carbon capture, transport, and storage supply chains: Status and the way forward. *International Journal of Greenhouse Gas Control*, 132:104039, 2024. URL <https://doi.org/10.1016/j.ijggc.2023.104039>.
- [49] H. de Coninck and S. M. Benson. Carbon Dioxide Capture and Storage: Issues and Prospects. *Annual Review of Environment and Resources*, 39(1):243–270, 2014. URL <https://doi.org/10.1146/annurev-environ-032112-095222>.

- [50] M. J. Gidden, S. Joshi, J. J. Armitage, A. Christ, M. Boettcher, E. Brutschin, A. C. Köberle, K. Riahi, H. J. Schellnhuber, C. Schleussner, and J. Rogelij. A prudent planetary limit for geologic carbon storage. *Nature*, 645(8079):124–132, 2025. URL <https://doi.org/10.1038/s41586-025-09423-y>.
- [51] J. Alcalde, S. Flude, M. Wilkinson, G. Johnson, K. Edlmann, C. E. Bond, V. Scott, S. M. V. Gilfillan, X. Ogaya, and R. S. Haszeldine. Estimating geological CO<sub>2</sub> storage security to deliver on climate mitigation. *Nature Communications*, 9(1):2201, 2018. URL <https://doi.org/10.1038/s41467-018-04423-1>.
- [52] J. Wang, D. Ryan, E. J. Anthony, A. Wigston, L. Basava-Reddi, and N. Wildgust. The effect of impurities in oxyfuel flue gas on CO<sub>2</sub> storage capacity. *International Journal of Greenhouse Gas Control*, 11:158–162, 2012. URL <https://doi.org/10.1016/j.ijggc.2012.08.002>.
- [53] L. Rycroft, F. Neele, K. B. Bruun, R. Meneguolo, J. de Moor, W. Schiferli, T. G. G. Candela, S. Ó Snæbjörnsdóttir, N. Hoffman, and S. O’Brien. Chapter four - Geological storage of CO<sub>2</sub>. In Lydia R. and Filip N., editors, *Deployment of Carbon Capture and Storage*, Woodhead Publishing Series on Carbon Capture and Storage, pages 133–266. Woodhead Publishing, 2024. ISBN 978-0-323-95498-3. URL <https://doi.org/10.1016/B978-0-323-95498-3.00003-1>.
- [54] E. G. Nikolaidou, E. Nessi, P. Seferlis, and A. I. Papadopoulos. The role of impurities in CCS from pilot capture plants to sequestration sites – A review. *International Journal of Greenhouse Gas Control*, 145:104410, 2025. URL <https://doi.org/10.1016/j.ijggc.2025.104410>.
- [55] A. Martin, V. Becattini, C. Marieni, S. Kolbeinsdóttir, M. Mazzotti, and T. Gunatilake. Potential and challenges of underground CO<sub>2</sub> storage via in-situ mineralization in Switzerland. *Swiss Journal of Geosciences*, 118(1):1, 2025. URL <https://doi.org/10.1186/s00015-024-00473-4>.
- [56] C. Hepburn, E. Adlen, J. Beddington, E. A. Carter, S. Fuss, N. Mac Dowell, J. C. Minx, P. Smith, and C. K. Williams. The technological and economic prospects for CO<sub>2</sub> utilization and removal. *Nature*, 575(7781):87–97, 2019. URL <https://doi.org/10.1038/s41586-019-1681-6>.
- [57] O. S. Bushuyev, P. De Luna, C. T. Dinh, L. Tao, G. Saur, J. van de Lagemaat, S. O. Kelley, and E. H. Sargent. What Should We Make with CO<sub>2</sub> and How Can We Make It? *Joule*, 2(5):825–832, 2018. URL <https://doi.org/10.1016/j.joule.2017.09.003>.
- [58] N. Mac Dowell, P. S. Fennell, N. Shah, and G. C. Maitland. The role of CO<sub>2</sub> capture and utilization in mitigating climate change. *Nature Climate Change*, 7(4):243–249, 2017. URL <https://doi.org/10.1038/nclimate3231>.
- [59] A. Gasós, R. Pini, V. Becattini, and M. Mazzotti. Carbon footprint of oil produced through enhanced oil recovery using carbon dioxide directly captured from air.

- Energy & Environmental Science*, 18:7440–7446, 2025. URL <http://dx.doi.org/10.1039/D5EE01752A>.
- [60] G. Astarita, D. W. Savage, and A. Bisio. *Gas treating with chemical solvents*. J. Wiley and Sons, New York, NY, 1983.
- [61] A. L. Kohl and R. Nielsen. *Gas purification*. Elsevier, 5 edition, 1997.
- [62] H. E. Benson, J. H. Field, and R. M. Jameson. CO<sub>2</sub> absorption employing hot potassium carbonate solutions. *Chemical Engineering Progress*, 50(7), 1954.
- [63] A. Kothandaraman. *Carbon dioxide capture by chemical absorption: a solvent comparison study*. Massachusetts Institute of Technology, 2010. URL <http://hdl.handle.net/1721.1/59877>.
- [64] J. Oexmann, C. Hensel, and A. Kather. Post-combustion CO<sub>2</sub>-capture from coal-fired power plants: Preliminary evaluation of an integrated chemical absorption process with piperazine-promoted potassium carbonate. *International Journal of Greenhouse Gas Control*, 2(4):539–552, 2008. URL <https://doi.org/10.1016/j.ijggc.2008.04.002>.
- [65] T. Harkin, A. Hoadley, and B. Hooper. Using multi-objective optimisation in the design of CO<sub>2</sub> capture systems for retrofit to coal power stations. *Energy*, 41(1): 228–235, 2012. URL <https://doi.org/10.1016/j.energy.2011.06.031>.
- [66] Y. Le Moullec and T. Neveux. Chapter 13 - process modifications for CO<sub>2</sub> capture. In P. H. M. Feron, editor, *Absorption-Based Post-combustion Capture of Carbon Dioxide*, pages 305–340. Woodhead Publishing, 2016. URL <https://doi.org/10.1016/B978-0-08-100514-9.00013-5>.
- [67] J. Oexmann and A. Kather. Minimising the regeneration heat duty of post-combustion CO<sub>2</sub> capture by wet chemical absorption: The misguided focus on low heat of absorption solvents. *International Journal of Greenhouse Gas Control*, 4(1):36–43, 2010. URL <https://doi.org/10.1016/j.ijggc.2009.09.010>.
- [68] J. F. Pérez-Calvo, D. Sutter, M. Gazzani, and M. Mazzotti. A methodology for the heuristic optimization of solvent-based CO<sub>2</sub> capture processes when applied to new flue gas compositions: A case study of the chilled ammonia process for capture in cement plants. *Chemical Engineering Science: X*, 8:100074, 2020. URL <https://doi.org/10.1016/j.cesx.2020.100074>.
- [69] G. Puxty, M. Maeder, and T. Moore. The Chemistry and Thermodynamics of Point Source CO<sub>2</sub> Capture by Liquid Chemical Absorption and Its Impact on Process Performance. *Chemical Reviews*, 125(22):10956–10993, 2025. URL <https://doi.org/10.1021/acs.chemrev.5c00377>.
- [70] G. F. Versteeg, L. A. J. Van Dijk, and W. P. M. van Swaaij. On the kinetics between CO<sub>2</sub> and alkanolamines both in aqueous and non-aqueous solutions. An overview. *Chemical Engineering Communications*, 144(1):113–158, 1996. URL <https://doi.org/10.1080/00986449608936450>.

- [71] G. Sartori and D. W. Savage. Sterically hindered amines for carbon dioxide removal from gases. *Industrial & Engineering Chemistry Fundamentals*, 22(2):239–249, 1983. URL <https://doi.org/10.1021/i100010a016>.
- [72] J. T. Cullinane and G. T. Rochelle. Carbon dioxide absorption with aqueous potassium carbonate promoted by piperazine. *Chemical Engineering Science*, 59(17):3619–3630, 2004. URL <https://doi.org/10.1016/j.ces.2004.03.029>.
- [73] D. Morlando, V. Buvik, A. Delic, A. Hartono, H. F. Svendsen, H. M. Kvamsdal, E. F. da Silva, and H. K. Knuutila. Available data and knowledge gaps of the CESAR1 solvent system. *Carbon Capture Science & Technology*, 13:100290, 2024. URL <https://doi.org/10.1016/j.ccst.2024.100290>.
- [74] S. Bishnoi and G. T. Rochelle. Absorption of carbon dioxide in aqueous piperazine/methyldiethanolamine. *AIChE Journal*, 48(12):2788–2799, 2002. URL <https://doi.org/10.1002/aic.690481208>.
- [75] Y. Du, Y. Yuan, and G. T. Rochelle. Capacity and absorption rate of tertiary and hindered amines blended with piperazine for CO<sub>2</sub> capture. *Chemical Engineering Science*, 155:397–404, 2016. URL <https://doi.org/10.1016/j.ces.2016.08.017>.
- [76] S. Freguia and G. T. Rochelle. Modeling of CO<sub>2</sub> capture by aqueous monoethanolamine. *AIChE Journal*, 49(7):1676–1686, 2003. URL <https://doi.org/10.1002/aic.690490708>.
- [77] G. T. Rochelle. Air pollution impacts of amine scrubbing for CO<sub>2</sub> capture. *Carbon Capture Science & Technology*, 11:100192, 2024. URL <https://doi.org/10.1016/j.ccst.2024.100192>.
- [78] X. Wang, W. Conway, D. Fernandes, G. Lawrance, R. Burns, G. Puxty, and M. Maeder. Kinetics of the reversible reaction of CO<sub>2</sub>(aq) with ammonia in aqueous solution. *The Journal of Physical Chemistry A*, 115(24):6405–6412, 2011. URL <https://doi.org/10.1021/jp108491a>.
- [79] J. Du, W. Yang, L. Xu, L. Bei, S. Lei, W. Li, H. Liu, B. Wang, and L. Sun. Review on post-combustion CO<sub>2</sub> capture by amine blended solvents and aqueous ammonia. *Chemical Engineering Journal*, page 150954, 2024. URL <https://doi.org/10.1016/j.cej.2024.150954>.
- [80] O. Augustsson, B. Baburao, S. Dube, S. Bedell, P. Strunz, M. Balfe, and O. Stallmann. Chilled ammonia process scale-up and lessons learned. *Energy Procedia*, 114:5593–5615, 2017. URL <https://doi.org/10.1016/j.egypro.2017.03.1699>.
- [81] G. Puxty, R. Rowland, and M. Attalla. Comparison of the rate of CO<sub>2</sub> absorption into aqueous ammonia and monoethanolamine. *Chemical Engineering Science*, 65(2):915–922, 2010. URL <https://doi.org/10.1016/j.ces.2009.09.042>.
- [82] P. S. Kumar, J. A. Hogendoorn, G. F. Versteeg, and P. H. M. Feron. Kinetics of the reaction of CO<sub>2</sub> with aqueous potassium salt of taurine and glycine. *AIChE Journal*, 49(1):203–213, 2003. URL <https://doi.org/10.1002/aic.690490118>.

- [83] U. E. Aronu, A. Hartono, K. A. Hoff, and H. F. Svendsen. Kinetics of carbon dioxide absorption into aqueous amino acid salt: Potassium salt of sarcosine solution. *Industrial & Engineering Chemistry Research*, 50(18):10465–10475, 2011. URL <https://doi.org/10.1021/ie200596y>.
- [84] Q. Xiang, M. Fang, H. Yu, and M. Maeder. Kinetics of the reversible reaction of  $\text{CO}_2(\text{aq})$  and  $\text{HCO}_3^-$  with sarcosine salt in aqueous solution. *The Journal of Physical Chemistry A*, 116(42):10276–10284, 2012. URL <https://doi.org/10.1021/jp305715q>.
- [85] A. Kiani, W. Conway, M. H. Abdellah, G. Puxty, A. J. Minor, G. Kluivers, R. Bennett, and P. Feron. A study on degradation and  $\text{CO}_2$  capture performance of aqueous amino acid salts for direct air capture applications. *Greenhouse Gases: Science and Technology*, 14(5):859–870, 2024. URL <https://doi.org/10.1002/ghg.2302>.
- [86] F. O. Ochedi, J. Andresen, and M. Van der Spek. Oxidative degradation of glycine in aqueous  $\text{KOH}/\text{K}_2\text{CO}_3$  solutions for  $\text{CO}_2$  capture. *Greenhouse Gases: Science and Technology*, 14(6):1025–1036, 2024. URL <https://doi.org/10.1002/ghg.2310>.
- [87] H. J. Song, S. Lee, K. Park, J. Lee, D. Chand Spah, J. W. Park, and T. P. Filburn. Simplified estimation of regeneration energy of 30 wt% sodium glycinate solution for carbon dioxide absorption. *Industrial & Engineering Chemistry Research*, 47(24):9925–9930, 2008. URL <https://doi.org/10.1021/ie8007117>.
- [88] H. Knuutila, U. E. Aronu, H. M. Kvamsdal, and A. Chikukwa. Post combustion  $\text{CO}_2$  capture with an amino acid salt. *Energy Procedia*, 4:1550–1557, 2011. URL <https://doi.org/10.1016/j.egypro.2011.02.024>.
- [89] M. Rabensteiner, G. Kinger, M. Koller, and C. Hoehenauer. PCC pilot plant studies with aqueous potassium glycinate. *International Journal of Greenhouse Gas Control*, 42:562–570, 2015. URL <https://doi.org/10.1016/j.ijggc.2015.09.012>.
- [90] A. Kasturi, G. G. Jang, D. Stamberg, R. Custelcean, S. Yiacoumi, and C. Tsouris. Determination of the regeneration energy of direct air capture solvents/sorbents using calorimetric methods. *Separation and Purification Technology*, 310:123154, 2023. URL <https://doi.org/10.1016/j.seppur.2023.123154>.
- [91] K. A. Garrabrant, N. J. Williams, E. Holguin, F. M. Brethomé, C. Tsouris, and R. Custelcean. Energy-efficient  $\text{CO}_2$  capture from flue gas by absorption with amino acids and crystallization with a bis-iminoguanidine. *Industrial & Engineering Chemistry Research*, 58(24):10510–10515, 2019. URL <https://doi.org/10.1021/acs.iecr.9b00954>.
- [92] R. Custelcean. Direct Air Capture of  $\text{CO}_2$  Using Solvents. *Annual Review of Chemical and Biomolecular Engineering*, 13(1):217–234, 2022. URL <https://doi.org/10.1146/annurev-chembioeng-092120-023936>.

- [93] J. K. Stolaroff. Carbonate solutions for carbon capture: A summary. Technical report, Lawrence Livermore National Lab.(LLNL), Livermore, CA (United States), 2013. URL <https://doi.org/10.2172/1097716>.
- [94] G. Hu, N. J. Nicholas, K. H. Smith, K. A. Mumford, S. E. Kentish, and G. W. Stevens. Carbon dioxide absorption into promoted potassium carbonate solutions: A review. *International Journal of Greenhouse Gas Control*, 53:28–40, 2016. URL <https://doi.org/10.1016/j.ijggc.2016.07.020>.
- [95] K. Gustafsson, R. Sadegh-Vaziri, S. Grönkvist, F. Levihn, and C. Sundberg. BECCS with combined heat and power: Assessing the energy penalty. *International Journal of Greenhouse Gas Control*, 110:103434, 2021. URL <https://doi.org/10.1016/j.ijggc.2020.103248>.
- [96] T. R. Kumar, J. Beiron, M. Biermann, S. Harvey, and H. Thunman. Plant and system-level performance of combined heat and power plants equipped with different carbon capture technologies. *Applied Energy*, 338:120927, 2023. URL <https://doi.org/10.1016/j.apenergy.2023.120927>.
- [97] J. S. Tosh, J. H. Field, H. E. Benson, and W. P. Haynes. Equilibrium study of the system potassium carbonate, potassium bicarbonate, carbon dioxide, and water. Technical report, Bureau of Mines, Pittsburgh, Pa. (USA), 12 1958. URL <https://www.osti.gov/biblio/7199456>.
- [98] M. R. M. Abu-Zahra, L. H. J. Schneiders, J. P. M. Niederer, P. H. M. Feron, and G. F. Versteeg. CO<sub>2</sub> capture from power plants: Part I. A parametric study of the technical performance based on monoethanolamine. *International Journal of Greenhouse gas control*, 1(1):37–46, 2007. URL [https://doi.org/10.1016/S1750-5836\(06\)00007-7](https://doi.org/10.1016/S1750-5836(06)00007-7).
- [99] K. Smith, G. Xiao, K. Mumford, J. Gouw, I. Indrawan, N. Thanumurthy, D. Quyn, R. Cuthbertson, A. Rayer, N. Nicholas, A. Lee, G. da Silva, S. Kentish, T. Harkin, A. Qader, C. Anderson, B. Hooper, and G. Stevens. Demonstration of a concentrated potassium carbonate process for CO<sub>2</sub> capture. *Energy & Fuels*, 28(1): 299–306, 2014. URL <https://doi.org/10.1021/ef4014746>.
- [100] E. Dahlén, K. Gustafsson, O. Augustsson, H. Larsson, M. Olofsson, S. Fransson, L. Jonsson, N. Mirzaei, M. Choupani, M. Båbler, M. Jones, H. Brännström, and S. Hedlund. Utvidgade tester av BECCS genom HPC vid kraftvärmeverk. Technical report, Swedish Energy Agency, 2022. URL <https://www.energimyndigheten.se/forskning-och-innovation/data-om-finansiering-av-forskning-och-innovation/projektdatabas/sokresultat/?registrationnumber=2020-012179>.
- [101] X. Wang, W. Conway, R. Burns, N. McCann, and M. Maeder. Comprehensive study of the hydration and dehydration reactions of carbon dioxide in aqueous solution. *The Journal of Physical Chemistry A*, 114(4):1734–1740, 2010. URL <https://doi.org/10.1021/jp909019u>.

- [102] P. V. Danckwerts. *Gas-liquid reactions*. McGraw-Hill New York, 1970.
- [103] G. Astarita, D. W. Savage, and J. M. Longo. Promotion of CO<sub>2</sub> mass transfer in carbonate solutions. *Chemical Engineering Science*, 36(3):581–588, 1981. URL [https://doi.org/10.1016/0009-2509\(81\)80146-7](https://doi.org/10.1016/0009-2509(81)80146-7).
- [104] M. Imle, J. Kumelan, D. Speyer, N. McCann, G. Maurer, and H. Hasse. Solubility of carbon dioxide in activated potash solutions in the low and high gas loading regions. *Industrial & Engineering Chemistry Research*, 52(37):13477–13489, 2013. URL <https://doi.org/10.1021/ie401835x>.
- [105] M. M. Sharma and P. V. Danckwerts. Catalysis by Brønsted bases of the reaction between CO<sub>2</sub> and water. *Transactions of the Faraday Society*, 59:386–395, 1963. URL <https://doi.org/10.1039/TF9635900386>.
- [106] D. T. Phan, M. Maeder, R. C. Burns, and G. Puxty. Catalysis of CO<sub>2</sub> absorption in aqueous solution by inorganic oxoanions and their application to post combustion capture. *Environmental Science & Technology*, 48(8):4623–4629, 2014. URL <https://doi.org/10.1021/es500667s>.
- [107] D. T. Phan, M. Maeder, R. C. Burns, and G. Puxty. Catalysis of CO<sub>2</sub> absorption in aqueous solution by vanadate and sulfate and their application to post combustion capture. *International Journal of Greenhouse Gas Control*, 36:60–65, 2015. URL <https://doi.org/10.1016/j.ijggc.2015.02.013>.
- [108] E. Kim, S. Lee, D. Lee, K. Jang, J. Park, and W. Y. Choi. Alpha effect-driven enhancement of CO<sub>2</sub> capture kinetics and size-controlled NaHCO<sub>3</sub> crystals: Promoter-added NaOH absorbent study. *Separation and Purification Technology*, 343:126943, 2024. URL <https://doi.org/10.1016/j.seppur.2024.126943>.
- [109] H. E. Benson, J. H. Field, and W. P. Haynes. Improved process for CO<sub>2</sub> absorption uses hot carbonate solutions. *Chemical Engineering Progress*, 52(10), 1956.
- [110] G. T. Rochelle, E. Chen, J. T. Cullinane, M. Hilliard, J. Lu, B. Oyekan, and R. Dugas. CO<sub>2</sub> Capture by absorption with potassium carbonate. Technical report, U.S. Department of Energy, 2004. URL <https://doi.org/10.2172/829575>.
- [111] J. T. Cullinane and G. T. Rochelle. Kinetics of carbon dioxide absorption into aqueous potassium carbonate and piperazine. *Industrial & Engineering Chemistry Research*, 45(8):2531–2545, 2006. URL <https://doi.org/10.1021/ie050230s>.
- [112] X. Ye and Y. Lu. CO<sub>2</sub> absorption into catalyzed potassium carbonate-bicarbonate solutions: Kinetics and stability of the enzyme carbonic anhydrase as a biocatalyst. *Chemical Engineering Science*, 116:567–575, 2014. URL <https://doi.org/10.1016/j.ces.2014.05.040>.
- [113] A. K. Kunze, G. Dojchinov, V. S. Haritos, and P. Lutze. Reactive absorption of CO<sub>2</sub> into enzyme accelerated solvents: From laboratory to pilot scale. *Applied Energy*, 156:676–685, 2015. URL <https://doi.org/10.1016/j.apenergy.2015.07.033>.

- [114] L. Fradette, S. Lefebvre, and J. Carley. Demonstration results of enzyme-accelerated CO<sub>2</sub> capture. *Energy Procedia*, 114:1100–1109, 2017. URL <https://doi.org/10.1016/j.egypro.2017.03.1263>.
- [115] P. C. Tseng, W. S. Ho, and D. W. Savage. Carbon dioxide absorption into promoted carbonate solutions. *AIChE Journal*, 34(6):922–931, 1988. URL <https://doi.org/10.1002/aic.690340604>.
- [116] H. Thee, Y. A. Suryaputradinata, K. A. Mumford, K. H. Smith, G. da Silva, S. E. Kentish, and G. W. Stevens. A kinetic and process modeling study of CO<sub>2</sub> capture with MEA-promoted potassium carbonate solutions. *Chemical Engineering Journal*, 210:271–279, 2012. URL <https://doi.org/10.1016/j.cej.2012.08.092>.
- [117] H. Thee, N. J. Nicholas, K. H. Smith, G. da Silva, S. E. Kentish, and G. W. Stevens. A kinetic study of CO<sub>2</sub> capture with potassium carbonate solutions promoted with various amino acids: Glycine, sarcosine and proline. *International Journal of Greenhouse Gas Control*, 20:212–222, 2014. URL <https://doi.org/10.1016/j.ijggc.2013.10.027>.
- [118] Y. Li, L. Wang, Z. Tan, Z. Zhang, and X. Hu. Experimental studies on carbon dioxide absorption using potassium carbonate solutions with amino acid salts. *Separation and Purification Technology*, 219:47–54, 2019. URL <https://doi.org/10.1016/j.seppur.2019.03.010>.
- [119] P. V. Danckwerts. The reaction of CO<sub>2</sub> with ethanolamines. *Chemical Engineering Science*, 34(4):443–446, 1979. URL [https://doi.org/10.1016/0009-2509\(79\)85087-3](https://doi.org/10.1016/0009-2509(79)85087-3).
- [120] E. Alper and W. D. Deckwer. Kinetics of absorption of CO<sub>2</sub> into buffer solutions containing carbonic anhydrase. *Chemical Engineering Science*, 35(3):549–557, 1980. URL [https://doi.org/10.1016/0009-2509\(80\)80003-0](https://doi.org/10.1016/0009-2509(80)80003-0).
- [121] S. Peirce, R. Perfetto, M.E. Russo, C. Capasso, M. Rossi, P. Salatino, and A. Marzocchella. Characterization of technical grade carbonic anhydrase as biocatalyst for CO<sub>2</sub> capture in potassium carbonate solutions. *Greenhouse Gases: Science and Technology*, 8(2):279–291, 2018. URL <https://doi.org/10.1002/ghg.1738>.
- [122] Y. Lu, X. Ye, Z. Zhang, A. Khodayari, and T. Djukadi. Development of a carbonate absorption-based process for post-combustion CO<sub>2</sub> capture: the role of biocatalyst to promote CO<sub>2</sub> absorption rate. *Energy Procedia*, 4:1286–1293, 2011. URL <https://doi.org/10.1016/j.egypro.2011.01.185>.
- [123] W. C. Floyd III, S. E. Baker, C. A. Valdez, J. K. Stolaroff, J. P. Bearinger, J. H. Satcher Jr, and R. D. Aines. Evaluation of a carbonic anhydrase mimic for industrial carbon capture. *Environmental Science & Technology*, 47(17):10049–10055, 2013. URL <https://doi.org/10.1021/es401336f>.

- [124] J. H. Field. Separation of CO<sub>2</sub> from gas mixtures, June 28 1975. US Patent 3,907,969.
- [125] A. G. Eickmeyer. Method and compositions for removing acid gases from gaseous mixtures and reducing corrosion of ferrous surface areas in gas purification systems, July 22 1975. US Patent 3,896,212.
- [126] J. Zhang and F. J. Martin. Corrosion of steel by carbonate-bicarbonate solution for CO<sub>2</sub> capture. *Materials and Corrosion*, 64(5):388–393, 2013. URL <https://doi.org/10.1002/maco.201106235>.
- [127] T. W. Trofe, K. E. McIntush, and M. C. Murff. Stretford process operations and chemistry report. Final report. Technical report, Radian Corp., Austin, TX (United States), 1993. URL <https://doi.org/10.2172/6914608>.
- [128] B. Scott, J. R. Daniels, and I. Chao. Corrosion history of a hot pot CO<sub>2</sub> absorber. In *AIChE Symposium on Safety in Ammonia and Related Facilities*, pages 127–134, 1987.
- [129] L. Qinghua, T. Jinlin, and S. Yajun. Catalytic activity of vanadium pentoxide for the absorption of carbon dioxide by potassium carbonate solution. *Acta Physico-Chimica Sinica*, 8(6):753–759, 1992. URL <https://doi.org/10.3866/PKU.WHXB19920608>.
- [130] N. J. Nicholas, G. da Silva, S. Kentish, and G. W. Stevens. Use of vanadium (V) oxide as a catalyst for CO<sub>2</sub> hydration in potassium carbonate systems. *Industrial & Engineering Chemistry Research*, 53(8):3029–3039, 2014. URL <https://doi.org/10.1021/ie403836e>.
- [131] K. Endo, Q. S. Nguyen, S. E. Kentish, and G. W. Stevens. The effect of boric acid on the vapour liquid equilibrium of aqueous potassium carbonate. *Fluid Phase Equilibria*, 309(2):109–113, 2011. URL <https://doi.org/10.1016/j.fluid.2011.06.031>.
- [132] D. Schäfer, Á. Pérez-Salado Kamps, B. Rumpf, and G. Maurer. Experimental investigation on the influence of boric acid on the solubility of carbon dioxide in aqueous solutions of potassium hydroxide. *Vestnik Sankt-Peterburgskogo universiteta, Seriya 7: Geologia, G*, pages 127–133, 03 2013.
- [133] S. Shen, Y. Yang, and S. Ren. CO<sub>2</sub> absorption by borate-promoted carbonate solution: Promotion mechanism and vapor liquid equilibrium. *Fluid Phase Equilibria*, 367:38–44, 2014. URL <https://doi.org/10.1016/j.fluid.2014.01.027>.
- [134] F. J. W. Roughton and V. H. Booth. The catalytic effect of buffers on the reaction  $\text{CO}_2 + \text{H}_2\text{O} \rightleftharpoons \text{H}_2\text{CO}_3$ . *Biochemical Journal*, 32(11):2049, 1938. URL <https://doi.org/10.1042/bj0322049>.
- [135] M. Kiese and A. B. Hastings. The catalytic hydration of carbon dioxide. *Journal of Biological Chemistry*, 132(1):267–280, 1940. URL [https://doi.org/10.1016/S0021-9258\(18\)73415-7](https://doi.org/10.1016/S0021-9258(18)73415-7).

- [136] H. Thee, K. H. Smith, G. da Silva, S. E. Kentish, and G. W. Stevens. Carbon dioxide absorption into unpromoted and borate-catalyzed potassium carbonate solutions. *Chemical Engineering Journal*, 181:694–701, 2012. URL <https://doi.org/10.1016/j.cej.2011.12.059>.
- [137] K. H. Smith, C. J. Anderson, W. Tao, K. Endo, K. A. Mumford, S. E. Kentish, A. Qader, B. Hooper, and G. W. Stevens. Pre-combustion capture of CO<sub>2</sub> - results from solvent absorption pilot plant trials using 30 wt% potassium carbonate and boric acid promoted potassium carbonate solvent. *International Journal of Greenhouse Gas Control*, 10:64–73, 2012. URL <https://doi.org/10.1016/j.ijggc.2012.05.018>.
- [138] D. Guo, H. Thee, G. da Silva, J. Chen, W. Fei, S. Kentish, and G. W. Stevens. Borate-catalyzed carbon dioxide hydration via the carbonic anhydrase mechanism. *Environmental Science & Technology*, 45(11):4802–4807, 2011. URL <https://doi.org/10.1021/es200590m>.
- [139] R. A. T. O. Nijsing, R. H. Hendriks, and H. Kramers. Absorption of CO<sub>2</sub> in jets and falling films of electrolyte solutions, with and without chemical reaction. *Chemical Engineering Science*, 10(1-2):88–104, 1959. URL [https://doi.org/10.1016/0009-2509\(59\)80028-2](https://doi.org/10.1016/0009-2509(59)80028-2).
- [140] H. Knuutila, O. Juliussen, and H. F. Svendsen. Kinetics of the reaction of carbon dioxide with aqueous sodium and potassium carbonate solutions. *Chemical Engineering Science*, 65(23):6077–6088, 2010. URL <https://doi.org/10.1016/j.ces.2010.07.018>.
- [141] Á. Pérez-Salado Kamps, E. Meyer, B. Rumpf, and G. Maurer. Solubility of CO<sub>2</sub> in aqueous solutions of KCl and in aqueous solutions of K<sub>2</sub>CO<sub>3</sub>. *Journal of Chemical & Engineering Data*, 52(3):817–832, 2007. URL <https://doi.org/10.1021/je060430q>.
- [142] S. Weisenberger and A. Schumpe. Estimation of gas solubilities in salt solutions at temperatures from 273 K to 363 K. *AIChE Journal*, 42(1):298–300, 1996. URL <https://doi.org/10.1002/aic.690420130>.
- [143] H. Knuutila, O. Juliussen, and H. F. Svendsen. Density and N<sub>2</sub>O solubility of sodium and potassium carbonate solutions in the temperature range 25 to 80 °C. *Chemical Engineering Science*, 65(6):2177–2182, 2010. URL <https://doi.org/10.1016/j.ces.2009.12.015>.
- [144] H. Hikita, S. Asai, H. Ishikawa, and Y. Saito. Kinetics of absorption of chlorine in aqueous acidic solutions of ferrous chloride. *Chemical Engineering Science*, 30(5-6):607–616, 1975. URL [https://doi.org/10.1016/0009-2509\(75\)80033-9](https://doi.org/10.1016/0009-2509(75)80033-9).
- [145] X. Ye and Y. Lu. Kinetics of CO<sub>2</sub> absorption into uncatalyzed potassium carbonate-bicarbonate solutions: Effects of CO<sub>2</sub> loading and ionic strength in the solutions. *Chemical Engineering Science*, 116:657–667, 2014. URL <https://doi.org/10.1016/j.ces.2014.05.050>.

- [146] E. G. Kloosterman, S. M. De Vries, H. Kalsbeek, and B. Drinkenburg. Influence of ionic strength on the absorption of  $\text{CO}_2$  in carbonate/bicarbonate buffer solutions. *Industrial & Engineering Chemistry Research*, 26(11):2216–2222, 1987. URL <https://doi.org/10.1021/ie00071a008>.
- [147] D. Roberts and P. V. Danckwerts. Kinetics of  $\text{CO}_2$  absorption in alkaline solutions - I transient absorption rates and catalysis by arsenite. *Chemical Engineering Science*, 17(12):961–969, 1962. URL [https://doi.org/10.1016/0009-2509\(62\)80074-8](https://doi.org/10.1016/0009-2509(62)80074-8).
- [148] J. Haubrock, J. A. Hogendoorn, and G. F. Versteeg. The applicability of activities in kinetic expressions: A more fundamental approach to represent the kinetics of the system  $\text{CO}_2\text{-OH}^-$ -salt in terms of activities. *Chemical Engineering Science*, 62(21):5753–5769, 2007. URL <https://doi.org/10.1016/j.ces.2007.06.018>.
- [149] S. Gondal, H. F. Svendsen, and H. K. Knuutila. Activity based kinetics of  $\text{CO}_2\text{-OH}^-$  systems with  $\text{Li}^+$ ,  $\text{Na}^+$  and  $\text{K}^+$  counter ions. *Chemical Engineering Science*, 151:1–6, 2016. URL <https://doi.org/10.1016/j.ces.2016.05.009>.
- [150] B. R. W. Pinsent, L. Pearson, and F. J. W. Roughton. The kinetics of combination of carbon dioxide with hydroxide ions. *Transactions of the Faraday Society*, 52:1512–1520, 1956. URL <https://doi.org/10.1039/TF9565201512>.
- [151] L. Kucka, E. Y. Kenig, and A. Gorak. Kinetics of the gas- liquid reaction between carbon dioxide and hydroxide ions. *Industrial & Engineering Chemistry Research*, 41(24):5952–5957, 2002. URL <https://doi.org/10.1021/ie020452f>.
- [152] S. Gondal, N. Asif, H. F. Svendsen, and H. Knuutila. Kinetics of the absorption of carbon dioxide into aqueous hydroxides of lithium, sodium and potassium and blends of hydroxides and carbonates. *Chemical Engineering Science*, 123:487–499, 2015. URL <https://doi.org/10.1016/j.ces.2014.10.038>.
- [153] R. Pohorecki and W. Moniuk. Kinetics of reaction between carbon dioxide and hydroxyl ions in aqueous electrolyte solutions. *Chemical Engineering Science*, 43(7):1677–1684, 1988. URL [https://doi.org/10.1016/0009-2509\(88\)85159-5](https://doi.org/10.1016/0009-2509(88)85159-5).
- [154] E. I. Konnik. Salting-out and salting-in of gaseous non-electrolytes in aqueous solutions of electrolytes. *Russian Chemical Reviews*, 46(6):577–588, 1977. URL <https://doi.org/10.1070/RC1977v046n06ABEH002157>.
- [155] M. Wagner, I. von Harbou, J. Kim, I. Ermatchkova, G. Maurer, and H. Hasse. Solubility of carbon dioxide in aqueous solutions of monoethanolamine in the low and high gas loading regions. *Journal of Chemical & Engineering Data*, 58(4):883–895, 2013. URL <https://doi.org/10.1021/je301030z>.
- [156] M. Amirkhosrow, J. Pérez-Calvo, M. Gazzani, M. Mazzotti, and E. Nemati Lay. Rigorous rate-based model for  $\text{CO}_2$  capture via monoethanolamine-based solutions: effect of kinetic models, mass transfer, and holdup correlations on prediction accuracy. *Separation Science and Technology*, 56(9):1491–1509, 2021. URL <https://doi.org/10.1080/01496395.2020.1784943>.

- [157] R. Meier, G. Werner, R. Kirmse, J. Stach, and L. Dunsch. Voltammetrische und spektroskopische untersuchungen zur komplexbildung von Vanadium (IV) und Vanadium (V) mit Carbonat. *Zeitschrift für anorganische und allgemeine Chemie*, 583(1):209–222, 1990. URL <https://doi.org/10.1002/zaac.19905830126>.
- [158] N. McCann, M. Imle, and H. Hasse. Carbonate complexes of vanadate. *Polyhedron*, 95:81–85, 2015. URL <https://doi.org/10.1016/j.poly.2015.03.004>.
- [159] E. G. Ribó, Z. Mao, J. S. Hirschi, T. Linsday, K. Bach, E. D. Walter, C. R. Simons, T. J. Zuehlsdorff, and M. Nyman. Implementing vanadium peroxides as direct air carbon capture materials. *Chemical Science*, 15(5):1700–1713, 2024. URL <https://doi.org/10.1039/D3SC05381D>.
- [160] N. McCann, M. Wagner, and H. Hasse. A thermodynamic model for vanadate in aqueous solution—equilibria and reaction enthalpies. *Dalton Transactions*, 42(7):2622–2628, 2013. URL <https://doi.org/10.1039/C2DT31993D>.
- [161] R. Pohorecki and E. Kucharski. Desorption with chemical reaction in the system CO<sub>2</sub>-aqueous solution of potassium carbonate. *The Chemical Engineering Journal*, 46(1):1–7, 1991. URL [https://doi.org/10.1016/0300-9467\(91\)80001-D](https://doi.org/10.1016/0300-9467(91)80001-D).
- [162] K. Bach, E. Garrido Ribó, J. S. Hirschi, Z. Mao, M. T. Nord, L. N. Zakharov, K. A. Goulas, T. J. Zuehlsdorff, and M. Nyman. Tetraperoxotitanates for high-capacity direct air capture of carbon dioxide. *Chemistry of Materials*, 37(1):48–61, 2024. URL <https://doi.org/10.1021/acs.chemmater.4c01795>.
- [163] Z. Mao, M. Rashwan, E. Garrido Ribó, M. Nord, L. N. Zakharov, T. W. Surta, A. Uysal, and M. Nyman. Carbon dioxide capture by niobium polyoxometalate fragmentation. *Journal of the American Chemical Society*, 146(28):19489–19498, 2024. URL <https://doi.org/10.1021/jacs.4c06178>.
- [164] Florian Walthert. Kinetic analysis of CO<sub>2</sub> absorption in loaded potassium carbonate solutions. Master’s thesis, KTH Royal Institute of Technology, Stockholm, Sweden, 2024. URL <https://kth.diva-portal.org/smash/record.jsf?pid=diva2%3A1901712>.
- [165] P. V. Danckwerts and M. M. Sharma. The absorption of carbon dioxide into solutions of alkalis and amines (with some notes on hydrogen sulfide and carbonyl sulfide). *The Chemical Engineer*, Review Series No. 2, 1966.

